NOVEL PROPERTIES OF FERROMAGNETIC P-WAVE SUPERCONDUCTORS

by

CHRISTOPHER LÖRSCHER
M.S. University of Central Florida, 2010
B.S. University of Central Florida, 2007

A dissertation submitted in partial fulfilment of the requirements
for the degree of Doctor of Philosophy
in the Department of Physics
in the College of Sciences
at the University of Central Florida
Orlando, Florida

Summer Term
2014

Major Professor: Richard Andrew Klemm

ABSTRACT

This thesis investigates the many extraordinary physical properties of the candidate p-wave ferromagnetic superconductors UCoGe and URhGe, and proposes theoretical predictions for p-wave superconductors yet to be discovered. In particular, we carry out angular dependent quantum field theoretical calculations of the thermodynamic $H-T$ phase diagram known as the upper critical field $\boldsymbol{H}_{c2}(\theta,\phi,t)$, or more appropriately for ferromagnetic superconductors the upper critical induction, $\boldsymbol{B}_{c2}(\theta,\phi,t) = \mu_0\boldsymbol{H}_{c2} + \boldsymbol{M}(\boldsymbol{H}_{c2})$, where $\boldsymbol{M}(\boldsymbol{H}_{c2}) = \boldsymbol{M_0} + \delta\boldsymbol{M}(\boldsymbol{H_{c2}})$, and $\boldsymbol{M}_0$ is the spontaneous magnetization of the material, for various p-wave superconducting order parameter symmetries including: The axial Anderson-Brinkman-Morel (ABM) state, the chiral Scharnberg-Klemm (SK) state, and the completely broken symmetry polar state (CBS), as well as for some other states with partially broken symmetry (PBS) superconducting order parameter symmetries. The most notable contribution of the work presented in this thesis is the application of the Klemm-Clem transformations to analytically calculate the full angular θ,ϕ and temperature T dependencies of the upper critical field $\boldsymbol{H}_{c2}(\theta,\phi,t)$ for orthorhombic materials, which may prove to be useful to experimentalists in identifying these exotic states of matter experimentally. Second, this work formulates a double spin-split ellipsoidal Fermi surface (FS) model for ferromagnetic superconductors in the normal state, which introduces a field dependence to the effective mass in one crystallographic direction on the dominant Fermi surface and to the chemical potential, and is subsequently applied to the normal state of URhGe to explain theoretically the anomalous specific heat data of Aoki and Flouquet [12]. Extension of this work to understanding the still elusive reentrant high-field superconducting phase of URhGe and the S-shaped $H_{c2}(T)$ curve for $\boldsymbol{H} \parallel \hat{\boldsymbol{b}}$ in H_{c2} measurements of UCoGe is discussed. Third, this work also presents theoretical fits to the upper critical field data of Kittika $et\ al.$ [61] for Sr_2RuO_4 using the helical p-wave states and including Pauli limiting effects.

TABLE OF CONTENTS

LIST OF FIGURES

CHAPTER 1: INTRODUCTION

Superconductivity is the magnificent phenomenon where a material undergoes a second order phase transition at a particular temperature, T_c, called the superconducting transition temperature, from a normal metal to to an exotic material that allows electrical current to flow without resistance. This exciting new phenomena was discovered by Heike Kamerlingh Onnes and his graduate student, G. Holst, in Leiden, Netherlands in 1911 by cooling mercury to liquid helium temperatures. At 4.2 K, the temperature dependant resistivity, $\rho(T)$, was observed to drastically vanish, signaling the onset of a phase transition to the superconducting state where the electrical resistance suddenly becomes zero $R = 0\ \Omega$. A microscopic theory of superconductivity was developed in 1957 by John Bardeen, Leon Cooper, and John Schrieffer, in the well known Bardeen-Cooper-Schriefer (BCS) theory of superconductivity. This theory explained the many effects that were observed in the conventional superconductors known at the time. Since then, however, many more materials have been discovered that defy this theory, including materials which exhibit ferromagnetism and superconductivity simultaneously in the same crystal, which for a long time were thought to be incompatible quantum orderings, since ferromagnetic order would be conducive only for parallel spin pairing, which is not permitted in conventional BCS theory; only anti-parallel spins with equal and opposite momenta could pair according to BCS theory. The Meissner effect, where externally applied magnetic fields are expelled from the interior of superconductors up to a penetration depth, also is inconsistent with parallel spin pairing and the simultaneous coexistence of superconductivity and ferromagnetism; that is, all conventional type-I superconductors expel externally applied magnetic fields from their interior, effectively forcing the magnetic induction, $\boldsymbol{B}$ inside the material to vanish. The Meissner effect and BCS theory are not compatible with the recently discovered ferromagnetic superconductors, URhGe and UCoGe, which exhibit both ferromagnetism and superconductivity below the superconducting transition temperature, T_c, which is well below the

Curie temperature, T_C.

Introduction to conventional superconductivity

Since its discovery by Heike Kamerlingh Onnes in 1911, superconductivity posed a serious challenge to Quantum Mechanics, and many phenomenological theories explaining certain aspects of this strange phenomenon were devised leading up to to the microscopic description by Bardeen, Cooper and Schrieffer in 1957. One of the ubiquitous properties of conventional superconductors is how it responds to externally applied magnetic fields, $\boldsymbol{H}$. In 1933, Meissner and Ochsenfeld discovered that in addition to having zero electrical resistance, superconductors also expel all magnetic flux from their interior. Although since then, many superconducting materials have been found to allow magnetic flux to penetrate their cores albeit in quantized values of the flux quantum (type-II superconductors),

$$\Phi_0 = \frac{h}{2e}, \tag{1.1}$$

many materials (type-I superconductors) have been found to exhibit this effect, called the Meissner-Ochsenfeld effect. In light of Meissner and Ochsenfeld's discovery that all magnetic fields are expelled from a superconductor, London proposed a phenomenological theory of this effect by using Maxwell's equations. London proposed that since the magnetic field lines are expelled from the superconductor's interior, the magnetic induction $\boldsymbol{B}$, should vanish inside the superconductor, from which one can deduce that the magnetic permeability of the superconductor to be $\mu = 0$ from $\boldsymbol{B} = \mu_0 \boldsymbol{H} + \boldsymbol{M}$. In the Meissner states, $\boldsymbol{B} = 0$ so that $\boldsymbol{M} = -\mu_0 \boldsymbol{H}$. Thus, London modeled the superconductivity as perfect diamagnetism using Maxwell's equations obtaining the equation for

the magnetic induction

$$\boldsymbol{B} + \lambda_L^2(\nabla(\nabla \cdot \boldsymbol{B}) - \nabla^2 \boldsymbol{B}) = 0, \tag{1.2}$$

where λ_L is the London penetration depth,

$$\lambda_L = \sqrt{\frac{m}{\mu_0 n_s e^2}}, \tag{1.3}$$

where n_s is the density of superconducting electrons. The solution to this differential equation is found by looking for solutions independent of x and y for a superconductor occupying the space $z > 0$, and is given by

$$B_x(z) \propto e^{-z/\lambda_L}, \tag{1.4}$$

which is the equation for the induction parallel to the superconductor, which was shown to drop off exponentially over a length λ_L, as opposed to discontinuously as first proposed by Meissner and Ochsenfeld. The origin of this diamagnetic behavior exhibited by superconductors is due to persistent currents that exist in a strip of width λ_L near the superconductor's surface.

In addition to the London theory of the Meissner Ochsenfeld effect, Landau and Ginzburg began to formulate their own phenomenological theory of the second order phase transition to the superconducting state using the ubiquitous idea of free energy, F, and the idea of an order parameter, Ψ, which characterizes the degree of order of the appropriate type at a given temperature ($e.g.$ magnetization for ferromagnetism). Ginzburg and Landau formulated a free energy functional, $F[\Psi(\boldsymbol{r})]$,

which depends on the order parameter/global wave function of the superconductor, $\Psi(\boldsymbol{r})$,

$$F[\Psi(\boldsymbol{r})] = \int \frac{d^3r}{V} \left[\alpha|\Psi|^2 + \frac{\beta}{2}|\Psi|^4 + \frac{1}{8\pi}B^2 + \frac{1}{2m^*} \left| \left(\frac{\hbar}{i}\nabla + e^* \boldsymbol{A}(\boldsymbol{r}) \right) \right] \Psi(\boldsymbol{r}) \right|^2, \tag{1.5}$$

where $\alpha(T) = \alpha'(T - T_c)$, $\alpha' > 0$, and $\beta > 0$ are the appropriate phenomenological parameters of the theory, m^* is the effective mass, and e^* is the effective charge, which was later found to be $e^* = 2e$ in the BCS theory.

Taking the functional derivative with respect to Ψ^* we obtain

$$\frac{\delta F}{\delta \Psi^*} = \left[\alpha(T) + \beta|\Psi|^2 + \frac{1}{2m^*} \left(\frac{\hbar}{i}\nabla + e^* \boldsymbol{A}(\boldsymbol{r}) \right)^2 \right] \Psi = 0, \tag{1.6}$$

which for the simplest case in which $\boldsymbol{B} = 0$ and neglecting the gradient term results in

$$\Psi = \pm\sqrt{\frac{-\alpha(T)}{\beta}}, \tag{1.7}$$

which has real solutions only for $\alpha(T) < 0$, otherwise the trivial solution $\Psi = 0$ prevails. Ginzburg and Landau theorized that at a particular temperature when the phase transition to the superconducting state occurs, $T = T_c$, the parameter $\alpha(T)$ would change sign, and thus the simplest form that it could take is

$$\alpha(T) = \alpha'(T - T_c), \tag{1.8}$$

which for $T > T_c$ we have $\alpha(T) > 0$ and we have the global wavefunction vanishing at all

locations $\Psi(\boldsymbol{r}) = 0$, and for $T < T_c$ we have that $\alpha(T) < 0$ and thus $\Psi = \pm\sqrt{\frac{|\alpha(T)|}{\beta}}$, so that the superconducting order parameter behaves as

$$\Psi(T) \propto (T_c - T)^{1/2} \tag{1.9}$$

for $T < T_c$ with the onset of superconducting order just below T_c and maximum at $T = 0$, and zero for $T > T_c$. One question remains: what kind of order exists in superconducting materials? The answer to this question would take almost a decade to resolve, when Bardeen, Cooper and Schrieffer developed the microscopic theory of superconductivity in 1957.

The two natural lengths scales that are present in the Ginzburg-Landau theory are the London penetration depth, λ_L, given by

$$\lambda_L^2 = \frac{m^*\beta}{|\alpha(T)|(2e)^2} \tag{1.10}$$

and the coherence length ξ, given by

$$\xi^2 = \frac{\hbar^2}{2m^*|\alpha(T)|}, \tag{1.11}$$

which is the most probable range of a region fluctuating into the superconducting state, which is expected to diverge as $1/|T - T_c|$ close to T_c, which is the signature of any second order phase transition.

The ratio of these two quantities,

$$\kappa = \lambda_L/\xi = \frac{m^*}{e\hbar}\sqrt{\frac{\beta}{2}} \tag{1.12}$$

is the only free parameter in the Ginzburg-Landau theory.

For $\kappa < 1/\sqrt{2}$ one has so-called type-I superconductor which exhibits a Meissner effect where the externally applied magnetic field is expelled from the interior of the superconductor by persistent current in a thin layer of width λ_L on the outer edge of the superconductor. For $\kappa > 1/\sqrt{2}$ one has a type-II superconductor, which allows magnetic flux lines to penetrate its interior in integral multiples of the flux quantum, $\Phi = n\Phi_0$, where $\Phi_0 = \frac{h}{2e}$, forming an array of flux lines called an Abrikosov vortex lattice.

It wasn't until 1957 that superconductivity was given a rigorous mean field theoretical description by Bardeen, Cooper and Schrieffer. The main contribution of the BCS theory was to provide insight on the mechanism driving the superconductivity. The theory assumed that there must be some pairing between electrons at the Fermi level, which is brought about by an attractive interaction, which was later shown to be due to the electron-phonon interaction.

Superconductivity and magnetism

Much has changed in the field of superconductivity since its discovery by Heike Kamerlingh Onnes in 1911, and its subsequent mean field theoretical description given in 1957 by the Bardeen-Cooper-Schrieffer (BCS) theory. In conventional BCS superconductivity, Cooper pairs are formed by electrons with opposite spins by an attractive interaction mediated by phonons in the crystal,

with a spin-wave function of the form

$$\chi_{s-wave} = 1/\sqrt{2}(|\uparrow\downarrow> - |\downarrow\uparrow>), \tag{1.13}$$

which has a total spin of $s = 0$ and has even orbital symmetry (i.e. $l = 0, 2, ...$). This channel for Cooper pairing is incompatible with ferromagnetism, since ferromagnetic order would be conducive only to equal spin pairing ($e.g.$ p-wave pairing with $l = 1$); thus, these two orders were for a long time believed to be mutually exclusive. However, recent discoveries of heavy fermion superconducting materials such as UGe_2 [3], UCoGe [1, 48], and URhGe [5, 38, 7, 8, 9, 11] in which there is simultaneous ferromagnetic and superconducting order, have sparked renewed interest in the field of p-wave superconductivity. For such superconductors, the symmetry of the spin component of the wave function is odd (i.e. $l = 1, 3, ...$), with p-wave symmetry (i.e. $l = 1$) being the simplest example of such a case. In these novel superconductors, the Cooper spin pairs form triplet states, with spin-wave functions of the form

$$\chi_{p-wave} = \begin{cases} |\uparrow\uparrow> \\ 1/\sqrt{2}(|\uparrow\downarrow> + |\downarrow\uparrow>), \\ |\downarrow\downarrow> \end{cases} \tag{1.14}$$

as opposed to singlet states that their s-wave counterparts form. Unlike their s-wave counterparts, p-wave ferromagnetic superconductors do not have their Cooper pairs mediated by phonons. The exact mechanism behind equal spin pairing is currently unknown, but it has been widely purported to arise from ferromagnetic spin fluctuations, especially close to a quantum critical point at $T = 0$, providing the necessary superconducting glue to form pairs.

The parallel-spin triplet states are much more resilient to the externally applied magnetic field $\boldsymbol{H}$,

which is evident from (1) their unusually high zero-temperature upper critical inductions, $B_{c2}(0)$, which in some cases exceeds the Pauli limit,

$$B_P \sim 1.85 T_c \text{ T/K}, \tag{1.15}$$

by a factor of twenty, in at least one crystallographic direction, where T_c is the superconducting transition temperature in K, and (2) by the temperature T independence of the Knight shift for applied fields $\boldsymbol{H}$ normal to the direction of the ferromagnetism,[48] so that these experiments are consistent with one another. In contrast, the Knight shift and $B_{c2,||}(0)$ for fields parallel to the layers of Sr_2RuO_4, are inconsistent with one another [33], and there is no observable ferromagnetism in the superconducting state in sharp contrast with the most likely candidate p-wave superconductors which all possess ferromagnetism in the superconducting state. Ferromagnetic superconductors have the ferromagnetic transition temperature $T_{\rm Curie}$ exceeding the superconducting transition temperature T_c.

The orbital symmetry of the superconducting order parameter, $\Delta(\boldsymbol{k})$, which for p-wave superconductors depends on the wave-vector of the electrons forming the Cooper pair, $\boldsymbol{k}$. $\Delta(\boldsymbol{k})$ can usually be classified by its nodes, both in the order parameter and in the resulting superconducting energy gap, where the superconducting order parameter vanishes on the Fermi surface. For p-wave superconductors free of long-range ferromagnetism, one may have a nodeless gap, such as for the isotropic Balian-Werthamer (BW) state of ^{3}He [30], or a gap with either planar nodes (polar state), or point nodes (axial state), where it vanishes on the Fermi surface (FS). The basic order parameter symmetries of these three basic order parameters are depicted in Fig. 1.1.

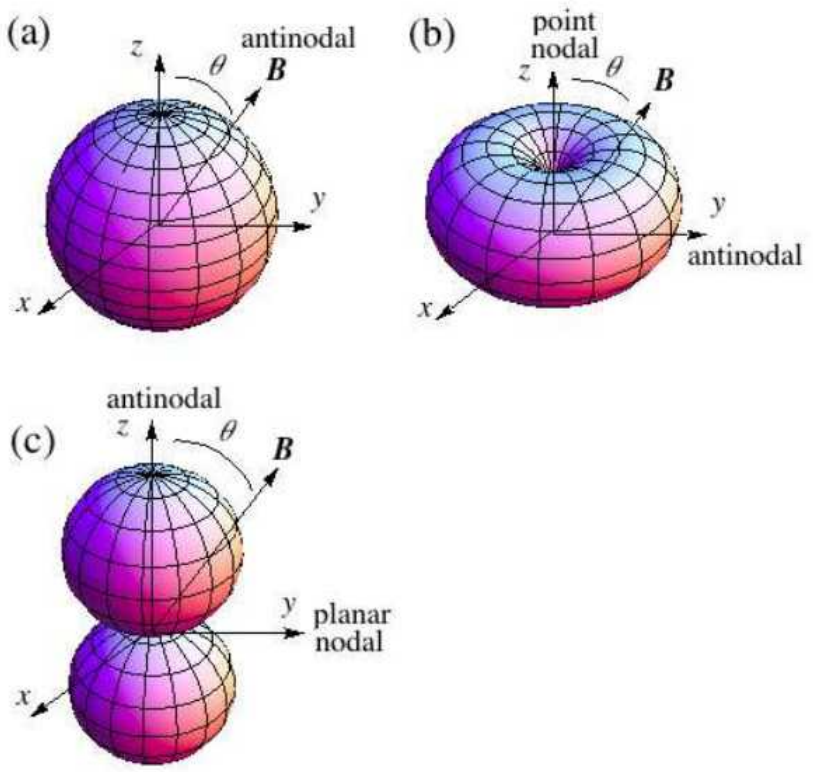

Figure 1.1: Sketches of the three basic types of p-wave gap functions $|\Delta(\hat{\boldsymbol{k}})|$. (a) The non-chiral BW, or isotropic gap $|\Delta_0|$ p-wave state, for which $H_{c2}(T)$ is given by $H_{c2,\mathrm{p\ antinodal}}(T)$ for all $\boldsymbol{H}$ directions [13]. (b) The ABM and SK states. When these states have their antinodal planes locked onto a uniaxial crystal plane, breaking the planar antinodal axial rotational symmetry, the chiral ABM states have complex order parameters $\Delta_{0\pm}(\hat{k}_x \pm i\hat{k}_y)$ with distinct $H_{c2,\mathrm{ABM\ nodal}}(T)$ and $H_{c2,\mathrm{ABM\ antinodal}}(T)$ for $\boldsymbol{H}$ along the nodal axis and antinodal planar directions, respectively [13, 72]. The SK state with order parameter $\sum_{\sigma=\pm}\Delta_{0,\sigma}(\hat{k}_x + i\sigma\hat{k}_y)$ is more complicated. For $\boldsymbol{H}$ along the nodal axis, the SK state is chiral with $H_{c2,\mathrm{SK\ nodal}}(T)$ [13]. For $\boldsymbol{H}$ in the antinodal plane, the SK state is non-chiral with $H_{c2,\mathrm{p\ antinodal}}(T)$ [72]. See text. (c) The non-chiral polar/CBS state. This state with order parameter $\Delta_0 k_z$ has its antinodal axis locked onto a crystal axis (e.g., the $\hat{\boldsymbol{z}}$ axis), breaking the point antinodal axial rotational symmetry. For $\boldsymbol{H}$ parallel and perpendicular to the antinodal axis, $H_{c2}(T)$ is respectively $H_{c2,\mathrm{p\ antinodal}}(T)$ and the distinct planar nodal form, $H_{c2,\mathrm{planar\ nodal}}(T)$ [14].

Each of these states possesses unique T and (θ, ϕ) orientational dependencies of $\boldsymbol{H}_{c2}(T)$, which are useful in identifying the orbital symmetries experimentally. It was shown theoretically by Scharnberg and Klemm that for p-wave superconductors with an isotropic equal-spin pairing interaction of the form

$$V_{3D}(\hat{\boldsymbol{k}}, \hat{\boldsymbol{k}}') = V_0 \hat{\boldsymbol{k}} \cdot \hat{\boldsymbol{k}}', \tag{1.16}$$

which leads to an isotropic BW state for $\boldsymbol{H} = 0$ with an isotropic gap function as sketched in Fig.1.1(a), $\boldsymbol{H}_{c2}(T)$ is always given by that of the polar state, $H_{c2,\mathrm{polar}}(T)$ [13], in which $\boldsymbol{H}$ always points in an antinodal order parameter direction. This is analogous to the interaction of $\boldsymbol{H}$ with spins through the rotationally-invariant Heisenberg interaction with an isotropic $\boldsymbol{g}$-tensor. To avoid confusion with the various order parameter states, we hereby designate $H_{c2,\mathrm{p\ antinodal}}(T) \equiv H_{c2,\mathrm{polar}}(T)$. Except for the p-wave chiral ABM states [72], when $\boldsymbol{H}$ lies along the antinodal direction, $H_{c2}(T) = H_{c2,\mathrm{p\ antinodal}}(T)$, even though the state symmetry may be very different than that of the polar state. $H_{c2,\mathrm{p\ antinodal}}(T)$ has a much straighter T dependence than any other p-wave or s-wave state in pure, three-dimensional materials with a spherical, or ellipsoidal as this thesis presents, FS [13, 45].

Scharnberg and Klemm also investigated the effects of two pairing states perpendicular to $\boldsymbol{H}$ within the framework of the rotationally symmetric $V_{3D}(\hat{\boldsymbol{k}}, \hat{\boldsymbol{k}}')$. For $\boldsymbol{H}||\hat{\boldsymbol{z}}$, there are two order parameter components, which are usually written as

$$\Delta_{\pm}(\hat{\boldsymbol{k}}) = \Delta_{\pm,0}(\hat{k}_x \pm i\hat{k}_y), \tag{1.17}$$

both components of which nominally share the same T_c. These are the two chiral manifestations of the Anderson-Brinkman-Morel (ABM) state of ^{3}He [87, 88], in which only parallel-spin pairing with one spin state is involved. [13]. The term "chirality" refers to the azimuthal invariance of the

magnitude of the order parameter $|\Delta(\hat{\boldsymbol{k}})|$. This can be shown explicitly for an order parameter of the form given by Eq. 1.17.

$$\Delta_{\pm}(\hat{\boldsymbol{k}}) = \Delta_{\pm,0}(\sin\theta_{\boldsymbol{k}}\cos\phi_{\boldsymbol{k}} \pm i\sin\theta_{\boldsymbol{k}}\sin\phi_{\boldsymbol{k}}), \tag{1.18}$$

which can be rewritten as

$$\Delta_{\pm}(\hat{\boldsymbol{k}}) = \Delta_{\pm,0}\sin\theta_{\boldsymbol{k}}\exp(\pm i\phi_{\boldsymbol{k}}), \tag{1.19}$$

the magnitude of which is independent of the azimuthal angle $\phi_{\boldsymbol{k}}$. The $\pm$ corresponds to the two possible orientations of the parallel spin pairing.

These ABM states with $\boldsymbol{H} = 0$ have a gap function with a point nodes at the poles, as sketched in Fig. 1.1(b). Scharnberg and Klemm also investigated $H_{c2}(T)$ for the special case of $\boldsymbol{H}$ along the nodal point direction normal to the pairing plane of these chiral ABM states, and found that $H_{c2,\mathrm{ABM\,nodal}}(T)$ for either of these ABM states exhibited a T dependence that rose even more slowly with decreasing T than did $H_{c2,s}(T)$ for a pure, isotropic s-wave superconductor on a spherical (or ellipsoidal, as shown here) FS in the absence of Pauli-limiting effects [13].

However, Scharnberg and Klemm then investigated the effects of the two combined chiral ABM pairing states perpendicular to $\boldsymbol{H}$. In effect, they calculated $H_{c2}(T)$ for the two-component state

containing an unequal amplitude mix of the two chiral ABM states,

$$\Delta_{\rm SK}(\hat{\boldsymbol{k}}) = \sum_{\sigma=\pm} \Delta_{0,\sigma}(\hat{k}_x + i\sigma\hat{k}_y) \tag{1.20}$$

The SK state is a chiral state except for the special cases when $|\Delta_{0,+}| = |\Delta_{0,-}| = \Delta_0$, for which it is non-chiral. For those special cases, one may write

$$\Delta_{\rm SK}(\hat{\boldsymbol{k}}) = \Delta_0 \sum_{\sigma=\pm} e^{i\psi_\sigma}(\hat{k}_x + i\sigma\hat{k}_y), \tag{1.21}$$

which may be rewritten as

$$\Delta_{\rm SK}(\hat{\boldsymbol{k}}) = 2\Delta_0 e^{i\phi_+} \sin\theta_{\boldsymbol{k}} \cos(\phi_{\boldsymbol{k}} + \phi_-), \tag{1.22}$$

where $\phi_\pm = (\psi_+ \pm \psi_-)/2$ is independent of $\hat{\boldsymbol{k}}$. Except for the overall constant phase ϕ_+, $\Delta_{\rm SK}(\hat{\boldsymbol{k}})$ is therefore a real function of $\hat{\boldsymbol{k}}$ and hence non-chiral whenever $|\Delta_{0,+}| = |\Delta_{0,-}|$. The magnetic analog of this degenerate, two-component state is the anisotropic XY model of spin-spin interactions, in which there is an easy plane normal to a hard axis for spin-spin interactions with $\boldsymbol{H}$ in that plane, but the interactions within the easy plane can be either isotropic or anisotropic, depending upon the field direction. Although they originally denoted this as the "generalized ABM state" [13], this state came to be known as the SK state [14, 31, 26]. For $\boldsymbol{H}||\hat{\boldsymbol{z}}$, the chiral SK state has $H_{c2,\rm SK\ nodal}(T)$. However, for $\boldsymbol{H} \perp \hat{\boldsymbol{z}}$, the SK state is non-chiral just below $H_{c2,\rm p\ antinodal}(T)$ [72]. Although not mentioned in the original paper [13], the SK and ABM states might be favored in superconductors with uniaxial symmetry such as certain layered superconductors [33], for which $V_{2D}(\hat{\boldsymbol{k}}, \hat{\boldsymbol{k}}') = V_0(\hat{k}_x\hat{k}'_x + \hat{k}_y\hat{k}'_y)$ could lock onto the layers, breaking the axial rotational degree of freedom of the antinodal plane. Sr_2RuO_4 has often been mentioned as a likely candidate for

either the single parallel-spin chiral ABM state or the dual parallel-spin SK state, which is either chiral or non-chiral, depending upon the direction of $\boldsymbol{H}$, although many of the authors were apparently unaware of the proper designation of the latter state they described [49, 51]. For the ABM state, when $\boldsymbol{H}$ is parallel to the antinodal plane, $H_{c2}(T)$ is given by the new form $H_{c2,\mathrm{ABM\ antinodal}}(T)$ [72]. Neither the ABM nor the SK state appears to be consistent with the experiments of $H_{c2,||}(T)$ parallel to the layers of Sr_2RuO_4 [60, 61, 27], which show that $H_{c2,||}(T)$ is strongly Pauli limited [65, 33]. Recent scanning tunneling microscopy on that material were also inconsistent with gap nodes [73]. Regardless of whether Sr_2RuO_4 or some other as yet undiscovered material will be the first manifestation of the SK or ABM states, $\boldsymbol{H}_{c2}(\theta)(T)$ at an arbitrary angle θ with respect to the fixed nodal point direction of the SK or ABM states with the normal state electrons on a general ellipsoidal FS will be presented in this thesis [72].

Yet another p-wave order parameter symmetry is that of the completely broken symmetry (CBS) state

$$\Delta_{\mathrm{CBS}}(\boldsymbol{k}) = \Delta_0 k_z, \Delta_0 k_y, \Delta_0 k_x, \tag{1.23}$$

for which the pairing could be locked onto the x, y, z axes respectively. For the external field $\boldsymbol{H}$ applied in the antinodal direction, H_{c2} is given by $H_{c2,\ \mathrm{p\ antinodal}}(T)$, which is the highest of all the H_{c2}'s. When the field is applied perpendicular to the pairing direction (nodal direction), H_{c2} is given by a $H_{c2,\ \mathrm{p\ nodal}}(T)$ depicted in Fig. 1.1(c). In 2005, Hardy and Huxley [38] reported that the upper critical field of URhGe fit the data using a p-wave polar/CBS symmetry along all three crystallographic directions, with a slight demagnetization jump at T_c shown in Fig. 1.2. The authors noted that the only fitting parameter used was the slope at T_c.

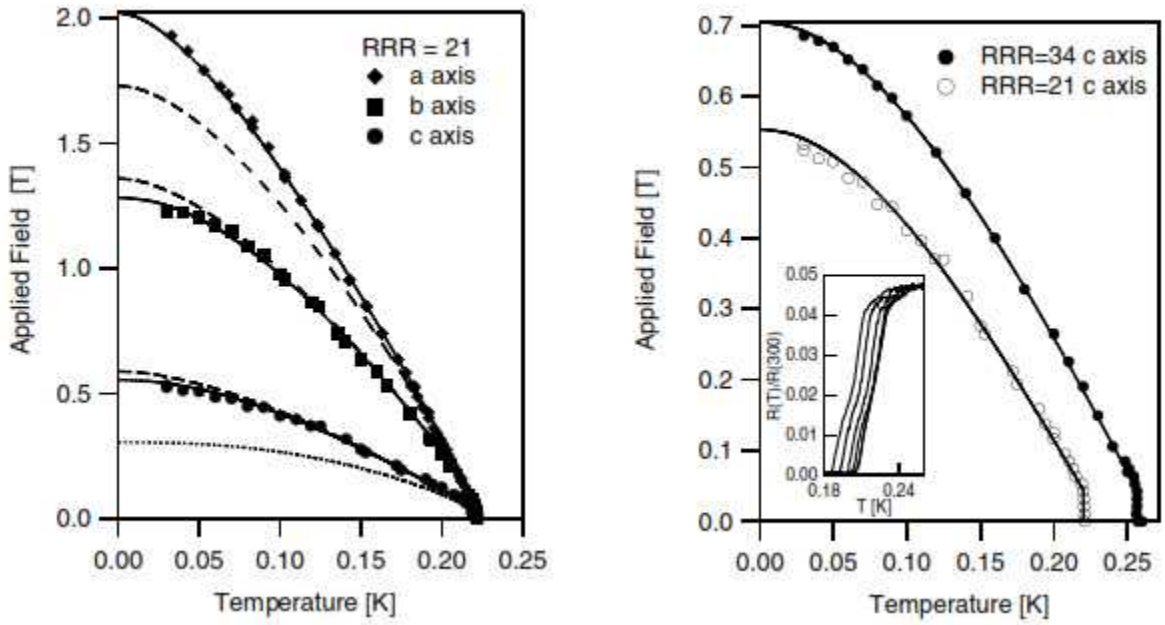

Figure 1.2: (left) The temperature dependence of H_{c2} as reported by Hardy and Huxley [38] for a URhGe sample of RRR=21. Solid lines represent calculated values corresponding to a completely broken symmetry/polar state. Dashed lines are calculated values based on BCS s-wave symmetry without Pauli limiting. The dotted line is a calculated value based on BCS s-wave symmetry with Pauli limiting. (right) Upper critical field data for two samples of URhGe with RRR=34 and RRR=21, with external magnetic field applied along the c-axis direction. Solid lines are fits using the completely broken symmetry state symmetry. Inset shows resistivity data from which the upper critical field was extracted. The demantnetization jumps are evident close to T_c. The only fitting parameter used was the slope at T_c.

The d-vector

Since triplet spin Cooper pairing has a three component spin state given by

$$\chi_{p-wave} = \begin{cases} |\uparrow\uparrow> \\ 1/\sqrt{2}(|\uparrow\downarrow> + |\downarrow\uparrow>), \\ |\downarrow\downarrow> \end{cases} \tag{1.24}$$

and elegant and full description of the pairing can be expressed as a complex vector called the $\boldsymbol{d}$-vector, which is a function of a vector $\hat{\boldsymbol{k}}$ in a certain fixed reference frame.

The Cooper pair wave function may be expressed in terms of the $\boldsymbol{d}$-vector and has the form

$$\Psi = i(\boldsymbol{d}(\boldsymbol{k}) \cdot \boldsymbol{\sigma})\sigma_y = (d_x(\boldsymbol{k})\sigma_x + d_y(\boldsymbol{k})\sigma_y + d_z(\boldsymbol{k})\sigma_z)i\sigma_y, \tag{1.25}$$

which in matrix form is

$$\Psi = \begin{pmatrix} -d_x(\boldsymbol{k}) + id_y(\boldsymbol{k}) & d_z(\boldsymbol{k}) \\ d_z(\boldsymbol{k}) & d_x(\boldsymbol{k}) + id_y(\boldsymbol{k}) \end{pmatrix}, \tag{1.26}$$

where σ_x, σ_y and σ_z are the Pauli matrices.

The simplest example of a $\boldsymbol{d}$-vector is that of the B-phase of superfluid Helium-3, where

$$\boldsymbol{d}(\boldsymbol{k}) \sim \hat{\boldsymbol{k}}. \tag{1.27}$$

Substituting this $\boldsymbol{d}$-vector into Eq. 1.25, we obtain

$$\Psi^B = \begin{pmatrix} -k_x + ik_y & k_z \\ k_z & k_x + ik_y \end{pmatrix}, \tag{1.28}$$

which can be written as

$$\Psi^B = (-k_x + ik_y)\boldsymbol{\alpha} + k_z\boldsymbol{\beta} + (k_x + ik_y)\boldsymbol{\gamma}, \tag{1.29}$$

where $\boldsymbol{\alpha} = \mid \uparrow\uparrow>$, $\boldsymbol{\beta} = \mid \uparrow\downarrow> + \mid \downarrow\uparrow>$, $\boldsymbol{\gamma} = \mid \downarrow\downarrow>$, which is a linear superposition of equally probable states $m_s = 1$, $m_s = 0$, $m_s = -1$.

The axial, or planar phase, which is chiral, has $k_z = 0$ and $\boldsymbol{d}(\boldsymbol{k}) \sim (\hat{k}_x, \hat{k}_y, 0)$ with

$$\Psi^{\text{planar}} = (-k_x + ik_y)\boldsymbol{\alpha} + (k_x + ik_y)\boldsymbol{\gamma}. \tag{1.30}$$

The polar phase, which is non-chrial, has $k_x = k_y = 0$, with $\boldsymbol{d}(\boldsymbol{k}) \sim (0, 0, k_z)$ and

$$\Psi^{\mathrm{polar}} = k_z \boldsymbol{\alpha}. \tag{1.31}$$

The upper critical field, specifically the angular dependence of H_{c2}, for various such phases will be discussed in this thesis.

CHAPTER 2: CANDIDATE P-WAVE SUPERCONDUCTORS

Experiments

Since the discovery of superconductivity in 1911, new exotic materials have been discovered that have been shown to contain mobile electrons that behave as though their mass were $10-1000$ times the value of the electron mass in vacuum; these materials were aptly named "heavy fermion" materials. In such materials, quantum phase transitions arise in highly correlated electron systems because of competing interactions that promote rivaling ground states such as superconductivity and ferromagnetism [36]. Experimental and theoretical research in the area of unconventional p-wave superconductivity has pointed to the strongest candidates for $l = 1$ parallel spin state superconductivity, the heavy fermion materials: UGe_2, UCoGe, URhGe, and UPt_3, the only superconductor that has been definitively shown to have multiple superconducting phases. Other potential candidates such of the new class of topological superconductors, non-centrosymmetric compounds such as UIr and YPtBi, and the widely purported Sr_2RuO_4, although the upper critical field parallel to the layers $H_{c2,\|}$ is Pauli limited and inconsistent with Knight shift measurements in that direction. Some of these heavy fermion materials such as UCoGe and URhGe have been shown to possesses ferromagnetism below a ferromagnetic transition temperature, T_C, and superconductivity below a superconducting transition temperature, $T_c < T_C$, for which the ferromagnetism persists even in the superconducting phase at ambient pressure. Other ferromagnetic materials UGe_2, and UIr have been shown to possess superconducting order within the ferromagnetic state under high pressure. Ferromagnetism and superconductivity were not believed to exist simultaneously in the same crystal. Yet, magnificent materials which possess both ferromagnetism and superconductivity simultaneously, and the same electrons that participate in the ferromagnetism also participate in the superconductivity, were discovered, possessing many unique properties that render them a fruitful

playground to investigate new and exotic physics of strongly correlated matter.

In ferromagnetic superconductors, one can measure the temperature T and orientation dependence of the upper critical field $\boldsymbol{H}_{c2}$, at which the superconductivity is destroyed by the applied magnetic field $\boldsymbol{H}$ in combination with the ferromagnetic spontaneous magnetization $\boldsymbol{M}_0$. However, in such materials, it is more convenient to calculate the upper critical magnetic induction $\boldsymbol{B}_{c2}$, which arises from the complicated interplay of ferromagnetic and diamagnetic superconducting components in the single function $\boldsymbol{B} = \mu_0\boldsymbol{H} + \boldsymbol{M}$, where $\boldsymbol{M}(\boldsymbol{H})$ is the field-dependent magnetization. One can probe the bulk properties of the superconductivity by measuring the T and differently oriented $\boldsymbol{H}$ dependencies of $\boldsymbol{B}_{c2}$ [13, 14, 15, 20, 21, 22, 26].

URhGe

The discovery of superconductivity at ambient pressure was discovered in the weak itinerant ferromagnet URhGe with a Curie temperature of $T_C = 9.5$ K, superconducting transition temperature of $T_c = 0.26$ K, and zero-temperature spontaneous ferromagnetic moment of $M_0 = 0.4\mu_B$, where μ_B is the Bohr magneton, opened new opportunities for studying ferromagnetic superconductors. The crystal structure of URhGe is of the TiNiSi-type and its orthorhmobic structure is depicted in the Fig 2.1.

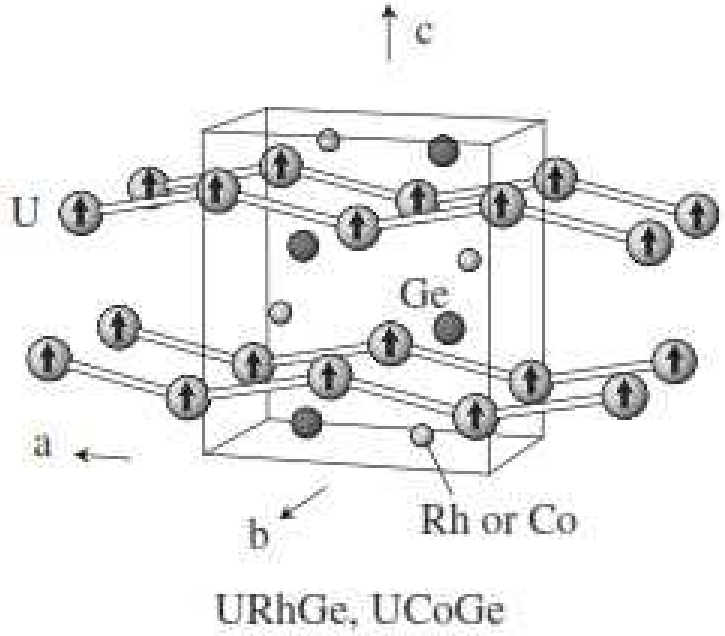

Figure 2.1: Crystal structure of URhGe and its sister compound UCoGe [12]. Arrows indicate the direction of the net spontaneous magntic moment.

Early upper critical field measurements on single crystal samples of URhGe with residual resistance ratio RRR=21 by Hardy and Huxley strongly supported a completely broken symmetry p-wave order parameter shown in Fig 1.2 [38], with $\Delta = \Delta_0 k_z$, for its low field regime ($i.e.$ $\mu_0 H \leq 2$ T). Subsequent experiments showed strong evidence for the reemergence of superconductivity at high fields. This anomalous high-field reentrant superconducting phase was measured in clean samples RRR = 50 [9], where the superconductivity was found to disappear at a relatively low field strength [38], but then reappears when the strength of the external field exceeds 8T [7] shown in Fig. 2.2.

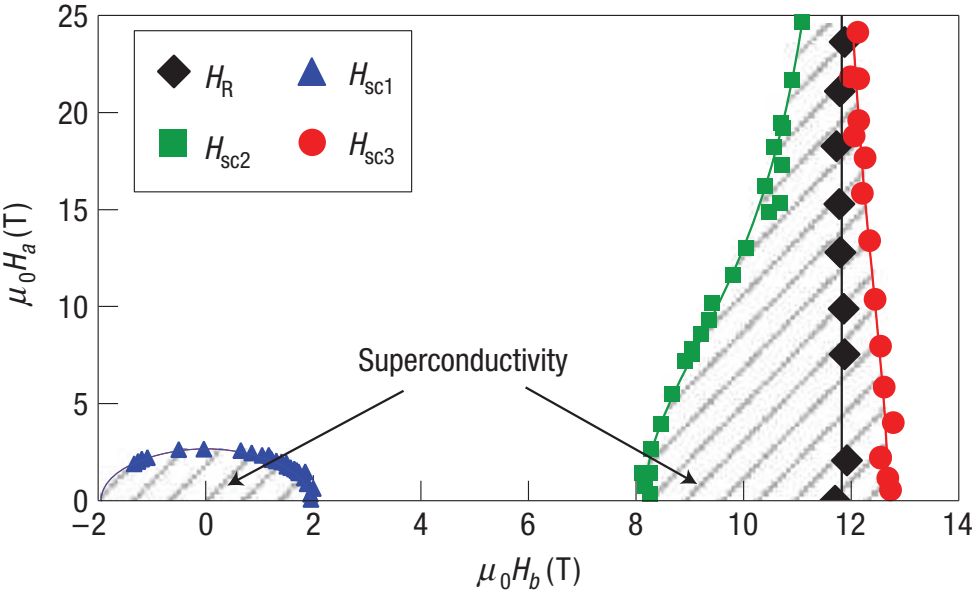

Figure 2.2: H_a/H_b phase diagram of the upper critical field and the higher reentrant critical field of URhGe. Superconductivity occurs below H_{sc1} and between H_{sc2} and H_{sc3}. [7]

Subsequent elastic neutron scattering measurements by Lévy *et al.* [9] showed strong evidence for a realignment of the of the magnetic at high fields. Fig. 2.3 shows strong evidence for a metamagnetic transition which occurs at $\mu_0 H_R = 12$ T, where the magnetic moments suddenly realign themselves from the crystallographic c-axis direction to the b-axis direction. Resistance measurements performed for various temperatures clearly point out the link between the metamagnetic transition and the re-entrant superconductivity.

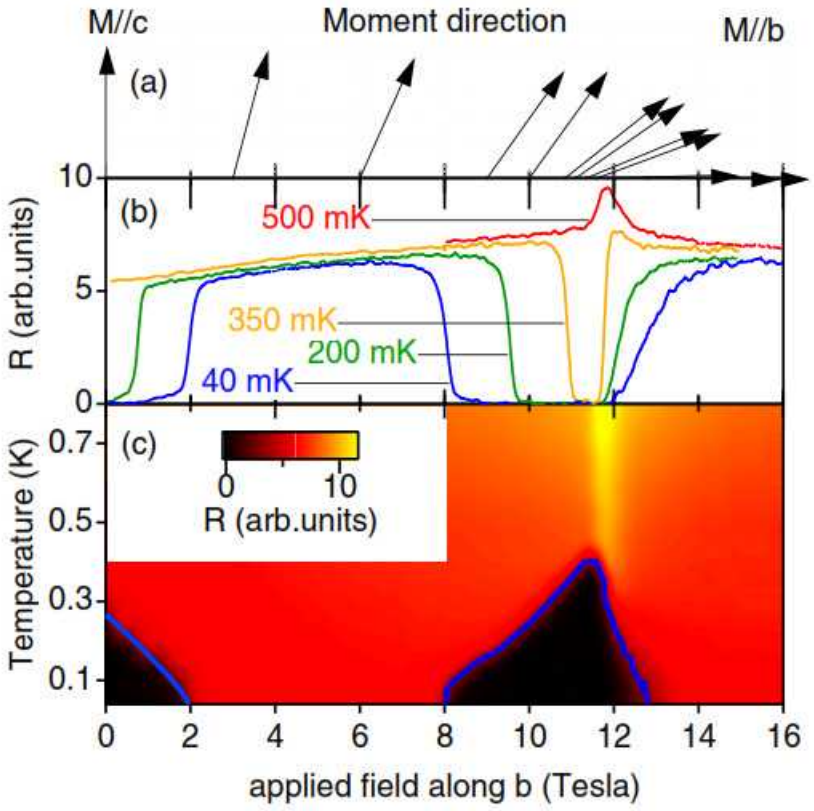

Figure 2.3: Superconductivity and metamagnetic transition for external magnetic field along the b-axis direction of URhGe. (a) Magnetic moment direction established by elastic neutron scattering. At the reorientation field $\mu_0 H_R = 12$ T, the magnetic moments align along the b-axis direction (b) Resistance measurements performed under various temperatures. The reorientation field H_R is indicated by the peak in the resistance for $T = 500$ K. (c) Temperature versus field applied along the b-axis direction for $T = 40$ mK. As seen in (b), two pockets of superconductivity are observed: below $\mu_0 H = 2$ T and between $\mu_0 H = 8 - 13$ T [9].

Angular dependent measurements of $R(\boldsymbol{B})$ at various temperatures later showed evidence of Shubnikov-de-Haas Oscillations (SdH) [27], which provided precise information about the Fermi surface geometry and quasiparticle mass of URhGe under the application of an external magnetic

field. The authors claimed that the re-entrant superconductivity was partly due to a decreasing effective mass, m^* upon application of an external magnetic field.

Magnetization measurements conducted by Aoki $et\ al.$ were seemingly at odds with the conclusions of [8], and revealed anomalous behavior for the b-axis direction at the reorientation field $\mu_0 H = 12$ T shown in Fig. 2.4. Note that at the reorientation field,H_R, the slope of $M(H)$ drastically increases in a 2 T interval, then returns to the slope before the magnetic moment reorientation; $\partial M/\partial H$ is also plotted versus H in Fig. 2.4 showing evidence of a peak centered at H_R.

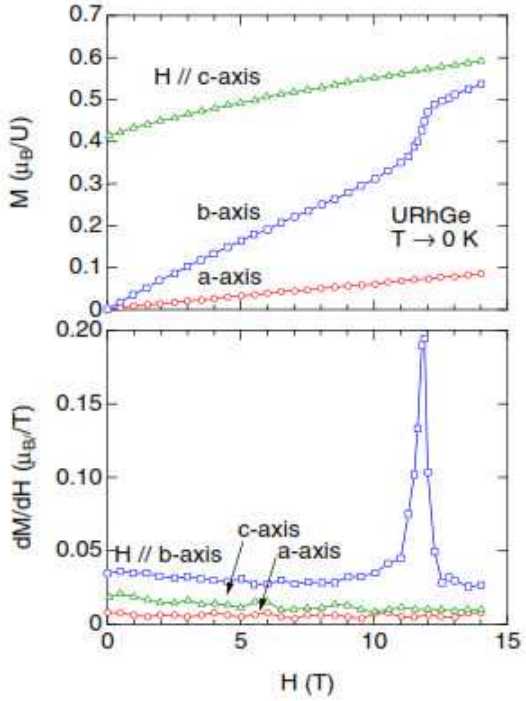

Figure 2.4: Magnetization curves for all three crystal axis directions in URhGe [12]. A sharp change in slope is observed at the reorientation field, $\mu_0 H_R = 12$ T in the b-axis direction. Field derivative of the magnetization along all three crystal axis directions is shown, with a sharp Lorentzian peak observed at H_R for the b-axis direction.

Using the Maxwell relations [12], the authors were able to extract the linear T coefficient $\gamma(\boldsymbol{H})$ of the specific heat. Figure 2.5 depicts the specific heat curves along all three crystallographic axes, and shows evidence of an anomalous peak in γ for the field along the b-axis direction.

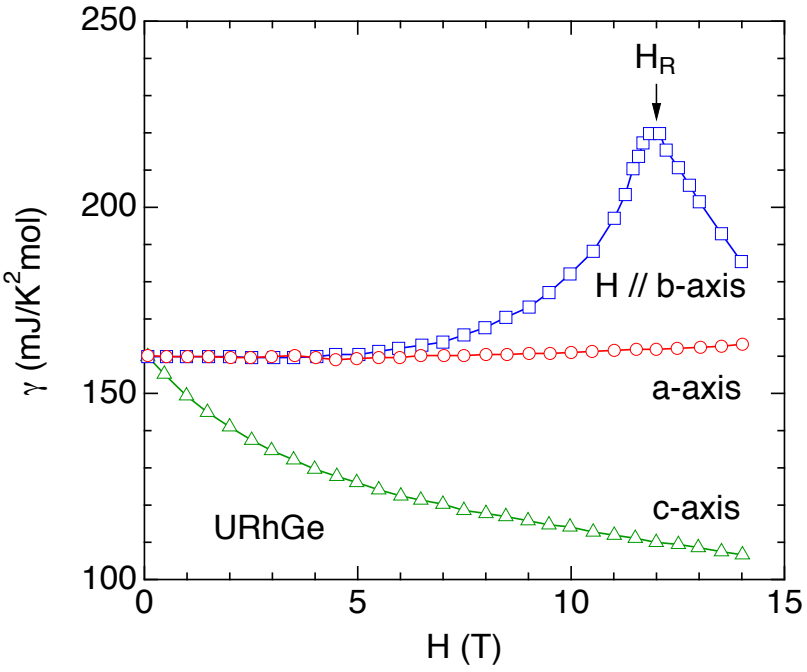

Figure 2.5: Linear T coefficient γ of the specific heat for the field along the a, b, and c axis directions. An anomalous peak occurs in $\gamma_b(\boldsymbol{H})$ at the reorientation field, $H_R = 12$ T [12].

The robustness of the superconductivity in high fields is a signature of parallel-spin pairing, and cannot be easily explained using conventional BCS s-wave pairing, although the exact reason for the reemergence of superconductivity at high fields in URhGe has not yet been pinpointed, and is one of the goals of this thesis. Although Knight shift measurements have not yet been performed in either the high or low-field superconducting states of URhGe, it remains one of the primary candidates for a p-wave superconductor.

UCoGe

Yet another breakthrough in the field of p-wave superconductivity was attained when the heavy fermion compound UCoGe was discovered and found to have anomalous superconducting properties, specifically as exhibited by its upper critical field. UCoGe has the same orthorhombic crystal structure as URhGe with a TiNiSi-type crystal structure shown in Fig.2.1. It has a Curie temperature of $T_C = 3$ K, and a superconducting transition temperature of $T_c = 0.7$ K, with a zero-temperature spontaneous magnetic moment of $M_0 = 0.05\mu_B$, which is much smaller than the ordered moment in URhGe, where μ_B is the Bohr magneton. The onset of the ferromagnetism and superconductivity is signaled by a kink in the resistivity, $\rho(T)$, and peaks in the specific heat C/T, as shown in Fig. 2.6.

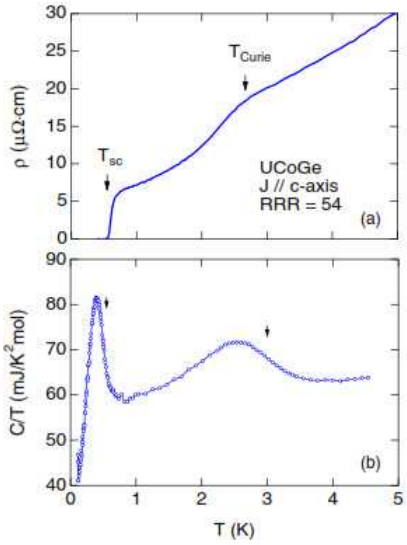

Figure 2.6: Temperature dependence of the resistivity, $\rho(T)$, and specific heat, C/T in UCoGe [12]. Onset of ferromagnetic and superconducting transitions are signaled by kinks in $\rho(T)$, and peaks in C/T.

Since the ferromagnetic transition T_C is very close to the superconducting transition T_c, there is a strong interplay between ferromagnetism and superconductivity. Upper critical field measurements revealed strikingly high values for the extrapolated $H_{c2}(0)$ from the data at ambient pressure and the field along a hard magnetic axis (a or b). As shown in Fig. 2.7, $H^b_{c2}(0) \sim 18$ T, and $H^a_{c2}(0) \sim 30$ T, far exceeding the conventional Pauli limit, providing strong evidence for a parallel spin state.

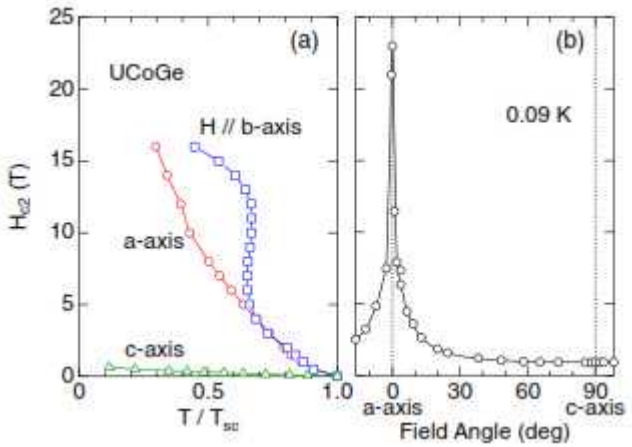

Figure 2.7: (a) Temperature dependence of H_{c2} of UCoGe. Upward curvature is evident in at least two crystal axis directions, with a strong S-shaped H_{c2} enhancement for $\mu_0 H_{\|\hat{\boldsymbol{b}}} > 5$ T. For $\mu_0 H < 5$ T, $H^a_{c2} \sim H^b_{c2}$, showing strong evidence for an axial p-wave state with uniaxial anisotropy [10].

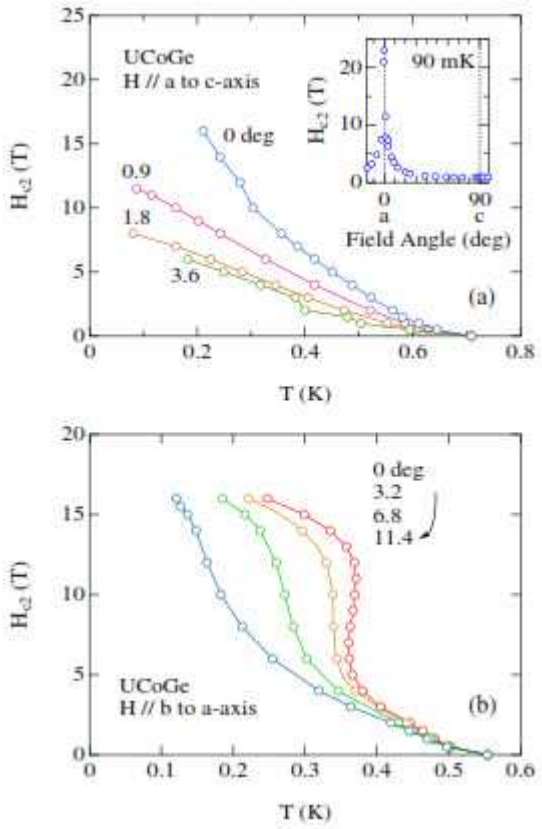

Figure 2.8: (a) Temperature dependence of the upper critical field of UCoGe at various angles measured from the a-axis direction. The upper critical field is strongly suppressed by crystal misalignments of the crystal. The inset shows the full angle dependence of the upper critical field at $T = 90$ mK. (b) Temperature dependence of the upper critical field at various angles measured from the b-axis direction. There is a strong suppression in the S-shaped behavior of H_{c2} for slight misalignments of the crystal [10].

Angle dependent measurements were also conducted showing strong evidence for high sensitivity to sample alignment as shown in Fig 2.8. These studies provide strong evidence that for UCoGe, the order parameter symmetry seems to be closer to that of an axial state or chiral p-wave, of the form $\Delta = \Delta_0(k_x + ik_y)$ or $\Delta = \Delta_+(k_x + ik_y) + \Delta_-(k_x - ik_y)$, than a polar state as in the

case of URhGe. Ambient pressure measurements of the bulk probe $\boldsymbol{B}_{c2}$ and of local probes such as muon depolarization experiments on orthorhombic UCoGe [1, 4] and URhGe [5, 6, 7, 9, 8] showed that the superconductivity exists completely within the ferromagnetic T range and that the same electrons are responsible for the superconductivity and the ferromagnetism [4, 12]. In some non-ferromagnetic p-wave superconductors, such as the purported doped topological insulators, although $\boldsymbol{M}_0 = 0$, there can still be complications due to competing surface and bulk properties. The variety of possible *p*-wave states can still be characterized in those materials by bulk measurements of $\boldsymbol{H}_{c2}(T)$ for a variety of $\boldsymbol{H}$ orientations. Early measurements of H_{c2} in UCoGe showed strong curvature in all three crystallographic directions, with no anisotropy observed in the ab plane, suggesting a pairing mechanism with axial symmetry with the pairing occurring in the ab-plane. More recent measurements were conducted by Dai Aoki $et\ al.$ at the CEA in Grenoble, with clean single crystals of UCoGe and more accurately aligned samples. The spectacular S-shaped behavior of H_{c2} along the b-axis is qualitatively novel. In addition, $\boldsymbol{H}$ along a exhibits pronounced upward curvature, and $\boldsymbol{H}$ along both of these directions violates the Pauli limit by roughly a factor of 20, providing strong evidence for a parallel-spin triplet pair state.

The P/T phase diagram is pictured in the central panel of Fig. 2.9. The high P regime is the first example of a ferromagnetic superconductor that has a superconducting phase combined with a paramagnetic phase, rather than a ferromagnetic phase [94]. Very recent ^{59}Co $K(T)$ measurements in the two non-ferromagnetic field directions with $\boldsymbol{H} \perp \hat{c}$ were performed. These Knight shift measurements are in agreement with the $H_{c2}(T)$ measurements in both of these directions, so in this case, there is no disagreement between any of the experiments. UCoGe is not only a ferromagnetic superconductor, the superconductivity is that of a parallel-spin state.

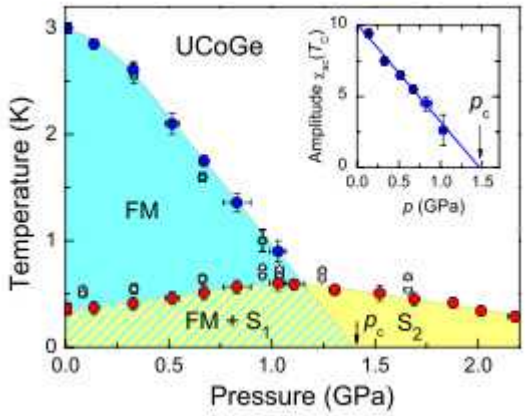

Figure 2.9: P/T phase diagram for UCoGe showing evidence for the coexistence of ferromagnetism and superconductivity at ambient pressure. Upon increasing the pressure, the ferromagnetism is suppressed without quenching the superconductivity [94].

SdH oscillations were also observed in UCoGe. The results suggested a small nearly spherical electron pocket with a heavy mass and low electron density, consistent with one of the Fermi surfaces calculated by Samsel-Czekala $et\ al.$ [95]. These oscillations were observed for field angles in the bc-plane from 0° to 65°, and were field-strength dependent. Polarized neutron diffraction studies of UCoGe have been performed [38]. The authors applied $\boldsymbol{B}||\hat{c}$ with strengths of 3 T and 12 T, respectively, and deduced that for $\boldsymbol{B}||\hat{c}$, a ferrimagnetic state is induced by the field, with the moments on the U and Co sites in opposite directions but with different magnitudes. This is extremely unusual.

UPt_3

To date, the strongest and most complete body of experimental evidence for triplet superconductivity has been compiled for the heavy fermion material UPt_3, which has an hexagonal crystal structure. In the case of UPt_3, measurements of the ultrasound velocity showed multiple superconducting phases. This very interesting material exhibits at least three superconducting phases shown in Fig 2.10, which have been designated the A, B, and C phases. For $\boldsymbol{H} \parallel \hat{\boldsymbol{b}}$ and $\boldsymbol{H} \parallel \hat{\boldsymbol{a}}$, evidence for the three superconducting phases was seen experimentally with the ultrasound velocity measurements of Adenwalla $et\ al.$ [92]. Although it is sometimes claimed to be the quintessential p-wave superconductor, there are still many unsolved mysteries associated with this compound. One such mystery is the inconsistency of the Knight shift K(T) measurements performed by Tou $et\ al.$ [93] and the strongly Pauli limited H_{c2} for $\boldsymbol{H} \parallel \hat{\boldsymbol{c}}$ measured by Shivaram $et\ al.$ [23] For $\boldsymbol{H} \parallel \hat{\boldsymbol{a}}$, no Pauli limiting was observed by Shivaram $et\ al.$ [23], which is consistent with the temperature independent $K(T)$ measured by Tou $et\ al.$ [93] for that field direction. In addition, no long range ferromagnetic order has been observed for UPt_3, in sharp contrast with the ferromagnetic superconductors URhGe and UCoGe, which have upper critical fields which violate the Pauli limit by a factor of 20 in at least one field direction. Future experiments might indicate that UPt_3 might in fact be the quintessential d-wave superconductor that has eluded physicists for a long time.

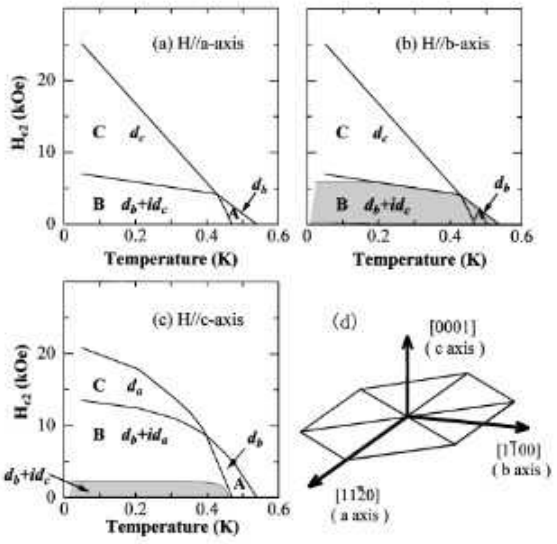

Figure 2.10: Upper critical field of UPt_3 depicting the three superconducting phases of this remarkable material.

Sr_2RuO_4

It is often claimed that the layered superconducting material Sr_2RuO_4 is a triplet p-wave superconductor exhibiting a chiral p-wave order parameter symmetry with antiparallel spin pairs normal to the layers described by a $\boldsymbol{d}$-vector $\hat{\boldsymbol{z}}(k_x \pm ik_y)$. Although many people believe that Sr_2RuO_4 has been definitively shown to exhibit such order parameter symmetry, many issues remain unresolved for this material. Early Knight shift measurements $K(T)$ for Sr_2RuO_4 in the superconducting state for $\boldsymbol{H} \perp \hat{\boldsymbol{c}}$ were also independent of temperature T and consistent with a chiral p-wave order parameter symmetry. Subsequent $K(T)$ measurements for $\boldsymbol{H} \parallel \hat{\boldsymbol{c}}$ were independent of T and inconsistent with this state. It thereafter assumed that as in ^{3}He, the spins and thus the $\boldsymbol{d}$-vector

could rotate with the field, always remaining normal to $\boldsymbol{H}$, and thus explaining the temperature independence of $K(T)$ parallel to $\hat{\boldsymbol{c}}$. Subsequent measurements of $H_{c2}(T)$ by Deguchi $et\ al.$ [60] showed Pauli limiting for $\boldsymbol{H} \parallel$ to the layers, which is in complete disagreement with antiparallel p-wave pairing $\parallel \hat{\boldsymbol{c}}$. Subsequent $H_{c2}(T,\theta)$ measurements were conducted by Kittika $et\ al.$ [61] showing the angle dependence for H_{c2} in the ac-plane. If Sr_2RuO_4 had an order parameter of the form $\Delta = \Delta_0(k_x \pm ik_y)$, $H_{c2}(T, 0^\circ)$ would be given by the Scharnberg-Klemm (SK) state, and $H_{c2}(T, 90^\circ)$ would be given by the polar state. Fits to the data of Kittika $et\ al.$ [61] using various order parameter symmetries with an anisotropic g-tensor and Pauli-limiting will be presented in this thesis.

CHAPTER 3: LOW FIELD UPPER CRITICAL FIELD OF UCoGe

Background

After the discovery of unconventional superconductivity in the heavy fermion URhGe, especially its anomalous reentrant behavior, much interest turned to the mechanism driving such high field superconductivity. Then, superconductivity was discovered in UCoGe [1], and $H_{c2}(T)$ was measured along all three crystallographic directions[2]; the authors observed upward curvature along all three crystallographic directions which could not be linked to dimensional crossover effects [47]. Further investigations on UCoGe revealed the extreme sensitivity of $H_{c2}(T)$ to single crystal purity and alignment. Subsequent measurements were performed on very clean single crystal samples of the material [10], revealing a highly anomalous S-shaped $H_{c2}(T)$ for the external magnetic field applied along the b-axis direction and $T < 0.65T_c$, and upward curvature along the a and c axis directions.

The first attempts to describe upward $H_{c2}(T)$ curvature in all crystal axis directions were based either upon ferromagnetic fluctuations [23], or upon a crossover from one parallel-spin state to another [24]. Meanwhile, a mean-field theory of the complementary effects of itinerant ferromagnetism and parallel-spin superconductivity was developed [25, 26]. To date, the field dependence of this mutual enhancement has not been investigated.

The model

To understand the origin of the upward curvature of $H_{c2}(T)$ for all three crystallographic directions of UCoGe, we study the case in which the p-wave pairing interaction strength is anisotropic,

but finite in all crystal directions. Since H_{c2} is essentially isotropic in the ab plane for samples of UCoGe with medium purity [19], we studied the partially broken symmetry (PBS) state as a function of the pairing interaction anisotropy. This can give a kink in $H_{c2}(T)$ in at least one field direction [27]. We assume a generally anisotropic p-wave pairing interaction of the form

$$V(\boldsymbol{k},\boldsymbol{k'}) = 3\sum_i V_i \hat{\boldsymbol{k}}\cdot\hat{\boldsymbol{x_i}}\hat{\boldsymbol{k'}}\cdot\hat{\boldsymbol{x_i}}|S_i(\hat{\boldsymbol{x_j}})><S_i(\hat{\boldsymbol{x_j}})|, \tag{3.1}$$

where we take $V_3 > V_2 \geq V_1$, and $|S_i(\hat{\boldsymbol{x_j}})>$ are the pair spin states. We assume a clean type II weakly coupled superconductor and use the linearized Gor'kov gap equation

$$\Delta(\boldsymbol{R},\boldsymbol{k}) = 2\pi T\sum_{\omega_n}\int\frac{d\Omega_{k'}}{4\pi}N(0)V(\hat{\boldsymbol{k}},\hat{\boldsymbol{k'}})\int_0^\infty d\xi e^{-2\xi|\omega_n|}e^{-i\xi_{\boldsymbol{k'}}v_F\boldsymbol{k'}\cdot M_{1/2}^{-1}\cdot\boldsymbol{\Pi}(\boldsymbol{R})}\Delta(\boldsymbol{R},\boldsymbol{k'}), \tag{3.2}$$

where $N(0)$ is the density of states per spin at the Fermi energy, ω_n are the fermion Matsubara frequencies, v_F is the Fermi velocity, $\boldsymbol{\Pi}(\boldsymbol{R}) = -i\boldsymbol{\nabla}_{\boldsymbol{R}} + 2e\boldsymbol{A}(\boldsymbol{R})$, $\boldsymbol{A}(\boldsymbol{R})$ is the magnetic vector potential, and $M_{1/2}^{-1}$ is the square root of the inverse effective mass tensor. We expand $\Delta(\boldsymbol{R},\boldsymbol{k})$ in terms of the relevant spherical harmonics and the linear harmonic oscillator wavefunctions,

$$\Delta(\boldsymbol{R},\boldsymbol{k}) = \sum_{n=0}^{\infty}\sum_{m=-1}^{1}|n(\boldsymbol{R})><n(\boldsymbol{R})|\Delta_{1m})>Y_{1m}(\hat{\boldsymbol{k}}), \tag{3.3}$$

and insert this expression in the linearized Gor'kov gap equation, project out the various order parameter components, and perform the integrations, after which we obtain expressions for upper

critical fields of the polar and two axial partially broken symmetry states (PBS) for $\boldsymbol{H} \parallel \hat{\boldsymbol{e_3}}$

$$\langle n|\Delta_{10}\rangle\alpha_n^{(p)} = 0 \tag{3.4}$$

$$(\langle n|\Delta_{1,1}\rangle + \langle n|\Delta_{1,-1}\rangle)\alpha_n^{\pm} = \mp b_{n-2}\langle n-2|\Delta_{1,1}\rangle - b_n\langle n+2|\Delta_{1,-1}\rangle, \tag{3.5}$$

$$\alpha_n^{(p)} = [N(0)V_3]^{-1} - a_n^{(p)} \tag{3.6}$$

$$\alpha_n^{(-)} = [N(0)V_2]^{-1} - a_n^{(a)} \tag{3.7}$$

$$\alpha_n^{(+)} = [N(0)V_1]^{-1} - a_n^{(a)}, \tag{3.8}$$

$$a_p^{(p)} = 3\pi T \sum_{\omega_n} \int_0^{\pi} \sin\theta\cos^2\theta \mathrm{d}\theta \int_0^{\infty} \mathrm{d}\xi \mathrm{e}^{-2\xi|\omega_n|}\mathrm{e}^{-1/2\xi_{12}} L_n(\xi_{12}), \tag{3.9}$$

$$a_a^{(a)} = \frac{3}{2}\pi T \sum_{\omega_n} \int_0^{\pi} \sin\theta \sin^2\theta \mathrm{d}\theta \int_0^{\infty} \mathrm{d}\xi \mathrm{e}^{-2\xi|\omega_n|} \mathrm{e}^{-\frac{1}{2}\xi_{12}} L_n(\xi_{12}), \tag{3.10}$$

$$b_n = \frac{3}{2}\pi T \sum_{\omega_n} \int_0^{\pi} \sin^3\theta \mathrm{d}\theta \int_0^{\infty} \mathrm{d}\xi \mathrm{e}^{-2\xi|\omega_n|} \mathrm{e}^{-\frac{1}{2}\xi_{12}} F_n(\xi_{12}), \tag{3.11}$$

where the superscripts (a) and (p) denote the axial and polar states respectively,

$$\xi_{12} = eH\xi^2 v_F^2 \sin^2\theta (m/m_{12}), \tag{3.12}$$

$m_{12} = \sqrt{m_1 m_2}$, $m = (m_1 m_2 m_3)^{1/3}$, L_n are the Laguerre polynomials,

$$F_n = \sum_{p=0}^{n} \frac{(-z)^{p+1}\sqrt{(n+1)(n+2)}n!}{p!(p+2)!(n-p)!}, \tag{3.13}$$

and $N(0)$ is the single-spin density of states, and we set $\hbar = c = k_B = 1$.

For the field along the $\hat{\boldsymbol{e_1}}$ or $\hat{\boldsymbol{e_2}}$ directions, one rotates the axes by $\pi/2$ about $\hat{\boldsymbol{e_2}}$ or $\hat{\boldsymbol{e_1}}$ respectively and replaces m_{12} with m_{23} or m_{13}, respectively.

Since the low-field $H_{c2}(T)$ data of Huy $et\ al.$ [2] for UCoGe suggest that it has uniaxial symmetry, with $H_{c2} \parallel \hat{\boldsymbol{a}} \approx H_{c2} \parallel \hat{\boldsymbol{b}}$ in the following we will restrict our consideration to the $V_1 = V_2$ case [19]. In order to fit the Aoki $et\ al.$ [11] data with the S-shaped $H_{c2,\|b}(T)$ curve, it is necessary to use the full orthorhombic anisotropy in Eqs. (3.4, 3.5, 3.9-3.11), and to include the spontaneous

and field-dependent magnetization. To do so for the two axial states, one may obtain a recursion relation for either one of the amplitudes, $\langle n|\Delta_{1,\pm 1}\rangle$ by eliminating the other in Eq. (3.5), and then solving the recursion relation in terms of a continued fraction. In Fig. 3.1, we plot $h_{c2,\|c} = 2eH_{c2}(m/m_{12})v_F^2/(2\pi T_c^c)^2$ versus $t = T/T_c$ for the polar state and for a variety of PBS states with $0.25 \leq \delta < 0$, where $\delta = \ln(T_c^{ab}/T_c^c)$. Note that these PBS states all have slight upward curvature, but since $T_c^c > T_c^{ab}$, the polar state dominates for all $T \leq T_c^c$. In Fig. 3.2, we plot $h_{c2} = 2eH_{c2}(m/\sqrt{m_{12}m_3})v_F^2/(2\pi T_c^c)^2$ versus $t = T/T_c$ for the CBS state and for various PBS states with $0.25 \leq \delta < 0$. In this case, the CBS state dominates near to T_c, but there is a crossover to a PBS state for $0.179 \leq \delta < 0$, resulting in a single kink in $H_{c2,\perp c}$.

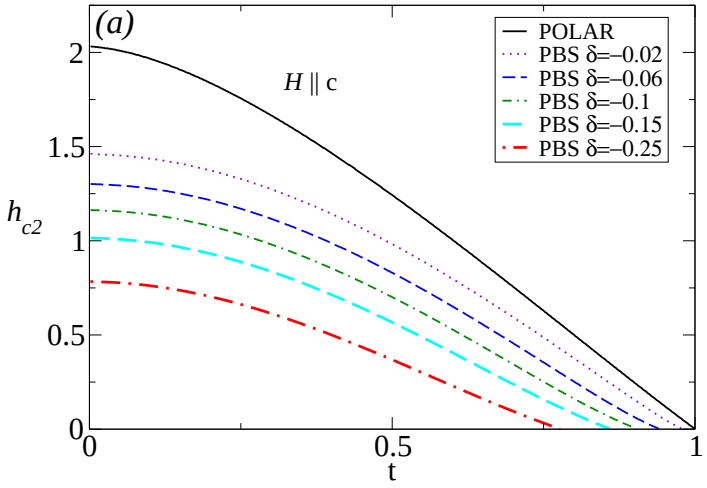

Figure 3.1: Plots of $h_{c2,\|,c} = 2eH_{c2}(m/m_{12})v_F^2/(2\pi T_c^c)^2$ versus $t = T/T_c^c$ for the polar state (solid black) and for a variety of PBS states with $-0.25 < \delta = \ln(\mathrm{T_c^{ab}/T_c^c}) < -0.02$.

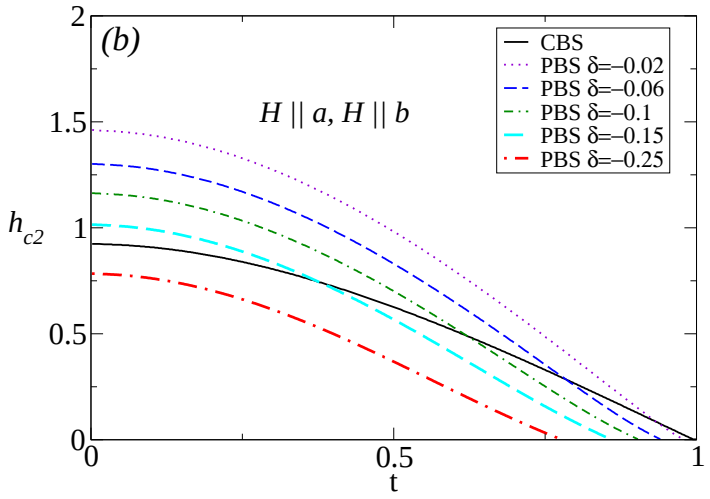

Figure 3.2: Plots of $h_{c2,\perp,c} = 2eH_{c2}(m/\sqrt{m_{12}m_3})v_F^2/(2\pi T_c^c)^2$ versus $t = T/T_c^c$ for the CBS state (solid black) and for various PBS states with $-0.25 < \delta < -0.02$.

Fits to the low-field H_{c2} data of Huy $et\ al.$

As a starting point, to see if there is any possibility of fitting the least anomalous region of the $H_{c2}(T)$ curves obtained for UCoGe, we assume uniaxial anisotropy and fit the data of Huy $et\ al.$ [2]. In Fig. 3.3, the best fit to the $H \parallel \hat{\boldsymbol{c}}$ data is for the polar state, as shown. In Fig. 3.4, the best fits to the $H \parallel \hat{\boldsymbol{a}}$ and $H \parallel \hat{\boldsymbol{b}}$ data are both for $\delta = 0.07$, which show a distinct crossover from the CBS to the PBS state. This δ value is also consistent with the polar state best fit to the $H_{c2,\parallel c}$ data in Fig. 3.3. We remark that when the spontaneous magnetization along the c-axis direction is included, the fitting to the data in Fig. 3.3 would be altered.

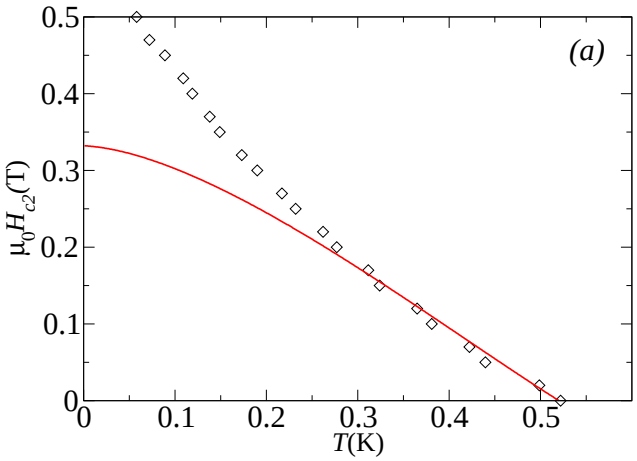

Figure 3.3: Best fits to the Huy $et\ al.$ data for $\mu_0 H_{c2}(T)$ in medium purity UCoGe for $\hat{\boldsymbol{H}} \parallel \hat{\boldsymbol{c}}$. Open black diamonds: data. The solid red curve is for the polar state.

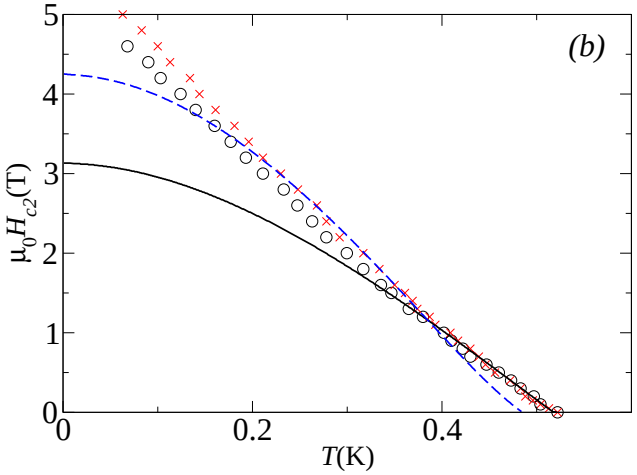

Figure 3.4: Data for $\hat{\boldsymbol{H}} \parallel \hat{\boldsymbol{b}}$ (red crosses) and $\hat{\boldsymbol{H}} \parallel \hat{\boldsymbol{a}}$ (open black circles). The solid black and blue dashed lines are for the CBS state and the polar state with $\delta = -0.07$, respectively. The slopes at T_c were adjusted to fit the data.

We found that it is possible to fit the upward curvature of the $H_{c2}(T)$ data for $H \parallel \hat{\boldsymbol{a}}$ and $H \parallel \hat{\boldsymbol{b}}$ from medium-purity UCoGe using a crossover from the completely broken symmetry polar state to a PBS state. However, in the model studied, it is not possible to fit the observed upward curvature of $H_{c2}(T)$ for $H \parallel \hat{\boldsymbol{c}}$ as the polar state alone provides the best fit to the data. At the very least, the spontaneous and field-dependent magnetization should be included in future fits, using an anisotropic itinerant ferromagnetic superconductor model similar to that previously studied [25, 26].

CHAPTER 4: ANGULAR DEPENDENT UPPER CRITICAL FIELD CALCULATIONS OF THE POLAR/CBS STATE

Background

In this section we present the angular dependent upper critical field calculations for the case of an anisotropic p-wave pairing interaction with equal-spin pairing along only one direction, the one-dimensional (1D) analog of $V_{3D}(\hat{\boldsymbol{k}}, \hat{\boldsymbol{k}}')$, or $V_{1D}(\hat{\boldsymbol{k}}, \hat{\boldsymbol{k}}') = V_0 \hat{k}_z \hat{k}'_z$ [14]. This state, $\Delta_0 k_z$, has come to be known as the polar/CBS state, for a polar state of completely broken rotational symmetry, analogous to the Ising interaction representing the dominant easy-axis component of the highly anisotropic 3D Heisenberg spin-spin interaction. A sketch of the polar/CBS gap function is given in Fig. 1.1. As for the ABM or SK superconducting states in a crystal, the 1D pairing is fixed to the crystal lattice, but in this case, to one crystal axis direction only. The largest intrinsic anisotropy due solely to the order parameter arises between the field applied parallel and perpendicular to this single pairing direction. If the field is along the pairing or antinodal direction, as in the 3D case, one obtains $H_{c2,\mathrm{p\ antinodal}}(T)$ [13]. However, when the field is applied in the planar nodal direction perpendicular to the pairing, then $H_{c2}(T)$ has a distinctly different form, $H_{c2,\mathrm{planar\ nodal}}(T)$, similar to but not identical to $H_{c2,s}(T)$ [14]. Summarizing the various cases evaluated prior to this work, we have for all T with pairing on spherical FSs [13, 14, 72],

$$H_{c2,\mathrm{p\ antinodal}} > H_{c2,\mathrm{SK\ nodal}} > H_{c2,\mathrm{ABM\ antinodal}} > H_{c2,s} > H_{c2,\mathrm{planar\ nodal}} > H_{c2,\mathrm{ABM\ nodal}}. \quad (4.1)$$

The angular dependence of either $\boldsymbol{H}_{c2}(T)$ or $\boldsymbol{B}_{c2}(T)$ for the 1D polar/CBS state case is important to aid experimentalists in determining its realization in materials such as URhGe. These new results are the focus of this paper. Since URhGe, the existing material for which this polar/CBS state has

been strongly supported by experiment [6], has an orthorhombic crystal structure [17, 18, 19, 12], its FS can be approximated as a general ellipsoid. Although the critical field data of UCoGe are more suggestive of an SK or ABM state at low $\boldsymbol{H}$ values, its crystal structure is also orthorhombic [12]. Hence, we have derived the prescription for including general ellipsoidal FS anisotropies into microscopic calculations of $B_{c2}(T)$ for a general anisotropic pairing interaction $V(\hat{\boldsymbol{k}}, \hat{\boldsymbol{k}}')$, and with the magnetic induction $\boldsymbol{B}$ in a general direction. The details of the derivation are presented in the appendix. We use this procedure here to calculate the full angular dependence of $B_{c2}(\theta, \phi, T)$ for the polar/CBS state of a ferromagnetic superconductor dominated by a single parallel-spin state, and our results are presented.

$\boldsymbol{B}_{c2}(T)$ measurements on a URhGe samples with a residual resistance ratio (RRR) = 21 were fit to the Scharnberg-Klemm theory of the p-wave polar/CBS state along all three crystallographic directions, with equal spin pairing along the a-axis direction and weak ferromagnetism along the c-axis direction in the low-field regime, using the resistively measured slopes of B_{c2} along the a-, b-, and c-axis directions just below the ferromagnetic demagnetization jumps at T_c as the only fitting parameters [6]. The measured $B_{c2,a}(T)$ fit the predicted $H_{c2,\mathrm{p\,antinodal}}(T)$ behavior, but $B_{c2,b}(T)$ and $B_{c2,c}(T)$ fit the qualitatively different $H_{c2,\mathrm{planar\,nodal}}(T)$ curve [14], with a constant ratio $B_{c2,b}(T)/B_{c2,c}(T)$ consistent with T-independent FS anisotropy. $B_{c2}(0)$ in all three crystal directions violated the Pauli limit $B_P \sim 1.85T_c$ T/K for a singlet-spin s-wave superconductor [6], indicating that URhGe is very unlikely to be an s- or d-wave superconductor. Consequently, these data provided strong evidence that the superconducting order parameter is likely to have the simplest parallel-spin p-wave orbital form $\hat{\boldsymbol{d}}k_a$ consistent with ferromagnetism in the bc plane of an orthorhombic crystal, where the pair-spin vector $\hat{\boldsymbol{d}} = (\hat{\boldsymbol{b}} + i\hat{\boldsymbol{c}})/\sqrt{2}$, and the p-wave pairing interaction fixed to the crystal a-axis direction for all $\boldsymbol{M}(\boldsymbol{H}) \perp \hat{\boldsymbol{a}}$ directions and the two possible parallel-spin states indicated by $\hat{\boldsymbol{b}} = |\uparrow\uparrow\rangle$ and $\hat{\boldsymbol{c}} = |\downarrow\downarrow\rangle$ [16].

Subsequent measurements on a URhGe sample with RRR = 50 [7] observed an anomalous high

$\boldsymbol{H}||\hat{\boldsymbol{b}}$ reentrant superconducting phase [7], further supporting the idea of a p-wave parallel spin state. But the low-field regime $B_{c2}(\theta, \phi = 0^{\circ})$ within the ab plane was consistent with ordinary FS anisotropy, at least within the experimental resolution [7]. At first sight, these results appear to be in contradiction with the earlier measurements of B_{c2} in URhGe [6].

Note that these results are different than those obtained from hexagonal UPt_3, which has antiferromagnetic domains with the magnetic ordering along the a-axis direction, and for $\boldsymbol{H} \perp \hat{\boldsymbol{c}}$, the resulting $H_{c2,\perp \boldsymbol{c}}(T)$ is consistent with that of the p-wave polar state [14, 23, 24]. For $\boldsymbol{H}||\hat{\boldsymbol{c}}$, the $H_{c2,||\boldsymbol{c}}(T)$ measurements of Shivaram *et. al.* [23] and the calculations of Choi and Sauls [24] fit that of the polar state with Pauli pair breaking for the anti-parallel spin triplet state [22, 23, 24]. UPt_3 has three superconducting phases, and appears to contain some amount of all three triplet spin states [22, 24, 25].

The model

In light of these experimental results, we calculate $B_{c2}(\theta, \phi, T)$ for a ferromagnetic superconductor with $T_{\rm Curie} > T_c$ and p-wave polar/CBS symmetry. Since all three low-field $B_{c2}(T)$ curves for the RRR = 21 crystal of URhGe have different slopes at T_c, the simplest possible FS to consider is an ellipsoidal one, with $\epsilon(\boldsymbol{k}) = \sum_{i=1}^{3} k_i^2/(2m_i)$, having three different single particle effective masses m_1, m_2, and m_3, appropriate for orthorhombic symmetry. We calculate B_{c2} within the ab-plane for the RRR = 21 and 50 URhGe crystals, and predict that under some conditions, a non-monotonic $B_{c2}(\theta, \phi)$ curve with a double peak at $0^{\circ} < \theta^{*} < 90^{\circ}$ and $180^{\circ} - \theta^{*}$ at fixed ϕ could arise, providing a definitive bulk test of the orbital symmetry of the order parameter. Our method is applicable to superconductors of any order parameter symmetry.

For our B_{c2} calculations, we assume the strong spin-orbit interaction splits the FS into two FSs,

each with only one spin state $\uparrow$ or $\downarrow$, and neglect the $\downarrow$ FS, as if the material were nearly a half metal. We further assume weak coupling for a clean homogeneous type-II parallel-spin $\uparrow$ p-wave superconductor with effective Hamiltonian [13, 14],

$$\begin{aligned} \mathcal{H} &= \sum_{\boldsymbol{k}} a^{\dagger}_{\boldsymbol{k},\uparrow}[\epsilon(\boldsymbol{k}-e\boldsymbol{A})-\mu_{\uparrow}(B)]a_{\boldsymbol{k},\uparrow} \\ &\quad +\frac{1}{2}\sum_{\boldsymbol{k},\boldsymbol{k}'} a^{\dagger}_{\boldsymbol{k}',\uparrow}a^{\dagger}_{\boldsymbol{k},\uparrow}V_{\uparrow\uparrow}(\hat{\boldsymbol{k}},\hat{\boldsymbol{k}}')a_{\boldsymbol{k},\uparrow}a_{\boldsymbol{k}',\uparrow}, \qquad (4.2) \\ V_{\uparrow\uparrow}(\hat{\boldsymbol{k}},\hat{\boldsymbol{k}}') &= 3V_{\uparrow\uparrow,0}\hat{k}_a\hat{k}'_a\hat{\boldsymbol{d}}\cdot\hat{\boldsymbol{d}}^{*} = 3V_{\uparrow\uparrow,0}\hat{k}_a\hat{k}'_a, \qquad (4.3) \end{aligned}$$

where e is the electronic charge, $\hat{\boldsymbol{d}}$ is the vector representing the $|\uparrow\uparrow\rangle$ pair spin states on the $\uparrow$ FS with chemical potential $\mu_{\uparrow}(B) = \mu - g\mu_B B/2$ including the Zeeman interaction, where μ_B is the Bohr magneton, $g = 2$ is assumed to be isotropic, and unit wave vectors are defined on the ellipsoidal $\uparrow$ FS to be

$$\hat{k}_i \equiv \frac{\sqrt{2m_i}}{\alpha(\theta,\phi)}\frac{\partial}{\partial k_i}\sqrt{\epsilon(\boldsymbol{k})}\big|_{\epsilon(\boldsymbol{k})=\mu_{\uparrow}(B)}, \qquad (4.4)$$

where

$$\alpha(\theta,\phi) = [\overline{m}_1\sin^2\theta\cos^2\phi + \overline{m}_2\sin^2\theta\sin^2\phi + \overline{m}_3\cos^2\theta]^{1/2}, \qquad (4.5)$$

$\overline{m}_i = m_i/m$, $m = (m_1m_2m_3)^{1/3}$, and we set $\hbar = k_B = 1$. The ellipsoidal $\uparrow$ FS is assumed to be the best approximation to that FS piece most relevant for the superconductivity that can lead to analytic solutions of $\boldsymbol{B}_{c2}$ [17, 18, 19]. The orbital symmetry of the equal-spin pairing interaction is that of a p wave locked onto the $\hat{\boldsymbol{a}} \equiv \hat{\boldsymbol{e}}_3$ axis of an orthorhombic crystal with $\boldsymbol{M}_0||\hat{\boldsymbol{c}}$ on an ellipsoidal FS containing single-particle effective masses m_i along the orthogonal $\hat{\boldsymbol{e}}_i$ directions, respectively [16]. The presence of $\alpha(\theta,\phi)$ in Eq. (4.4) is necessary to insure that the transformed unit wave vectors are normal to the transformed spherical $\uparrow$ FS, and that T_c does not depend upon

the direction of $\boldsymbol{B}$ when $\boldsymbol{B} = 0$. Here $\alpha(\theta, \phi)$ contains the same effective mass directional dependencies as does the anisotropic Ginzburg-Landau (AGL) model [44, 33], although the m_i in this model differ in principle from the analogous AGL model values, and can also be different on the two spin-orbit split FSs. Since in this paper we only treat the $\uparrow$ FS, we drop the spin subscripts to simplify the notation.

The spins are quantized along $\boldsymbol{B} = B\,(\sin\theta\cos\phi, \sin\theta\sin\phi, \cos\theta) = \boldsymbol{\nabla} \times \boldsymbol{A} = \mu_0 \boldsymbol{H} + \boldsymbol{M}$, including $\boldsymbol{M}_0$ for the ferromagnetic superconductor [6], which we assume is non-vanishing at and below T_c. We neglect additional spin-orbit coupling effects that may tie the spin quantization axes to the wave vector directions, since we are only interested in parallel-spin pair states, for which the effects of spin-orbit coupling on the Zeeman energy do not significantly affect B_{c2}.

We begin with the mean-field equations of motion for the finite T Green function matrix components in the presence of $\boldsymbol{B}$ [13], generalized to an ellipsoidal FS,

$$\Big[i\omega_n - \sum_{j=1}^{3} \frac{1}{2m_j}\Big(\nabla_j/i - eA_j(\boldsymbol{r})\Big)^2 + \mu_\sigma(B)\Big] G_{\sigma\sigma'}(\boldsymbol{r}, \boldsymbol{r}', \omega_n) + \sum_{\rho} \int d^3\boldsymbol{\xi}\, \Delta_{\sigma\rho}(\boldsymbol{r}, \boldsymbol{\xi}) F^{\dagger}_{\rho\sigma'}(\boldsymbol{\xi}, \boldsymbol{r}', \omega_n) = \delta_{\sigma\sigma'}\delta^3(\boldsymbol{r} - \boldsymbol{r}'), \quad (4.6)$$

$$\Big[-i\omega_n - \sum_{j=1}^{3} \frac{1}{2m_j}\Big(i\nabla_j - eA_j(\boldsymbol{r})\Big)^2 + \mu_\sigma(B)\Big] F^{\dagger}_{\sigma\sigma'}(\boldsymbol{r}, \boldsymbol{r}', \omega_n) - \sum_{\rho} \int d^3\boldsymbol{\xi}\, \Delta^*_{\sigma\rho}(\boldsymbol{r}, \boldsymbol{\xi}) G_{\rho\sigma'}(\boldsymbol{\xi}, \boldsymbol{r}', \omega_n) = 0. \quad (4.7)$$

where

$$\Delta_{\sigma\sigma'}(\boldsymbol{r}, \boldsymbol{r}') = \delta_{\sigma\sigma'} V_{\sigma\sigma}(\boldsymbol{r} - \boldsymbol{r}') F_{\sigma\sigma}(\boldsymbol{r}, \boldsymbol{r}', 0^+) \quad (4.8)$$

is the mean-field order parameter in position and imaginary time (τ) space and the ω_n are the

fermion Matsubara frequencies, the Fourier series transform variables of τ. Here and in the appendix, we have kept the spin subscripts merely to keep track of the various Green function matrix element factors for future reference, but we are presently only considering the $|\uparrow\uparrow\rangle$ spin state.

To study the full angle dependence of $B_{c2}(\theta,\phi)$, we implement the Maxwell equation-preserving Klemm-Clem (KC) transformations [44, 33], which are exact in the AGL model, and were subsequently applied to a microscopic calculation of B_{c2} in *d*-wave superconductors with $m_1 = m_2 < m_3$ [34]. Here we use them to calculate the effects of a general ellipsoidal FS on B_{c2} for a *p*-wave superconductor in the polar/CBS state, for which the order parameter anisotropy has a much stronger effect upon $B_{c2}(\theta,\phi)$ than in those d-wave cases [34]. The first KC transformation is an anisotropic scale transformation that changes the ellipsoidal FS into a spherical FS [33, 44]. This also changes $\boldsymbol{B}$ to $\boldsymbol{B}' = B'(\sin\theta'\cos\phi', \sin\theta'\sin\phi', \cos\theta')$, where θ' and ϕ' are given in the appendix. Then, one rotates $\hat{\boldsymbol{B}}'$ to the crystal z' axis. Finally, one applies an isotropic scale transformation involving $\alpha(\theta,\phi)$ [33, 44].

After imposing gauge invariance, making use of the Helfand-Werthamer procedure based upon a Feynman theorem [85], and Fourier transformation of the KC-transformed real-space to KC-transformed momentum-space variables, we obtain the single parallel-spin $(\uparrow\uparrow)$ linearized gap equation. The details of these calculations, including corrections of typos in the literature, are given in the appendix [13, 85]. We thus obtain,

$$\overline{\tilde{\Delta}}(\tilde{\boldsymbol{R}},\hat{\tilde{\boldsymbol{k}}}) \;=\; T\sum_{\omega_n}\frac{N(0)}{2}\int d\Omega_{\tilde{\boldsymbol{k}}'}\tilde{V}(\hat{\tilde{\boldsymbol{k}}},\,\hat{\tilde{\boldsymbol{k}}}')\int_0^\infty d\xi_{\tilde{\boldsymbol{k}}'}e^{-2\xi_{\tilde{\boldsymbol{k}}'}|\omega_n|}e^{-i\xi_{\tilde{\boldsymbol{k}}'}v_F\,\hat{\tilde{\boldsymbol{k}}}'\cdot\tilde{\boldsymbol{\Pi}}(\tilde{\boldsymbol{R}})}\overline{\tilde{\Delta}}(\tilde{\boldsymbol{R}},\,\hat{\tilde{\boldsymbol{k}}}'), \quad (4.9)$$

where $\overline{\tilde{\Delta}}$ is the transformed $\Delta_{\uparrow\uparrow}$ amplitude without the gauge phases, $N(0) = mk_F/(2\pi^2)$ is the density of states per spin at the chemical potential $\mu_\uparrow(\tilde{B}_3)$ for an effectively isotropic metal with a geometric mean mass m, effective Fermi wave vector $k_F = \sqrt{2m\mu_\uparrow(\tilde{B}_3)}$, effective Fermi velocity

$v_F = k_F/m$, and

$$\tilde{\mathbf{\Pi}}(\tilde{\boldsymbol{R}}) \;=\; -i\alpha\tilde{\boldsymbol{\nabla}}_{\tilde{\boldsymbol{R}}} + 2e\tilde{\boldsymbol{A}}(\tilde{\boldsymbol{R}}), \tag{4.10}$$

where $\alpha(\theta,\phi)$ is given by Eq.(4.5). We also define the anisotropy function

$$\gamma^2(\phi) \;=\; \frac{m_3}{m_1\cos^2\phi + m_2\sin^2\phi}, \tag{4.11}$$

so that $\alpha = \sqrt{\overline{m_3}}\sqrt{\cos^2\theta + \gamma^{-2}(\phi)\sin^2\theta}$. The KC transformations also modify the effective pairing interaction to become

$$\tilde{V}(\hat{\tilde{\boldsymbol{k}}},\,\hat{\tilde{\boldsymbol{k}}}') \;=\; 3V_0(\hat{\tilde{k}}_3\cos\theta' - \hat{\tilde{k}}_2\sin\theta')(\hat{\tilde{k}}'_3\cos\theta' - \hat{\tilde{k}}'_2\sin\theta'), \tag{4.12}$$

where $\cos\theta' = \sqrt{\overline{m_3}}\cos\theta/\alpha$. For an isotropic $\boldsymbol{g}$ tensor, $\tilde{B}_3 = B$ as the KC transformations do not modify $\mu_\uparrow(B)$.

The transformations have two overall effects: First, $B \to B\alpha(\theta,\phi)$ due to the transformed eigenvalues obtained from the transformed harmonic oscillator operator $\tilde{\mathbf{\Pi}}(\tilde{\boldsymbol{R}})$, modifying the slope of B_{c2} at T_c due to effective mass anisotropy, even for an s-wave superconductor [44, 33, 34, 85, 35]. Second, the rotation changes $V(\hat{\boldsymbol{k}},\hat{\boldsymbol{k}}')$ to $\tilde{V}(\hat{\tilde{\boldsymbol{k}}},\,\hat{\tilde{\boldsymbol{k}}}')$, given by Eq. (4.12). This differently alters $B_{c2}(\theta,\phi,T)$ from that of its slope at T_c.

We then expand $\Delta(\tilde{\boldsymbol{R}},\hat{\tilde{\boldsymbol{k}}})$ in terms of vortex harmonic oscillator states just below B_{c2} [13, 14],

$$\Delta(\tilde{\boldsymbol{R}},\hat{\tilde{\boldsymbol{k}}}) \;=\; (\hat{\tilde{k}}_3\cos\theta' - \hat{\tilde{k}}_2\sin\theta')\sum_{n=0}^{\infty} a_n|n(\tilde{\boldsymbol{R}})\rangle, \tag{4.13}$$

and obtain a general recursion relation for the expansion coefficients a_n,

$$\Gamma_n a_n = \frac{1}{2}\sin^2\theta'(\beta_n a_{n+2} + \beta_{n-2}a_{n-2}), \tag{4.14}$$

$$\Gamma_n = -\ln t + \cos^2\theta'\alpha_n^{(p)} + \sin^2\theta'\alpha_n^{(a)}, \tag{4.15}$$

$$\alpha_n^{(p,a)} = \pi T\sum_{\omega_n}\int_0^\pi d\theta_{\tilde{\boldsymbol{k}}'}\sin\theta_{\tilde{\boldsymbol{k}}'}\left(3\cos^2\theta_{\tilde{\boldsymbol{k}}'}, \frac{3}{2}\sin^2\theta_{\tilde{\boldsymbol{k}}'}\right) \times\int_0^\infty d\xi_{\tilde{\boldsymbol{k}}'}e^{-2\xi_{\tilde{\boldsymbol{k}}'}|\omega_n|}e^{-\eta_{\tilde{\boldsymbol{k}}'}/2}L_n(\eta_{\tilde{\boldsymbol{k}}'}), \tag{4.16}$$

$$\beta_n = \pi T\sum_{\omega_n}\int_0^\pi d\theta_{\tilde{\boldsymbol{k}}'}\frac{3}{2}\sin^3\theta_{\tilde{\boldsymbol{k}}'}\int_0^\infty d\xi_{\tilde{\boldsymbol{k}}'}e^{-2\xi_{\tilde{\boldsymbol{k}}'}|\omega_n|} \times e^{-\eta_{\tilde{\boldsymbol{k}}'}/2}(-\eta_{\tilde{\boldsymbol{k}}'})L_n^{(2)}(\eta_{\tilde{\boldsymbol{k}}'})[(n+1)(n+2)]^{-1/2}, \tag{4.17}$$

where

$$\eta_{\tilde{\boldsymbol{k}}'} = eB\alpha(\theta,\phi)v_F^2\xi_{\tilde{\boldsymbol{k}}'}^2\sin^2\theta_{\tilde{\boldsymbol{k}}'}, \tag{4.18}$$

$t = T/T_c$, $T_c = (2e^C\omega_0/\pi)\exp(-1/N(0)V_0)$, ω_0 is a characteristic pairing cutoff frequency, $C \approx 0.5772$ is Euler's constant, and $L_n(z)$ and $L_n^{(2)}(z)$ are a Laguerre and an associated Laguerre polynomial, respectively.

The recursion relation for the a_n differs from that obtained previously for the polar/CBS state for $\boldsymbol{B}$ in the nodal planar direction [14] only by the general θ' and by $B \to B\alpha(\theta,\phi)$. Solving it iteratively, $B_{c2}(\theta,\phi,t)$ is implicitly obtained from the continued-fraction equation,

$$\Gamma_0 - \frac{\frac{1}{4}\sin^4\theta'\beta_0^2}{\Gamma_2 - \frac{\frac{1}{4}\sin^4\theta'\beta_2^2}{\Gamma_4\cdots}} = 0. \tag{4.19}$$

Usually, 4 or 5 iterations yield sufficient accuracy to detect the unusual effects described in the following.

In Fig. 4.1(a), the reduced (dimensionless) magnetic induction $b_{c2} = 2eB_{c2}v_F^2/(2\pi T_c)^2$ is plotted versus t for a spherical FS [$\gamma^2(\phi) = 1$] and θ values increasing from 0° [at which $b_{c2}(t) = b_{c2,\mathrm{p\ antinodal}}(t)$ [13, 14]] to 90° [at which $b_{c2}(t) = b_{c2,\mathrm{planar\ nodal}}(t)$ [14]] from top to bottom in increments of 10° [14]. $b_{c2}(\theta, t)$ decreases monotonically with increasing θ, but is less sensitive to θ for $\theta \sim 0^\circ$ and especially for $\theta \sim 90^\circ$ than for ordinary FS anisotropy. As θ increases from 0° to 90°, $-db_{c2}(\theta, t)/dt|_{t=1}$ decreases monotonically by an overall factor of $1/\sqrt{3}$. Since this slope variation is indistinguishable from that which could arise from FS anisotropy, the same curves are rescaled by $-db_{c2}/dt|_{t=1}$ in Fig. 4.1(b). Order parameter anisotropy effects are easiest to identify for $t \ll 1$. [14, 15].

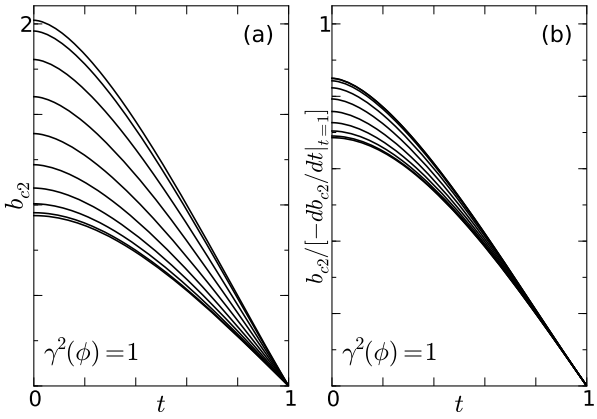

Figure 4.1: Plots of the dimensionless $b_{c2}(\theta, t) = 2eB_{c2}v_F^2/(2\pi T_c)^2$ for the polar/CBS p-wave state on a spherical Fermi surface with θ increasing from 0° [top, antinodal direction, with $b_{c2,\mathrm{p\ antinodal}}(t)$] to 90° [bottom, planar nodal direction, with $b_{c2,\mathrm{planar\ nodal}}(t)$] in increments of 10°. See text. (b) The same curves in Fig. 4.1(a) normalized by $-db_{c2}/dt|_{t=1}$.

At fixed t, $b_{c2}(\theta,\phi,t)$ for a polar/CBS p-wave superconductor with an ellipsoidal FS only depends upon $\alpha(\theta,\phi)$ and $\sin^2\theta'$, $b_{c2}(\pi-\theta,\phi,t)=b_{c2}(\theta,\phi,t)$, $\gamma^2(\phi)$ defined by Eq. (3.11) contains the entire ϕ dependence of b_{c2} [33, 44], and $-db_{c2}(\theta,\phi,t)/dt\big|_{t=1}\propto[3\sin^2\theta/\gamma^2(\phi)+\cos^2\theta]^{-1/2}$ [14], suggesting $\gamma^2(\phi)=3$ signals a crossover from order parameter to FS anisotropy as $t\to 1^-$.

In Fig. 4.2, we plotted $b_{c2}(\theta,t)/b_{c2}(0,t)$ for a variety of fixed $\gamma^2(\phi)$ values at $t=0,\frac{1}{2}$. At lower t and as $\gamma^2(\phi)$ increases from 0.1 to 3, there is an increasing difference between $b_{c2}(\theta,t)$ and the effective anisotropic mass form,

$$b_{c2}^{\rm eff}(\theta) \;=\; \left[\cos^2\theta/b_{c2}^2(0^\circ)+\sin^2\theta/b_{c2}^2(90^\circ)\right]^{-1/2} \tag{4.20}$$

fitted at each t, which fits are indicated by the dashed curves. Anomalous peaks at $0^\circ<\theta^*<90^\circ$ for $\gamma^2(\phi)>3$ are indicated by the arrows. For $\gamma^2(\phi)=10$, $t=1/2$, $b_{c2}(\theta)$ only has a conventional maximum at $\theta=90^\circ$. The anomalous $b_{c2}(\theta)$ is due to competing order parameter and FS anisotropy effects.

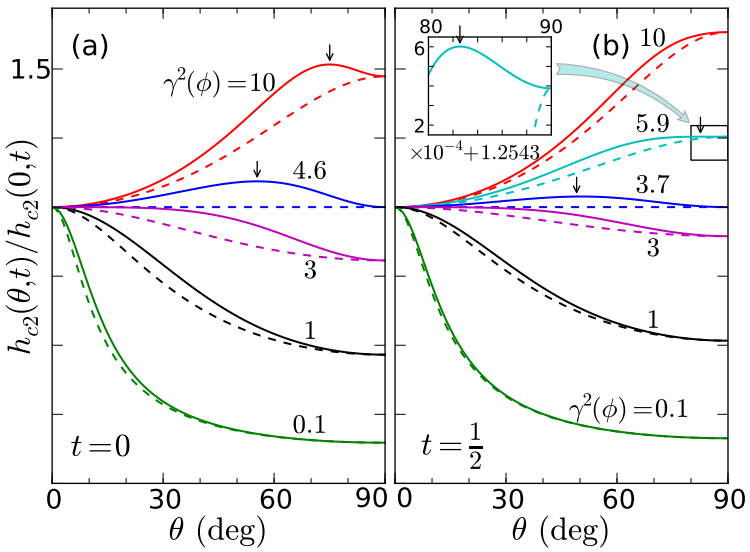

Figure 4.2: Calculated $b_{c2}(\theta,t)/b_{c2}(0,t)$ (solid) and fitted $b_{c2}^{\rm eff}(\theta,t)/b_{c2}(0,t)$, Eq. (5.28), (dashed) curves at constant $\gamma^2(\phi)$ values. The arrows indicate peak maxima at θ^* points. (a) $t = 0$ (b) $t = 1/2$. The inset is an enlargement of the $80° \leq \theta \leq 90°$ region of the $\gamma^2(\phi) = 5.9$ curve, with the indicated vertical scale points 1.2545 and 1.2549.

In Fig. 4.3, we plotted $\log_{10}[\gamma^2(\phi)]$ versus θ^*, the anomalous peak angle in $b_{c2}(\theta,t)$. Anomalous peaks appear for $\lambda(t) > \gamma^2(\phi) > 3$, where $\lambda(t)$ increases very rapidly with decreasing t for $t < 0.15$, as shown in inset (a). Inset (b) details the anomalous peak in $b_{c2}(\theta,0)$ for $\gamma^2(\phi) = 10^4$.

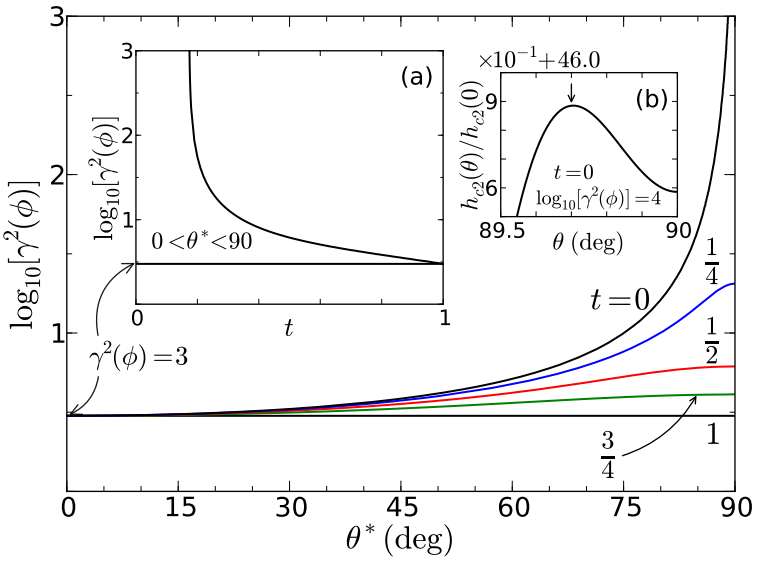

Figure 4.3: Logarithmic plot of $\gamma^2(\phi)$ as a function of θ^*, the peak angle in $b_{c2}(\theta, t)$, at the indicated t values. Inset (a): Plot of the $0° < \theta^* < 90°$ region versus $\log_{10}[\gamma^2(\phi)]$ and t. Inset (b): Plot of $b_{c2}(\theta, 0)/b_{c2}(0, 0)$ versus θ near to θ^* for $\gamma^2(\phi) = 10^4$. The vertical scale runs from 46.5 to 47.

Conventional peaks in $b_{c2}^{\rm eff}(\theta)$ occur only at either $\theta = 0°$ or $\theta = 90°$, but anomalous peaks only occur for $0° < \theta^* < 90°$. However, since $b_{c2}(\theta, \phi, t) = b_{c2}(180° - \theta, \phi, t)$, a second anomalous peak at $180° - \theta^*$ is reflection-symmetric in shape about $90°$ to that of the first one. When θ^* is close to $90°$, the magnitude of each anomalous peak is very small, but accurate measurements of this double peak could provide a definitive bulk test of the orbital symmetry of the order parameter.

URhGe

We extracted the FS effective masses from the RRR = 21 URhGe crystal data [6]. In Fig. 4.4(a) we present the calculated $b_{c2}(\theta, t)/b_{c2}(0, 0)$ in the ab plane (with $\boldsymbol{B} \perp \hat{\boldsymbol{c}}$) for different t values as

functions of θ. The dashed lines represent fits to the corresponding fitted curves using Eq. (4.20). Order parameter anisotropy effects in $b_{c2}(\theta)$ are significant for $t \ll 1$, but not for $t \sim 1$. Since the FS anisotropy is weaker in the ab plane than in the ac plane, our results differ substantially in this plane from those of Eq. (4.20). As noted above, in the bc plane ($\theta = \pi/2$), $b_{c2}(\phi) \propto \gamma(\phi)$, since their $b_{c2,b}(t)$ and $b_{c2,c}(t)$ data both fit the planar nodal polar/CBS state $b_{c2,\text{planar nodal}}(t)$ [6].

We also calculated $b_{c2}(\theta, \phi, t)$ for the RRR = 50 URhGe sample [7]. In Fig. 4.4(b), the calculated $b_{c2}(\theta, t)/b_{c2}(0, 0)$ and correspondingly fitted curves are plotted in the ab plane as a function of θ for various t, including $t = 0.16$, the lowest measurement value [7]. As in Fig. 4.2, the dashed curves are corresponding fits to Eq. (4.20).

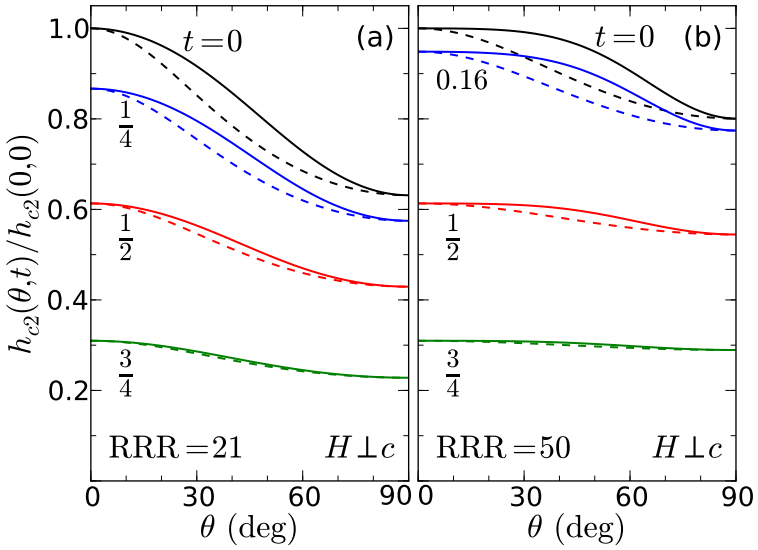

Figure 4.4: Calculated $b_{c2}(\theta, t)/b_{c2}(0, 0)$ (solid) and fitted $b_{c2}^{\text{eff}}(\theta, t)/b_{c2}(0, 0)$, Eq. (5.28), (dashed) curves, for $\boldsymbol{B} \perp \hat{\boldsymbol{c}}$ at various t values for the Fermi surface effective mass values obtained from experiment. (a) URhGe sample with RRR = 21 [6]. (b) URhGe sample with RRR = 50 [7].

Further complications of URhGe

The disappearing Shubnikov de Haas (SdH) oscillations with increasing $\boldsymbol{B}$ in URhGe were claimed to be due to a topological Lifshitz FS transition and a vanishing $\boldsymbol{v}_F(\boldsymbol{B})$ [8, 9], whereas the same effect in UCoGe was claimed to be due to changes in the effective mass $m(\boldsymbol{B})$ [11]. Anomalously anisotropic magnetization $\boldsymbol{M}(\boldsymbol{H})$ measurements of the T derivative $\gamma(\boldsymbol{H})$ of the specific heat in URhGe were claimed to support the latter interpretation [12]. From the SdH measurements [8], a strong $\boldsymbol{H}||\hat{\boldsymbol{b}}$ was also claimed to increase the pairing interaction strength V_0 and decrease the effective $\boldsymbol{v}_F(\boldsymbol{B})$ [8] of the heavy-electron ellipsoidal FS responsible for the pairing [17, 18, 19]. We note that it could also be interpreted in terms of changes in $\{m_i(\boldsymbol{B})\}$, and that b_{c2} and h_{c2} differ greatly for these field strengths due to the large $\boldsymbol{M}_0||\hat{\boldsymbol{c}}$ [9]. More importantly, if the order parameter in the reentrant phase maintains the polar/CBS form [16], dramatic further increases in V_0 and potentially in $\gamma^2(\phi)$ would be expected as the metamagnetic transition is approached [8], and the angle between $\boldsymbol{B}$ and $\boldsymbol{H}$ would decrease dramatically [9], yielding an anomalous peak in $b_{c2}(\theta, t)$ as shown in Fig. 4.2. Further experiments on URhGe to measure $\boldsymbol{M}(\boldsymbol{H})$ at $T_c(\boldsymbol{H})$ are necessary to compare with the calculated $B_{c2}(\theta, \phi)$. Allowing $V_0 \rightarrow V_0(\boldsymbol{B})$ might help to fit the reentrant phase. We have calculated $\gamma(\boldsymbol{B})$ self-consistently for an ellipsoidal FS in the presence of $\boldsymbol{M}_0$. These results make the analysis more complicated, but interesting. The results of this calculation will be presented in the next chapter, along with modifications to the present fits to the URhGe B_{c2} data [45].

Is strontium ruthenate p-wave?

If Sr_2RuO_4 were either a chiral (or non-chiral, depending upon the direction of $\boldsymbol{H}$) SK or a chiral ABM $p_x \pm ip_y$ parallel-spin state locked onto the layers as widely purported [49], for $\boldsymbol{H}$ parallel

to the layers $H_{c2,||}(T)$ would be proportional to either the rather linear $H_{c2,\mathrm{p\ antinodal}}(T)$ or the less linear $H_{c2,\mathrm{ABM\ antinodal}}(T)$ [72, 13], respectively. The former is shown as the top curve of Fig. 5.2(a), which differs very substantially from the experimental curves [60, 61, 27], and the latter also deviates substantially [72], although not as much, from the Sr_2RuO_4 parallel $H_{c2}(T)$ data that bend strongly downwards with decreasing T, precisely as expected for ordinary Pauli limiting [33, 61, 65], and entirely consistent with scanning tunneling microscopy results [73]. This is in striking contrast to $B_{c2}(T)$ measurements on URhGe and UCoGe, which violate the Pauli limit by factors of 20 or more [7, 5, 12], presenting very strong evidence for parallel-spin states. Fits of $H_{c2}(\theta, T)$ to different candidate Sr_2RuO_4 order parameter forms and reanalyses of the Knight shift measurements are sorely needed [49, 51]. Fits to the data of Kittika $et\ al.$ will be presented in a later chapter.

Future calculations on $CeCu_2Si_2$ using our technique

A variational approximation to our procedure was employed to fit the similarly extremely Pauli-limited in-plane $H_{c2}(90^\circ, \phi, t \ll 1)$ of $CeCu_2Si_2$, in which a d_{xy} order parameter was surprisingly claimed to best explain the weak ($\approx 0.5\%$) azimuthal anisotropy observed [36]. However, that very weak azimuthal anisotropy observed in this extremely Pauli-limited situation could also be explained by a 0.5% anisotropy in the g-tensor. Further measurements and a more accurate calculation of $H_{c2}(\theta, \phi, t)$ at intermediate θ values, where it is not dominated by Pauli-limiting effects, could provide a more definitive test of the order parameter symmetry.

UPt_3 f-wave?

Detailed $H_{c2}(\theta, \phi, t)$ for the proposed f-wave forms for the C phase of UPt_3 could provide supporting information for that scenario [25]. Including the intrinsic effective mass anisotropy from an ellipsoidal FS of the appropriate symmetry could aid in the correct identification of the order parameter symmetry in those and many other cases. In all three of these cases, inclusion of the KC-transformed Zeeman terms with an antiparallel-spin triplet or singlet spin state would first need to be made.

Discussion

From analytic expressions for parallel-spin, p-wave superconductors with completely broken symmetry, we calculated $B_{c2}(\theta, \phi, t)$ with general ellipsoidal Fermi surface anisotropy. For fixed $m_3/(m_1 \cos^2\phi + m_2 \sin^2\phi) > 3$, the competing effects of order parameter and Fermi surface anisotropy lead to an anomalous double peak in $B_{c2}(\theta)$ that can provide a definitive test of order parameter symmetry in URhGe and related compounds. Our method is generalizable to any order parameter symmetry, provided that the Zeeman terms are properly transformed for anti-parallel spin pairing. It is straightforward to generalize these calculations to include pairing on two spin-orbit or ferromagnetically split bands.

CHAPTER 5: ANGULAR DEPENDENCE OF THE UPPER CRITICAL FIELD OF THE SK/ABM P-WAVE STATE

Background

Although convincing experimental evidence suggests that URhGe exhibits a polar/CBS p-wave state such as

$$\Delta(\boldsymbol{k}) = \Delta_0 \hat{k}_z, \tag{5.1}$$

which was presented in the previous chapter, studies suggest that its sister compound UCoGe exhibits an axial state such as the Anderson-Brinkman-Morel (ABM) state with

$$\Delta(\boldsymbol{k}) = \Delta_0 (\hat{k_x} \pm i\hat{k}_y) \tag{5.2}$$

or the chiral Scharnberg-Klemm (SK) p-wave state with

$$\Delta_{\mathrm{SK}}(\hat{\boldsymbol{k}}) = \sum_{\sigma=\pm} \Delta_{0,\sigma}(\hat{k}_x + i\sigma\hat{k}_y). \tag{5.3}$$

Recently, much attention has been drawn to the compound Sr_2RuO_4 as being the quintessential

p-wave superconductor exhibiting an axial chiral p-wave state, since Knight shift measurements for $\boldsymbol{H}$ parallel and perpendicular to the layers showed no temperature T dependence below T_c, strongly suggestive of parallel spin pairing. In strong contrast to the Knight shift measurements performed on Sr_2RuO_4, $H_{c2}(T)$ measurements were strongly Pauli limited for $\boldsymbol{H} \parallel$ to the layers, and scanning tunneling microscopy measurements showed strong evidence for a nodeless gap, although with strontium ruthenate's cylindrical barrel shaped Fermi surfaces this might be consistent with a p-wave state.

The angular dependence of $H_{c2}(T, \theta, \phi)$ for the polar/CBS p-wave state as it relates to URhGe was presented in the previous chapter, and presented a rather novel way of identifying the polar/CBS order parameter symmetry in experimental studies. To help resolve the highly contradictory experiments on Sr_2RuO_4, we analytically calculate the angular dependence of $H_{c2}(T, \theta, \phi)$ for the Anderson-Brinkman-Morel (ABM) state and the chiral Scharnberg-Klemm (SK), which will help experimentalists in finding key signatures of these order parameter symmetries in UCoGe, Sr_2RuO_4 and other candidate materials using as presented in the previous chapter and Appendix A.

The model

Since UCoGe is orthorhombic as in the case of URhGe, we calculate the upper critical field using a general ellipsoidal Fermi surface. For tetragonal Sr_2RuO_4, which has three barrel shaped Fermi surfaces, we consider only one in our calculations since we are primarily interested in $H_{c2}(T, 90^\circ)$, which is dominated only by one Fermi surface. A coupling interaction of the form

$$V(\hat{\boldsymbol{k}}, \hat{\boldsymbol{k}'}) = 3V_0(\hat{k_1}\hat{k_1'} + \hat{k_2}\hat{k_2'}), \tag{5.4}$$

which can be written as

$$V(\hat{\boldsymbol{k}}, \hat{\boldsymbol{k}}') = \frac{3}{2} V_0 \sum_{\sigma=\pm} (\hat{k_1} + i\sigma \hat{k_2})(\hat{k_1'} - i\sigma \hat{k_2'}), \tag{5.5}$$

and is expected to have a $B_{c2}(T, \theta, \phi)$ given by the chiral SK state. Although the purported state for Sr_2RuO_4 is $\hat{\boldsymbol{z}}(\hat{k_x} + i\hat{k_y})$, where $\hat{\boldsymbol{z}}$ corresponds to an antiparallel-spin state in the lattice representation, we will assume parallel spin pairing, a magnetic induction $\boldsymbol{B} = B(\sin\theta\cos\phi, \sin\theta\sin\phi, \cos\theta)$ and a general ellipsoidal Fermi surface with single particle effective masses m_1, m_2, and m_3 to calculate the full angular and temperature dependencies of the ABM and SK states.

As for the polar/CBS state presented earlier, we assume weak coupling for a clean homogeneous type-II parallel-spin $\uparrow$ p-wave superconductor with effective Hamiltonian [13, 14],

$$\begin{aligned} \mathcal{H} &= \sum_{\boldsymbol{k},\sigma} a^\dagger_{\boldsymbol{k},\sigma} [\epsilon(\boldsymbol{k} - e\boldsymbol{A}) - \mu_\sigma(B)] a_{\boldsymbol{k},\sigma} \\ &\quad + \frac{1}{2} \sum_{\boldsymbol{k},\boldsymbol{k}'} a^\dagger_{\boldsymbol{k}',\sigma} a^\dagger_{\boldsymbol{k},\sigma} V(\hat{\boldsymbol{k}}, \hat{\boldsymbol{k}}') a_{\boldsymbol{k},\sigma} a_{\boldsymbol{k}',\sigma}, \end{aligned} \tag{5.6}$$

where the interaction has the form

$$V(\hat{\boldsymbol{k}}, \hat{\boldsymbol{k}}') = \frac{3}{2} V_0 \sum_{\sigma'=\pm} f_{\sigma'}(\hat{\boldsymbol{k}}) \hat{\boldsymbol{d}}_{\boldsymbol{\sigma'}} \cdot \hat{\boldsymbol{d}}^*_{\boldsymbol{\sigma'}} f^*_{\sigma'}(\hat{\boldsymbol{k}}'), \tag{5.7}$$

where e is the electronic charge,

$$\hat{\boldsymbol{d}}_{\sigma'} = \hat{\boldsymbol{x}} + i\sigma'\hat{\boldsymbol{y}} \tag{5.8}$$

μ is the chemical potential, the unit wave vectors are defined on the ellipsoidal each FS are

$$\hat{k}_i \equiv \frac{\sqrt{2m_i}}{\alpha(\theta,\phi)} \frac{\partial}{\partial k_i} \sqrt{\epsilon(\boldsymbol{k})}\big|_{\epsilon(\boldsymbol{k})=\mu_\uparrow(B)}, \tag{5.9}$$

where

$$\alpha(\theta,\phi) \;\; = \;\; [\overline{m}_1 \sin^2\theta\cos^2\phi + \overline{m}_2 \sin^2\theta\sin^2\phi + \overline{m}_3\cos^2\theta]^{1/2}, \tag{5.10}$$

$\overline{m}_i = m_i/m$, $m = (m_1 m_2 m_3)^{1/3}$, and we set $\hbar = k_B = 1$.

Unlike URhGe, Sr_2RuO_4 lacks any long range ferromagnetic order, and thus its upper critical induction, $B_{c2} = \mu_0 H_{c2}$, where H_{c2} is the upper critical field.

Performing identical Klemm-Clem transformations as in the case of the polar/CBS state, mapping the general ellipsoidal Fermi surface onto a spherical one, and rotating the resulting induction, $\boldsymbol{B'}$ to a new $\hat{z'}$ axis direction, we obtain the linearized and transformed gap equation

$$\overline{\tilde{\Delta}}(\tilde{\boldsymbol{R}},\hat{\tilde{\boldsymbol{k}}}) \;\; = \;\; T\sum_{\omega_n} \frac{N(0)}{2} \int d\Omega_{\tilde{\boldsymbol{k}}'} \tilde{V}(\hat{\tilde{\boldsymbol{k}}},\,\hat{\tilde{\boldsymbol{k}}}') \int_0^\infty d\xi_{\tilde{\boldsymbol{k}}'} e^{-2\xi_{\tilde{\boldsymbol{k}}'}|\omega_n|} e^{-i\xi_{\tilde{\boldsymbol{k}}'} v_F \hat{\tilde{\boldsymbol{k}}}'\cdot\tilde{\boldsymbol{\Pi}}(\tilde{\boldsymbol{R}})} \overline{\tilde{\Delta}}(\tilde{\boldsymbol{R}},\,\hat{\tilde{\boldsymbol{k}}}'), \tag{5.11}$$

where $\overline{\tilde{\Delta}}$ is the transformed Δ amplitude without the gauge phases, $N(0) = mk_F/(2\pi^2)$ is the density of states per spin at the chemical potential $\mu_\uparrow(\tilde{B}_3)$ for an effectively isotropic metal with a geometric mean mass m, effective Fermi wave vector $k_F = \sqrt{2m\mu_\uparrow(\tilde{B}_3)}$, effective Fermi velocity $v_F = k_F/m$, and

$$\tilde{\mathbf{\Pi}}(\tilde{\boldsymbol{R}}) \;\; = \;\; -i\alpha\tilde{\boldsymbol{\nabla}}_{\tilde{\boldsymbol{R}}} + 2e\tilde{\boldsymbol{A}}(\tilde{\boldsymbol{R}}), \tag{5.12}$$

where $\alpha(\theta,\phi)$ is given by Eq. (5.10). We also define the anisotropy function

$$\gamma^2(\phi) \;\; = \;\; \frac{m_3}{m_1\cos^2\phi + m_2\sin^2\phi}, \tag{5.13}$$

so that $\alpha = \sqrt{\overline{m_3}}\sqrt{\cos^2\theta + \gamma^{-2}(\phi)\sin^2\theta}$. The KC transformations also modify the effective pairing interaction to become

$$\tilde{V}(\hat{\tilde{\boldsymbol{k}}},\,\hat{\tilde{\boldsymbol{k}}}') = \frac{3}{2}V_0\sum_{\sigma'=\pm}\tilde{f}_{\sigma'}(\hat{\tilde{\boldsymbol{k}}})\tilde{f}^*_{\sigma'}(\hat{\tilde{\boldsymbol{k}}}') \tag{5.14}$$

where

$$\tilde{f}_\sigma(\hat{\tilde{\boldsymbol{k}}}) = \tilde{\hat{k}}_1 + i\sigma(\tilde{\hat{k}}_2\cos\theta' + \tilde{\hat{k}}_3\sin\theta') \tag{5.15}$$

and $\cos\theta' = \sqrt{\overline{m_3}}\cos\theta/\alpha$, $etc.$ From the form of

$$\tilde{V}(\hat{\tilde{\boldsymbol{k}}},\,\hat{\tilde{\boldsymbol{k}}}') = \frac{3}{2}V_0\sum_{\sigma'=\pm}\tilde{f}_{\sigma'}(\hat{\tilde{\boldsymbol{k}}})\tilde{f}^*_{\sigma'}(\hat{\tilde{\boldsymbol{k}}}') \tag{5.16}$$

we obtain

$$\Delta(\tilde{\boldsymbol{R}}, \hat{\tilde{\boldsymbol{k}}}) = \sum_{\sigma=\pm} \overline{\tilde{\Delta}}_\sigma(\tilde{\boldsymbol{R}}) \tilde{f}_\sigma(\hat{\tilde{\boldsymbol{k}}}). \tag{5.17}$$

Since the Cooper pairs orbit in Landau orbits perpendicular to the applied magnetic field $\boldsymbol{H}$, the natural basis to use is the set of eigenstates of the simple harmonic oscillator. We thus have

$$\overline{\tilde{\Delta}}_\sigma(\tilde{\boldsymbol{R}}) = \sum_{n=0}^{\infty} a_n^\sigma |n(\tilde{\boldsymbol{R}}) > . \tag{5.18}$$

Performing the integrals over $\hat{\tilde{k}}_i'$ in the linearized gap equation, we obtain the double recursion relation

$$\begin{aligned} a_n^\pm &= (\frac{1}{2}(1+\cos^2\theta')a_n^{(\pm)} + \frac{1}{2}\sin^2\theta' a_n^{(\mp)})\alpha_n^{(a)} \\ &\quad + \frac{1}{2}\sin^2\theta'(a_n^{(\pm)} - a_n^{(\mp)})\alpha_n^{(p)} \\ &\quad + (\frac{1}{4}\sin^2\theta' a_{n+2}^{(\pm)} + \frac{1}{4}(1\pm\cos\theta')^2 a_{n+2}^{(\mp)})\beta_n \\ &\quad + (\frac{1}{4}\sin^2\theta' a_{n-2}^{(\pm)} + \frac{1}{4}(1\mp\cos\theta')^2 a_{n-2}^{(\mp)})\beta_{n-2}, \end{aligned} \tag{5.19}$$

where

$$\alpha_n^{(p,a)} = \pi T \sum_{\omega_n} \int_0^{\pi} d\theta_{\tilde{\boldsymbol{k}}'} \sin\theta_{\tilde{\boldsymbol{k}}'} \left(3\cos^2\theta_{\tilde{\boldsymbol{k}}'}, \frac{3}{2}\sin^2\theta_{\tilde{\boldsymbol{k}}'} \right) \times \int_0^{\infty} d\xi_{\tilde{\boldsymbol{k}}'} e^{-2\xi_{\tilde{\boldsymbol{k}}'}|\omega_n|} e^{-\eta_{\tilde{\boldsymbol{k}}'}/2} L_n(\eta_{\tilde{\boldsymbol{k}}'}), \quad (5.20)$$

$$\beta_n = \pi T \sum_{\omega_n} \int_0^{\pi} d\theta_{\tilde{\boldsymbol{k}}'} \frac{3}{2}\sin^3\theta_{\tilde{\boldsymbol{k}}'} \int_0^{\infty} d\xi_{\tilde{\boldsymbol{k}}'} e^{-2\xi_{\tilde{\boldsymbol{k}}'}|\omega_n|} \times e^{-\eta_{\tilde{\boldsymbol{k}}'}/2}(-\eta_{\tilde{\boldsymbol{k}}'}) L_n^{(2)}(\eta_{\tilde{\boldsymbol{k}}'})[(n+1)(n+2)]^{-1/2}, \quad (5.21)$$

where

$$\eta_{\tilde{\boldsymbol{k}}'} = eB\alpha(\theta,\phi) v_F^2 \xi_{\tilde{\boldsymbol{k}}'}^2 \sin^2\theta_{\tilde{\boldsymbol{k}}'}, \quad (5.22)$$

$t = T/T_c$, $T_c = (2e^C\omega_0/\pi)\exp(-1/N(0)V_0)$, ω_0 is a characteristic pairing cutoff frequency, $C \approx 0.5772$ is Euler's constant, and $L_n(z)$ and $L_n^{(2)}(z)$ are a Laguerre and an associated Laguerre polynomial, respectively.

In the case of the chiral ABM state, the $a_n^{(+)}$ and $a_n^{(-)}$ amplitudes are decoupled, so the recursion relation decouples and can be written as

$$a_n^{(\pm)} D_n = \Gamma_n a_{n+2}^{(\pm)} + \Gamma_{n-2} a_{n-2}^{(\pm)}, \quad (5.23)$$

where

$$D_n = 1 - \frac{1}{2}(1+\cos^2\theta')\alpha_n^{(a)} - \frac{1}{2}\sin^2\theta'\alpha_n^{(p)}, \quad (5.24)$$

and

$$\Gamma_n = \frac{1}{4}\sin^2\theta'\beta_n. \tag{5.25}$$

Upon solving the recursion relation, we obtain the continued fraction expression from which $B_{c2}(\theta,\phi,t)$ for the chiral ABM is obtained numerically,

$$D_0 - \frac{\Gamma_0^2}{D_2 - \frac{\Gamma_2^2}{D_4 - \cdots}} \tag{5.26}$$

The reduced $b_{c2}(\theta,t)$ for parallel-spin superconductors in the p-wave chiral ABM state with a dominant spherical Fermi surface ($\gamma^2(\phi)=1$) are shown in Fig. 5.1. In Fig 5.1(a), $b_{c2}(t)$ curves are shown for various angles varying from $\theta = 0^\circ$ ($\boldsymbol{b} \parallel \hat{\boldsymbol{c}}$) to $\theta = 90^\circ$ ($\boldsymbol{b} \perp \hat{\boldsymbol{c}}$) in increments of 10°. The slope of $b_{c2}(\theta,\phi,t)$ just below $t=1$ ($T=T_c$) is given by

$$b_{c2}(\theta,\phi.t) \propto [m_3\cos^2\theta + 2\gamma^{-2}(\phi)\sin^2\theta]^{-1/2}. \tag{5.27}$$

This form varies from the conventional anisotropic mass formula by the factor of 2, which arises from the chiral ABM order parameter anisotropy. Since order parameter anisotropy is indistinguishable from effective mass anisotropy, we have plotted in Fig 5.1(b) $b_{c2}(\theta,t)$ normalized by the slope at $t=1$ in order to distinguish which part of the anisotropy is due to order parameter anisotropy. As expected, order parameter anisotropy is non existent at the transition temperature,

and becomes more prominent at lower temperatures approaching $T = 0$ K. From these curves, we see that for a spherical Fermi surface and a chiral ABM p-wave symmetry, $b_{c2}(\theta, t)$ is a monotonic function of θ, decreasing with increasing θ, as in the case for the polar/CBS state.

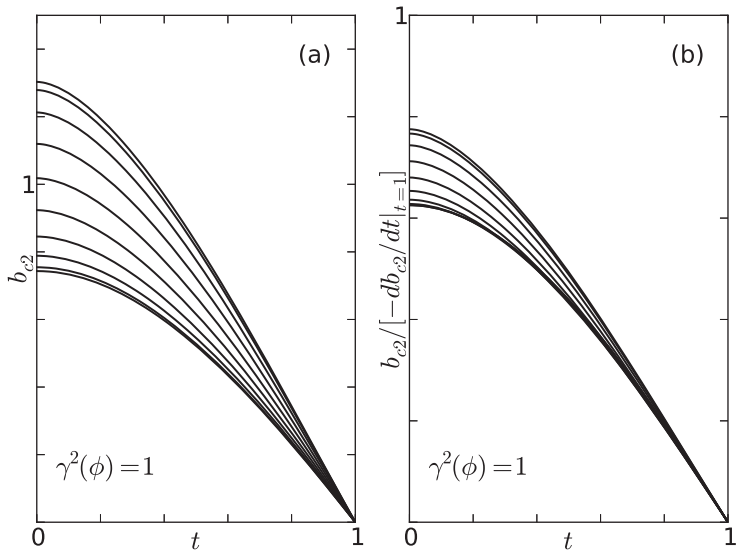

Figure 5.1: (a) Reduced b_{c2} versus $t = T/T_c$ for the chiral ABM state for various angles between $\theta = 0°(\boldsymbol{H} \parallel \hat{\boldsymbol{c}}$, top) and $\theta = 90°(\boldsymbol{H} \perp \hat{\boldsymbol{c}}$, bottom) in $10°$ increments for a spherical Fermi surface ($\gamma^2(\phi) = 1$).(b) Same curves normalized by the slope of each curve at $t = 1$ ($T = T_c$)

Things become more interesting when the effects of a general ellipsoidal Fermi surface are included. Figure 5.2 shows $b_{c2}(\theta)$ anisotropy normalized by $b_{c2}(0, t)$ for various $\gamma^2(\phi)$, ranging from $0.1 - 1.5$, and reduced temperature $t = 0, 1/2$ values. As expected, the anisotropy is more pronounced for $t = 0$, and $\gamma^2(\phi) > 1$ values. For $\gamma^2(\phi) > 1/2$, we note that the anisotropy is monotonic and varies only slightly from the Ginzburg Landau anisotropic mass formula (dashed curves)

$$b_{c2}^{\rm eff}(\theta) \;=\; \left[\cos^2\theta/b_{c2}^2(0^\circ) + \sin^2\theta/b_{c2}^2(90^\circ)\right]^{-1/2}. \tag{5.28}$$

This is attributed to the fact that for $\gamma^2(\phi) > 1/2$, effective mass anisotropy dominates the b_{c2} anisotropy, so that there is no competition between effective mass anisotropy and order parameter anisotropy. However, for $\gamma^2 < 1/2$ we observe an anomalous peak at θ^*, and by reflection symmetry at $\theta = 180^\circ - \theta^*$, that is distinctly different than the conventional b_{c2} maxima at 0° and 90°.

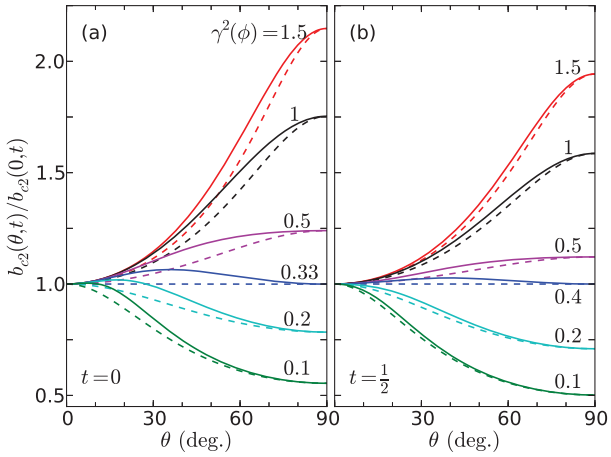

Figure 5.2: Reduced b_{c2} versus θ normalized by $b_{c2}(0,t)$ for the chiral ABM state at various $\gamma^2(\phi)$ values (solid) and temperatures $t = T/T_c = 0$ (a) and $t = 1/2$ (b). The dashed curves represent a fit using the Ginzburg-Landau anisotropic effective mass formula, which deviates from the calculated anisotropy due to order parameter effects. We observe an anomalous peak at $\theta^* < 90^\circ$ for $\gamma^2(\phi) < 1/2$ signaling a competition between order parameter anisotropy and effective mass anisotropy.

These anomalous peaks arise from a competition between order parameter anisotropy which tends

to enhance $b_{c2}(\theta, t)$ with increasing θ, and effective mass anisotropy which tends to suppress $b_{c2}(\theta, t)$ with increasing $\gamma^{-2}(\phi)$. These anomalous peaks were also observed for the polar/CBS state as demonstrated in chapter 4. However, this anomalous peak is unlikely to be observed in UCoGe and Sr_2RuO_4 for which $\gamma^2(\phi) >> 1$, but it may be relevant for yet undiscovered materials exhibiting the p-wave chiral ABM order parameter symmetry.

The much more interesting chiral p-wave state is the Scharnberg-Klemm state, for which the order parameter may be written as in Eq 1.20. The SK state is chiral provided that the pairing amplitudes for both axial modes are distinct $\Delta_{0,+} \neq \Delta_{0,-}$. This implies that $a_n^{(+)} \neq a_n^{(-)}$ in Eq. 5.19 for at least one relevant n value. One can easily show from Eq. 5.19 by setting $\theta' = 0^\circ$ that the recursion relation is greatly simplified for $a_n^{(-)} = -a_n^{(+)} \neq 0$ to become

$$[1 - \alpha_n^{(a)}][1 - \alpha_{n+2}^{(a)}] = \beta_n^2, \tag{5.29}$$

which is the expression for $b_{c2}(t)$ for the SK state with $\boldsymbol{h}$ in the nodal direction. Substituting $\theta' = 90^\circ$ into Eq 5.19, we obtain for $a_n^{(+)} \neq 0$

$$\alpha_n^{(p)} = 1, \tag{5.30}$$

which is the expression for $b_{c2}(t)$ for $\boldsymbol{h}$ in the antinodal (polar state) direction. However, for $\boldsymbol{h}$ applied in some general direction between $\theta = 0^\circ$ and $\theta = 90^\circ$, and for $a_n^{(+)} \neq a_n^{(-)}$, Eq. 5.19 is a coupled double recursion relation in the six harmonic oscillator amplitudes $a_n^{(\pm)}$, $a_{n+2}^{(\pm)}$, and $a_{n-2}^{(\pm)}$. First we cleverly redefine the variables,

$$\Psi_n^{(\pm)} = \frac{1}{2}(a_n^{(+)} \pm a_n^{(-)}), \tag{5.31}$$

$$D_n^{(+)} = 1 - \alpha_n^{(a)}, \tag{5.32}$$

$$D_n^{(-)} = 1 - \alpha_n^{(a)} \cos^2\theta' - \alpha_n^{(p)} \sin^2\theta', \tag{5.33}$$

and construct

$$\phi_n^{(\pm)} = \cos\theta' D_n^{(+)} \Psi_n^{(+)} \pm D_n^{(-)} \Psi_n^{(-)}. \tag{5.34}$$

After letting $n \to n+2$ in the expression for $\phi^{(-)}$, we obtain two equations for $\Psi_n^{(+)}$ and $\Psi_{n+2}^{(+)}$ in terms of $\Psi_n^{(-)}$ and $\Psi_{n+2}^{(-)}$. One then algebraically eliminates $\Psi_n^{(+)}$ and $\Psi_{n+2}^{(+)}$ in favor of $\Psi_n^{(-)}$ and $\Psi_{n+2}^{(-)}$. One then lets $n \to n-2$ in the expression for $\Psi_{n+2}^{(-)}$ and equates the resulting expression with the first expression for $\Psi_n^{(-)}$, resulting in the simple recursion relation

$$A_n \Psi_{n+2}^{(-)} + B_n \Psi_n^{(-)} + C_{n-2} \Psi_{n-2}^{(-)} = 0, \tag{5.35}$$

which results in a continued fraction expression for b_{c2},

$$B_0 - \frac{A_0 C_0}{B_2 - \frac{A_2 C_2}{B_4 - \cdots}} = 0, \tag{5.36}$$

where $B_n = B_n^{(+)} - B_n^{(-)}$,

$$A_n = E_{n-2}\beta_n[\cos^2\theta' D_{n+2}^{(+)}] - D_{n+2}^{(-)}], \tag{5.37}$$

$$B_n^{(+)} = D_n^{(-)}[E_n D_{n-2}^{(+)} + E_{n-2} D_{n+2}^{(+)}], \tag{5.38}$$

$$B_n^{(-)} = \cos^2\theta'[\beta_n^2 E_{n-2} + E_n \beta_{n-2}^2], \tag{5.39}$$

$$C_n = \beta_{n-2} E_n[\beta_{n-2}\cos^2\theta' D_{n-2}^{(+)} - D_{n-2}^{(-)}], \tag{5.40}$$

and

$$E_n = D_n^{(+)} D_{n+2}^{(+)} - \beta_n^2. \tag{5.41}$$

We also eliminated $\Psi_n^{(-)}$ and $\Psi_{n+2}^{(-)}$ in favor of $\Psi_n^{(+)}$ and $\Psi_{n+2}^{(+)}$. However, the resulting continued fraction expression used to obtain b_{c2} revealed a slightly lower value for the critical field; we chose the first solution which resulted in the higher $b_{c2}(\theta, \phi, t)$ value for all temperatures and angles. Figure 5.3(a) shows the reduced upper critical field $b_{c2}(t)$ for the the external magnetic field in the nodal ($\boldsymbol{H} \parallel \hat{\boldsymbol{c}}$), and the antinodal ($\boldsymbol{H} \perp \hat{\boldsymbol{c}}$) directions of the chiral ABM state, chiral SK state, polar/CBS state, and s-wave state without Pauli limiting for a spherical Fermi surface ($\gamma^2(\phi) = 1$). The upper critical field for $\boldsymbol{H} \parallel$ to the antinodal direction is given by curve (1) in the figure, which corresponds to b_{c2} for an isotropic BW state along all field directions, and is the highest b_{c2} of all the p-wave states and directions. The upper critical field for the SK state with $\boldsymbol{H} \parallel$ nodal direction is given by curve (2) and is the second highest $b_{c2}(t)$. Curve (3) is the upper critical field of the chiral ABM state with the field in the antinodal direction, which was previously unpublished. For an s-wave superconductor without Pauli limiting effects, one has an upper critical field given by curve (4). For the CBS/polar state and ABM states with $\boldsymbol{H} \parallel$ to the nodal direction, one has an upper critical field given by curve (5) and (6) respectively.

It is important to note that the second chiral component in Δ_{SK} allows the superconductivity to survive at higher fields than for Δ_{ABM} Figure 5.3(b) shows the temperature t dependence of $b_{c2}(\theta, t)$ of the SK state for $\theta = 0^\circ$ ($\boldsymbol{H} \parallel \hat{\boldsymbol{c}}$)(bottom) to $\theta = 90^\circ$ ($\boldsymbol{H} \perp \hat{\boldsymbol{c}}$) in increments of 10°. Surprisingly, the b_{c2} curves for $\theta = 0^\circ, 10^\circ, 20^\circ$, and 40° are remarkably close to each other. This signals a chiral to non-chiral transition that occurs at $\theta^* = 40^\circ$. We interpret this as being the signature of the vortices locking on to the nodal direction for $\theta \leq 40^\circ$, unlock from that direction at $\theta = 40^\circ$, and lock onto the non-chiral antinodal direction for $\theta > 40^\circ$.

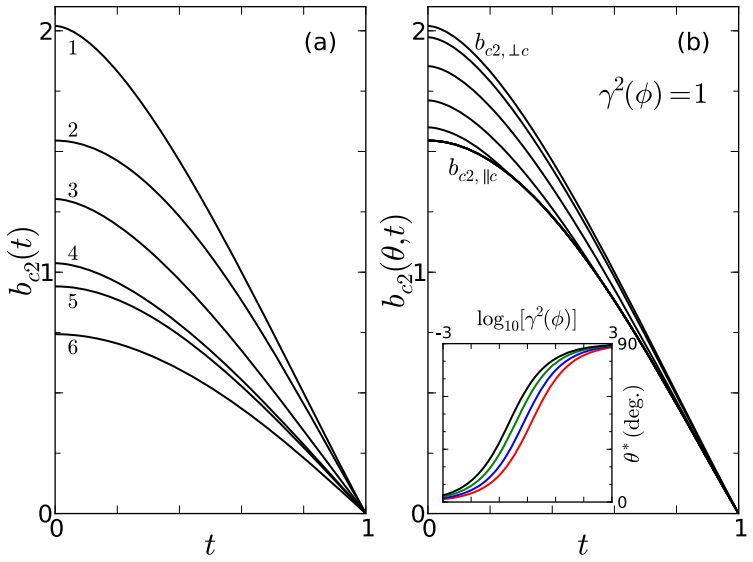

Figure 5.3: (a) Upper critical field curves for the antinodal field direction of the SK state (1), the nodal field direction of the SK state (2), the antinodal ABM state direction (3), the s-wave state with no Pauli limiting (4), the nodal direction of the CBS state (5), and the nodal directions of the ABM state, which has the lowest $b_{c2}(t)$. (b) Reduced $b_{c2}(t)$ curves for the chiral SK state for various angles ranging from $\theta = 0°$ to $\theta = 90°$ in increments of $10°$ for a spherical Fermi surface. Surprisingly, the curves for $\theta = 0°, 10°, 20°, 30°$, and $40°$ are indistinguishable at this scale, signaling a first order chiral to non-chiral transition that occurs at $\theta^* = 40°$. Inset: Plots of the kink transition angle θ^* versus $\log_{10}(\gamma^2(\phi))$ from top to bottom for $t = 3/4$ (black), $t = 1/2$ (green), $t = 1/4$ (blue), and $t = 0$ (red).

In order to more readily observe this phenomenon, we have plotted the normalized angular dependence in Fig 5.4 for various temperatures ($t = 0, 1/4, 1/2, 3/4$), and for various effective mass anisotropy values ($\gamma^2(\phi) = 0.1, 0.5, 1$ and 2). We note that there is a kink in the angular dependence at $\theta = \theta^*$ for fixed $\gamma(\phi)$ and t. In the inset of Fig 5.3(b) we have plotted this transition angle

θ^* as a function of $\log_{10}(\gamma^2(\phi))$. We note that as $\gamma^2(\phi)$ gets larger, the transition angle gets closer and closer to $\theta^* = 90°$. If Sr_2RuO_4 were a chiral p-wave superconductor, since its $\gamma^2(\phi) > 10^3$, the first order transition would occur for $\theta \approx 90°$, which might be difficult to detect. It is especially interesting to note that such a transition may have already been observed in Sr_2RuO_4 in very recent $H_{c2}(T)$ measurements. Since the upper critical field is strongly Pauli limited with the field parallel to the layers, more experiments are necessary to establish a chiral p-wave order parameter as the OP symmetry in Sr_2RuO_4.

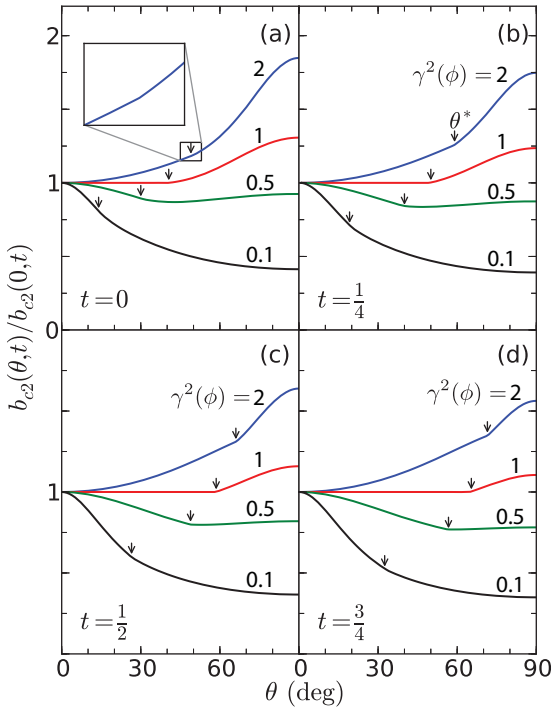

Figure 5.4: Reduced upper critical induction b_{c2} versus θ normalized by $b_{c2}(0,t)$ for the chiral SK state for $\gamma^2(\phi) = 2$ (blue, top), 1 (red), 0.5 (green), and 0.1 (black) at $t = 0$ (a), $t = 1/4$ (b), $t = 1/2$ (c), and $t = 3/4$ (d). The arrows indicate the location of the kink signaling the onset of the first order transition from a chiral (antinodal SK state, $\theta < \theta^*$) to a non-chiral SK state (nodal polar, $\theta > \theta^*$).

CHAPTER 6: SPECIFIC HEAT OF SUPERCONDUCTORS IN THE NORMAL STATE AND WITH TWO GENERAL ELLIPSOIDAL FERMI SURFACES

Background

In addition to the mysterious reentrant superconductivity observed in clean samples of URhGe, Shubnikov de Haas (SdH) measurements were also performed on even cleaner samples of URhGe with an RRR=130, from which Yelland *et al.* observed a sudden disappearance of SdH oscillations in the field-dependent resistance, $R(\boldsymbol{B})$ for $\mu_0 \boldsymbol{H} \geq 15.5$ T [8]. Those authors claimed the disappearance of the SdH oscillations was due to a topological Lifshitz Fermi surface(FS) transition, where the field-dependent cross-sectional area of the FS, $A(\boldsymbol{B})$, suddenly vanishes, quenching the SdH oscillations. They attributed this effect partially to a decrease in the effective cyclotron mass m^*, but primarily to a decrease in the field-dependent Fermi velocity, $\boldsymbol{v}_F(\boldsymbol{B}) = \hbar k_F/m^*$ with a smooth drop to zero at around 15 T in the wave vector $k_F(\boldsymbol{B})$. Yelland *et al.* also claimed that a strong $\boldsymbol{H}||\hat{\boldsymbol{b}}$ increases the pairing interaction strength V_0 and decreases the effective $\boldsymbol{v}_F(\boldsymbol{B})$ of the heavy-electron ellipsoidal FS responsible for the pairing [8, 17, 18, 19]. Yelland *et al.* further attributed the dramatic re-entrance into the superconducting state of URhGe at high magnetic fields in the b-direction as a direct consequence of this. However, a similar effect in UCoGe was claimed to be due to anomalies in the effective mass $m(\boldsymbol{B})$ [11]. Thermopower measurements at large fields provided strong evidence for a change in the FS in UCoGe [40], but no such change at the reentrant field in URhGe [12, 41]. As noted in the most recent review article on the subject, it is presently unclear as to whether the FS changes dramatically with $\boldsymbol{H}$, as in a vanishing of the average Fermi wavevector k_F, or whether the effective mass is strongly enhanced with $\boldsymbol{H}$ [42]. Anomalously anisotropic magnetization $\boldsymbol{M}(\boldsymbol{H})$ measurements of the T derivative $\gamma(\boldsymbol{H})$ of the specific heat in

URhGe and of the coefficient A in the low-T resistivity $\rho(T) = \rho_0 + AT^2$ in UCoGe were claimed to support the latter interpretation [11, 42], the latter using the Kadowaki-Woods relation [43]. But all of these works assumed a spherical FS, which for orthorhombic UCoGe and URhGe is certainly not the case [12]. Thus, if the enhancement of the "effective mass" with $\boldsymbol{H}$ actually occurs, one should try to determine which of the effective masses on which of the relevant FSs shows the strong enhancement. In the following, we show that strong changes with applied field occurring on only one of the three single particle effective masses on one of the ellipsoidal FSs in our double ellipsoidal FS model can explain the specific heat data on URhGe.

To help resolve this controversy, low-T $\boldsymbol{M}(\boldsymbol{H})$ measurements were conducted on URhGe yielding the slope $\gamma(\boldsymbol{H})$ with T of the specific heat for $\boldsymbol{H}||\hat{\boldsymbol{a}}, \hat{\boldsymbol{b}}, \hat{\boldsymbol{c}}$ from the Maxwell relation [11]. They found that $\gamma(\boldsymbol{H})$ remained relatively flat for $\boldsymbol{H}||\hat{\boldsymbol{a}}$ with a slight hint of upward curvature, decreased approximately linearly for $\boldsymbol{H}||\hat{\boldsymbol{c}}$ with slight upward curvature, but increased with $\boldsymbol{H}||\boldsymbol{b}$ for $H << H_R$, the "reentrant field", up to a sharp maximum at $\mu_0 \boldsymbol{H} \cdot \hat{\boldsymbol{b}} \sim \mu_0 H_R \sim 12$T, then decreased to a value higher than that at $\boldsymbol{H} = 0$.

To help resolve this issue, we analytically calculated $\gamma(\boldsymbol{B}) = \partial(S/V)/\partial T$ for an electron gas with two ferromagnetically split ellipsoidal Fermi surfaces, one for each spin projection, $\sigma = \{\uparrow, \downarrow\}$, with three distinct single particle effective masses, $\{m_{i\sigma}\}$, describing each FS. We study this double ellipsoidal FS model in the presence of an arbitrarily oriented magnetic induction, $\boldsymbol{B} = \mu_0 \boldsymbol{H} + \boldsymbol{M}$, and compare our results to the experimental curves of $\gamma(\boldsymbol{B})$ for all three crystallographic directions measured for URhGe.

The model

We begin our calculation with the Hamiltonian of the system

$$H = \sum_{\sigma=\uparrow,\downarrow} \epsilon_\sigma(\boldsymbol{k} - e\boldsymbol{A}) - \mu_\sigma(\boldsymbol{B}), \tag{6.1}$$

where

$$\mu_\sigma(\boldsymbol{B}) = \mu(0) + \sigma I/2 - g\mu_B \boldsymbol{\sigma} \cdot \boldsymbol{B}/2, \tag{6.2}$$

and

$$\epsilon_\sigma(\boldsymbol{k}) = \sum_{i=1}^{3} k_i^2/[2m_{i\sigma}(\boldsymbol{B})], \tag{6.3}$$

μ_B is the Bohr magneton, $g \sim 2$, $g\mu_B/2 = \gamma$ is the gyromagnetic ratio for the electron, $\sigma = \{\uparrow, \downarrow\}$, the $\mu_\sigma(\boldsymbol{B})$ are the chemical potentials at $T = 0$ in a magnetic induction,$\boldsymbol{B}$, on each FS, $\mu(0)$ is the non-magnetic chemical potential at $T = 0$ and $\boldsymbol{B} = 0$, $\boldsymbol{A}$ is the magnetic vector potential, e is the magnitude of the charge of an electron, I is the Stoner coupling energy, $\boldsymbol{B} = \boldsymbol{\nabla} \times \boldsymbol{A}$, the $m_{i\sigma}(\boldsymbol{B})$ are the induction dependent single particle effective masses on each FS, and we set $\hbar = 1$.

Here, we have included the effect of two distinct ellipsoidal Fermi surfaces, which are split by the ferromagnetism, one for each spin projection, by including three single particle effective masses for each spin projection, $m_{i\sigma}(\boldsymbol{B})$. Figure 6.1 depicts the two distinct FSs which are aligned along the three crystal axis directions, with the externally applied magnetic field, $\boldsymbol{H}$, applied in some general direction, and the magnetic induction, $\boldsymbol{B}$, which includes the spontaneous magnetization, $\boldsymbol{M}_0$. Our model can naturally be extended to include any arbitrary number of FSs. We perform the first of the Klemm-Clem (KC)-transformations [44, 33, 45] on the two distinct spin-split FSs, $x_i = \overline{m}_{i\sigma}^{-1/2} x'_{i\sigma}$, *etc.*,to map both ellipsoidal FSs onto spherical ones, where $\overline{m}_{i\sigma} = \frac{m_{i\sigma}(\boldsymbol{B})}{m_\sigma(\boldsymbol{B})}$ and

$m_\sigma(\boldsymbol{B}) = [m_{1\sigma}(\boldsymbol{B})m_{2\sigma}(\boldsymbol{B})m_{3\sigma}(\boldsymbol{B})]^{1/3}$ is the geometric mean effective mass on the σ FS. Figure 6.2 qualitatively depicts the two spherical FSs after the scale transformations are performed. Note that the transformations performed for each FS depend on the single particle effective masses $m_{i\sigma}$ relevant for the σ FS, and that each transformation changes the effective directions of $\boldsymbol{H}$ and $\boldsymbol{B}$ to $\boldsymbol{H}'_\sigma$ and $\boldsymbol{B}'_\sigma$ for the σ FS, which are different on the $\sigma =\uparrow,\downarrow$ FSs. In Fig. 6.2, the differently transformed fields are indicated by the arrow subscripts. We then rotate these transformed fields to the crystal z' axis direction, and finally apply isotropic scale transformations involving the anisotropy parameter $\alpha_\sigma(\theta,\phi)$ and obtain expressions for the transformed angles $\cos\theta'_\sigma = \sqrt{\overline{m}_{3\sigma}}\frac{\cos\theta}{\alpha_\sigma(\theta,\phi)}$, $etc.$, where

$$\alpha_\sigma(\theta,\phi) = [\overline{m}_{1\sigma}\sin^2\theta\cos^2\phi + \overline{m}_{2\sigma}\sin^2\theta\sin^2\phi + \overline{m}_{3\sigma}\cos^2\theta]^{1/2}. \tag{6.4}$$

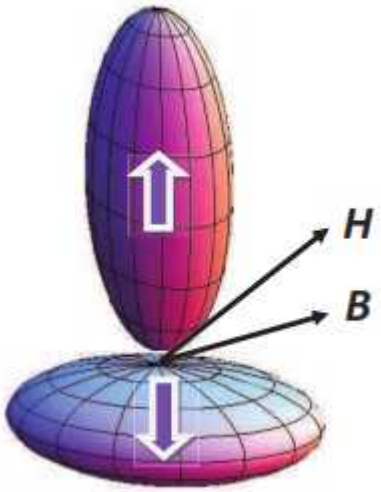

Figure 6.1: Plot of two distinct Fermi surfaces aligned along the crystal axes corresponding to up electron spin states. The applied magnetic field $\boldsymbol{H}$ and the magnetic induction $\boldsymbol{B}$ are indicated by the arrows.

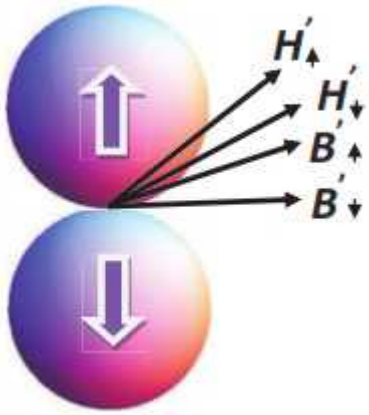

Figure 6.2: Plot of the ellipsoidal Fermi surfaces aligned along the crystal axes corresponding to the up and down electron spin states after transforming them into spherical ones. The transformed applied magnetic fields $\boldsymbol{H}'_{\uparrow}$ and $\boldsymbol{H}'_{\downarrow}$ and the transformed magnetic inductions $\boldsymbol{B}'_{\uparrow}$ and $\boldsymbol{B}'_{\downarrow}$ are in general different on each Fermi surface.

We also obtain $\epsilon_\sigma(k_{\sigma,\|}, n+1/2) = \frac{k^2_{\sigma,\|}}{2m_{\sigma,\|}} + \omega_{\sigma,\perp}(n+1/2)$, $\omega_{\sigma,\perp} = \frac{eB}{m_{\sigma,\perp}(\boldsymbol{B})}$, $m_{\sigma,\perp}(\boldsymbol{B}) = \frac{m_\sigma(\boldsymbol{B})}{\alpha_\sigma(\theta,\phi)}$, and $m_{\sigma,\|} = m_\sigma \alpha^2_\sigma(\theta,\phi)$ for the effective masses parallel and perpendicular to the transformed magnetic inductions on each of the two transformed FSs. Although obtaining the effective mass parallel to the field with the KC-transformations is non-trivial, we have shown that our results are consistent for any choice of $\boldsymbol{A}$ in all three crystallographic planes. More details are presented in Appendix B.

We begin with the expression for the total particle density for both spin-split Fermi surfaces in the presence of $\boldsymbol{B}$, $\Sigma_\sigma n_\sigma(\boldsymbol{B})$, which we assume to be independent of $\boldsymbol{B}$, in analogy with the Sommerfeld low temperature T expansion with $B = 0$. We obtain an asymptotic series expression involving the products $\Pi_\sigma(\boldsymbol{B}) = m_\sigma(\boldsymbol{B})\mu_\sigma(\boldsymbol{B})$ of the induction dependent chemical potential of

each FS, $\mu_\sigma(\boldsymbol{B})$, and the induction dependent geometric mean effective mass of each FS, $m_\sigma(\boldsymbol{B})$,

$$\sum_\sigma \Pi_\sigma^{3/2}(0) = \sum_\sigma \Pi_\sigma^{3/2}(\boldsymbol{B}) \times \left(1 + \sum_{n=0}^{\infty} a_n \left(\frac{eB\alpha_\sigma(\theta,\phi)}{\Pi_\sigma(\boldsymbol{B})}\right)^{2n+2}\right), \tag{6.5}$$

where

$$a_n = 3(-1)^{n+1}(2-2^{-2n})\zeta(2n+2)\frac{(4n-1)!!}{(4\pi)^{2n+2}}. \tag{6.6}$$

We then calculate the linear-T coefficient of the induction dependent specific heat, $\gamma(\boldsymbol{B})$. We define the entropy of the system in the usual way

$$S = -k_B \sum_{\mathbf{k}\sigma} [n_{F\sigma}\ln(n_{F\sigma}) + (1-n_{F\sigma})\ln(1-n_{F\sigma})], \tag{6.7}$$

where

$$n_{F\sigma} = \frac{1}{e^{\beta[\epsilon_\sigma(\boldsymbol{k}-e\boldsymbol{A})-\mu_\sigma(\boldsymbol{B})]}+1}, \tag{6.8}$$

k_B is the Boltzmann constant, and $\beta = \frac{1}{k_B T}$. The details of this calculation are presented in Appendix B. Making use of the thermodynamic relation $C_V = -\beta\frac{\partial(S/V)}{\partial\beta}$, we obtain the $B = 0$ linear T coefficient of the specific heat to be

$$\gamma(0) = \frac{k_B^2}{3\sqrt{2}} \sum_\sigma m_\sigma(0)\,\Pi_\sigma^{1/2}(0), \tag{6.9}$$

which agrees with textbook formulas for $\gamma(0)$.

For finite $\boldsymbol{B}$, the linear T-coefficient of the specific heat can be expanded in an asymptotic series

$$\begin{aligned}\gamma\left(\boldsymbol{B}\right) &= \frac{k_B^2}{3\sqrt{2}}\sum_{\sigma} m_\sigma\left(\boldsymbol{B}\right)\Pi_\sigma^{1/2}\left(\boldsymbol{B}\right) \\ &\times\left(1+\sum_{n=0}^{\infty}\lambda_n\left(\frac{eB\alpha_\sigma\left(\theta,\phi\right)}{\Pi_\sigma\left(\boldsymbol{B}\right)}\right)^{2n+2}\right), \end{aligned} \tag{6.10}$$

where $\lambda_n = \frac{1}{3}\left(4n+1\right)a_n$.

Specific heat of URhGe

To fit the specific heat data of Aoki $et\ al.$ [12], we first used a least-squares fit for the least anomalous a and b-axis directions of $\boldsymbol{H}$ to obtain the explicit field dependence of γ. Since SdH oscillations were found to vanish for URhGe with increasing $\boldsymbol{H}||\hat{\boldsymbol{b}}$, we assume that either the FS warps upon application of a strong magnetic field $\boldsymbol{H}$, or that the increased $\boldsymbol{H}$ moves the plane of electronic orbits away from an optimal cross-sectional area A of the FS, for which $\frac{\partial A}{\partial k_{\sigma,\|}} = 0$, thus quenching the SdH oscillations. In this latter scenario, we assume that this change in the observed portion of the FS with applied field will introduce a field dependence to the single particle effective mass parallel to the b-axis direction on the dominant FS. We assume that the single particle effective mass parallel to the b-axis direction on the dominant $\downarrow$ FS will have a Lorentzian field dependence of the form

$$m_{b,\downarrow}(\boldsymbol{B}) = \sum_{\alpha=\pm1}\frac{m_{b,\downarrow}(0)\left(H_0^2+(\Delta H)^2\right)}{(H+\alpha H_0)^2+(\Delta H)^2} + m_{b,\downarrow,\infty}, \tag{6.11}$$

where the fitting parameter $\mu_0 H$ is the magnetic field strength at the onset of the metamagnetic transition signaled by the peak in the $\frac{\partial M}{\partial H}$ data and the $\gamma_{\boldsymbol{H}\|b}$ data, which occurs for $\mu_0 H_0 = 12$T, $\mu_0 \Delta H$ is proportional to the half maximum width of the peak, $m_{b,\downarrow}(0)$ is the effective mass along the b-axis direction on the $\downarrow$ FS in zero field, and $m_{b,\downarrow,\infty}$ is the effective mass along the b-axis direction on the $\downarrow$ FS at high fields above the metamagnetic transition. All other single particle effective masses on both FSs are assumed to be independent of field, and all other field dependencies arise from the field dependent chemical potential of the dominant FS, $\mu_\downarrow = (\mu_\downarrow(0) + \delta\mu_\downarrow(\mu_0 H))$, where $\mu_\downarrow(0)$ and $\delta\mu_\downarrow$ are fitting parameters.

We substitute Eq. (6.11) into Eq. (6.10) with $\mu_\downarrow = (\mu_\downarrow(0) + \delta\mu_\downarrow \mu_0 H)$ and include only the dominant $\downarrow$ FS, and expand to leading order, obtaining

$$\begin{aligned} \gamma_b(H) &= \frac{k_B^2}{2\hbar^3\sqrt{3}} \lambda \times 10^3 \left[\mu_\downarrow(0) + \delta\mu_\downarrow \mu_0 H\right]^{1/2} \\ &\quad \times \left(\sum_{\alpha=\pm 1} \frac{m_\downarrow^3(0)\left(H_0^2 + (\Delta H)^2\right)}{(H + \alpha H_0)^2 + (\Delta H)^2} \right)^{1/2} + \gamma_{b,\infty} \end{aligned} \tag{6.12}$$

where $\lambda = 3.4 \times 10^{-5}$ m^3/mol is the conversion factor from m^3 to moles, which we have calculated based on 4 Uranium atoms per unit cell [12], and the dimensions of a unit cell given in [46], the factor of 10^3 is to convert from J to mJ, $m_\downarrow(0) \sim 180 m_e$ is the geometric mean mass for the $\downarrow$ FS in zero field, $\mu_0 H = 12.0$ T, $\mu_0 \Delta H = 0.97$ T, $\gamma_{b,\infty} = 150$ mJ/(molK^2), $\mu_\downarrow(0) = 20 \sim$ meV, and $\delta\mu_\downarrow = 3.1 \sim$ meV/T. We note that the positive value for $\delta\mu_\downarrow$ we obtain supports our hypothesis that the $\downarrow$ FS is the dominant FS contributing to $\gamma_b(\boldsymbol{H})$. We note that Eq. (6.10) had $\hbar = 1$, but to fit the experimental data, we have reintroduced $\hbar$ into Eq. (6.12). Figure 6.3 shows the theoretical fits along all three crystallographic directions. Details of this calculation are presented in Appendix B. It is important to note that the reentrant superconductivity in URhGe may arise from the increasing

effective mass along the b-axis direction, which seems to be the most plausible scenario in light of the specific heat data in the context of our current model. Field dependent enhancements of $m_{b\downarrow}$ in the context of upper critical field enhancements will be investigated in future work.

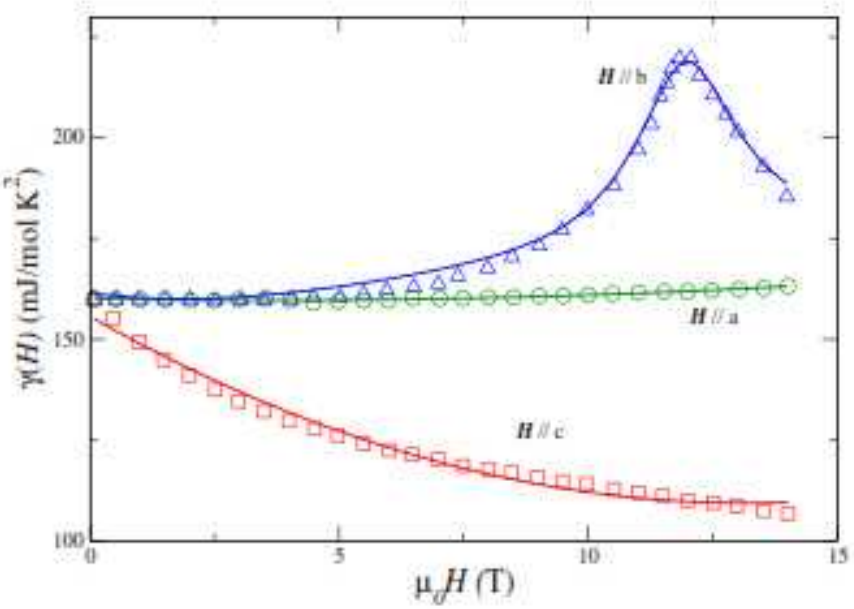

Figure 6.3: Experimental data for the linear T coefficient of the specific heat along all three distinct crystal axes of URhGe, γ, provided by D. Aoki [16], and theoretical fits to the data for externally applied magnetic elds $\boldsymbol{H}$ along the a (green), b (blue), and c (red) crystallographic directions. Solid color curves are fits of our model to the data.

CHAPTER 7: HELICAL STATES AND POSSIBLE P-WAVE SUPERCONDUCTIVITY IN Sr_2RuO_4

Background

The possible spin-triplet p-wave states for Sr_2RuO_4 are limited by the tetragonal crystal structure with two-dimensional square lattice point group symmetry C_{4v} to the six spin-orbit coupled states with the d-vectors $\hat{k}_x\hat{\boldsymbol{x}} \pm \hat{k}_y\hat{\boldsymbol{y}}$, $\hat{k}_y\hat{\boldsymbol{x}} \pm \hat{k}_x\hat{\boldsymbol{y}}$ and $(\hat{k}_x \pm i\hat{k}_y)\hat{\boldsymbol{z}}$ [78, 79]. It is important to note that the d-vectors are written in terms of the unit wave vectors $\hat{k}_x$, $\hat{k}_y$, and $\hat{k}_z$ as opposed to the wavevectors k_x, k_y, k_z, which possess magnitude. The first four d-vectors are non-chiral, and are known as the helical states. The last two are chiral, as discussed in the introduction. The two chiral states $\boldsymbol{d} = (\hat{k}_x \pm i\hat{k}_y)\hat{\boldsymbol{z}}$ with $\boldsymbol{d} \parallel \hat{\boldsymbol{c}}$ are believed to be stabilized near $\boldsymbol{H} = 0$ [49, 51], while with $H \sim H_{c2,ab}$, only the four helical states with d-vectors lying in the basal plane could be consistent with the in-plane $H_{c2,ab}$ measurements [61] by including the effects of Pauli limiting [66]. Contrary to the the assumption of very weak spin-orbit coupling, allowing the d-vector to rotate to a direction perpendicular to $\boldsymbol{H}$, that was argued to explain the Knight shift observations for both $\boldsymbol{H}||\hat{\boldsymbol{c}}$ and $\boldsymbol{H} \perp \hat{\boldsymbol{c}}$, sufficiently strong spin-orbit coupling should be assumed to allow for Zeeman energy splitting in spin-triplet pairing states [77]. In this case $\vec{S} \cdot \vec{L} \neq 0$, so that the energies for states with different total angular momentum J values are different, and thus the indistinguishability in the four helical states is lifted [50], since each state responds differently to $\boldsymbol{H}$, as illustrated in Fig. 7.1, two of them manifesting themselves by showing intrinsic four-fold in-plane anisotropies of $H_{c2,ab}(\phi)$ — a novel scenario other than earlier postulations of a multi-component order parameter [69] or the possible misalignment of two domains in the sample [61]. Only the $J = 2$, $J_z = \pm 2$ states are degenerate, while all others are not [79]. It is also possible to construct a generalized ABM state (Scharnberg-Klemm state) using two such degenerate helical states. Here we present

the calculation of the full angular and T dependencies of $H_{c2}(\theta, \phi, T)$ for the four helical states to try to set further restrictions on the possible pairing symmetries in Sr_2RuO_4.

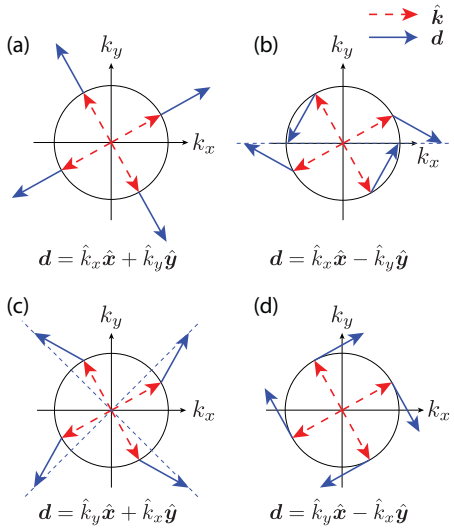

Figure 7.1: Illustration of the d-vectors for the helical states. In terms of $H_{c2,ab}(\phi)$, helical states shown in (a) and (d) are isotropic, while those in (b) and (c) exhibit four fold in-plane anisotropies due to the Pauli paramagnetic effect and strong spin-orbit coupling.

Model

The Fermi surface of Sr_2RuO_4 consists of three sheets: a quasi-two-dimensional γ band, and a pair of quasi-one-dimensional (α, β) bands [80]. Although still under debate [81, 82, 83], the cylindrical γ band is widely considered to be the primary source of p-wave pairing [51, 84]. The small c-axis dispersion in this nearly cylindrical γ Fermi surface can be incorporated by treating it as an elongated uniaxial ellipsoid, characterized by the effective mass anisotropy of the quasi-particles $m_c \gg m_a = m_b = m_{ab}$. The primary pair-breaking effects established in superconductivity fall into two categories: 1. the orbital effect arising from the competition be-

tween the coherence of two quasi-particles in a Cooper pair and their individual orbital motions in a magnetic field, i.e., the Landau levels governed by the effective vector potential $\boldsymbol{A}$ [85]; 2. the paramagnetic effect due to the Zeeman energy gained from the interactions between their spins and the field [63]. Highly anisotropic Zeeman interactions are expected in the layered compound Sr_2RuO_4, described here by an effective diagonal g-tensor $g = \mathrm{diag}(g_a, g_b, g_c)$ with $g_c \neq g_a = g_b = g_{ab}$ as in $-\mu_B \boldsymbol{S} \cdot g \cdot \overline{m}_{1/2} \cdot \boldsymbol{B}$, where μ_B is the Bohr magneton, $\boldsymbol{S}$ is the electron spin, $\overline{m}_{1/2} = \mathrm{diag}(\overline{m}_a^{1/2}, \overline{m}_b^{1/2}, \overline{m}_c^{1/2})$ is the diagonal tensor of the square roots of the relative effective masses $\overline{m}_\mu = m_\mu/m$ $(\mu = a, b, c)$ with geometric mean effective mass $m = (m_a m_b m_c)^{1/3}$, and the magnetic induction $\boldsymbol{B} = \mu_0 \boldsymbol{H} + \boldsymbol{M} = \nabla \times \boldsymbol{A}$, where $\boldsymbol{M}$ is the magnetization proportional to $\boldsymbol{H}$ for the non-ferromagnetic superconductor Sr_2RuO_4 [59]. If the d-vector is along the c axis, neither the chiral Anderson-Brinkman-Morel (ABM) state $\Delta_0(\hat{k}_x + i\hat{k}_y)\hat{\boldsymbol{z}}$ [87, 88] nor the Scharnberg-Klemm (SK) state $[\Delta_{0+}(\hat{k}_x + \hat{k}_y) + \Delta_{0-}(\hat{k}_x - i\hat{k}_y)]\hat{\boldsymbol{z}}$ [86, 72], nor generalizations of them obtained by setting $\hat{k}_x \to \sin(k_x a)$ and $\hat{k}_y \to \sin(k_y a)$ [74], could fit the in-plane $H_{c2,ab}$ measurements; for comparison, even the conventional s-wave state without Pauli limiting has $H_{c2}(T)$ well above the experimental data of Kittaka *et al.* for $\boldsymbol{H}||\hat{\boldsymbol{a}}$ (Fig. 7.2). Instead, the helical states have a chance for Pauli limiting to play the crucial role in suppressing $H_{c2,ab}(T)$, as long as $\boldsymbol{H}$ cannot cause the d-vectors to rotate.

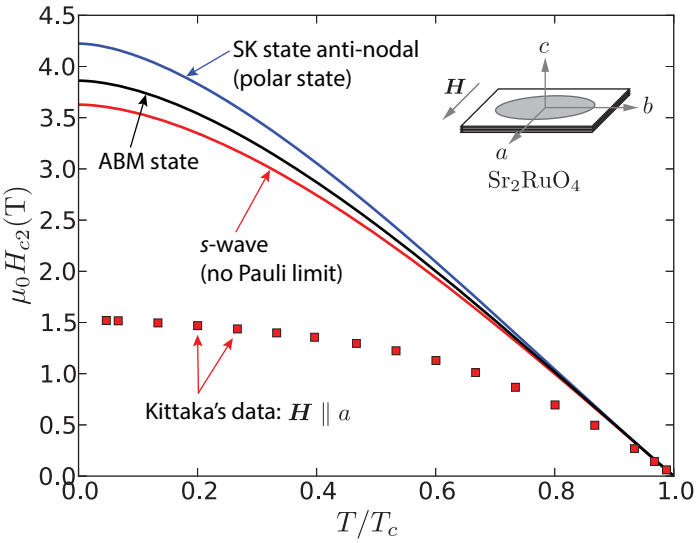

Figure 7.2: Fits to the chiral, ABM, SK and s-wave(without Pauli limiting) states to the in-pane $H_{c2,a}(T)$ measurements of Sr_2RuO_4. The in-plane $H_{c2,ab}(T)$ is strongly suppressed at low temperatures from that predicted from the orbital pairbreaking in these states. Note that in the anti-nodal direction, $H_{c2,ab}(T)$ of the chiral SK state has a first-order transition to that of the non-chiral polar state $\boldsymbol{d} = \Delta_0 k_x \hat{\boldsymbol{x}}$.

Hence we model Sr_2RuO_4 as a clean homogeneous weak-coupling type-II superconductor. Since close to H_{c2}, $\Delta(\boldsymbol{R}) = \sum_{n=0}^{\infty} a_n \, |n(\boldsymbol{R})\rangle$ for the vortex lattice in the mixed state, is constructed from the harmonic oscillator states $|n\rangle$, and is vanishingly small, the Gor'kov equations for p-wave superconductors with a single ellipsoidal Fermi surface can be linearized and transformed to yield [86, 89, 45]

$$\begin{aligned}\Delta(\boldsymbol{R}) = 2\pi T N(0) V_0 \sum_{\omega_n} \int \frac{\mathrm{d}\Omega_{\boldsymbol{k}'}}{4\pi} \int_0^{\infty} \mathrm{d}\xi \exp\left[-2|\omega_{\mathrm{n}}|\xi\right] \\ \times \exp\left[-i \, \mathrm{sgn}\omega_n \xi \boldsymbol{v}_F(\hat{\boldsymbol{k}}') \cdot \left(\alpha \nabla_{\boldsymbol{R}}/i + 2e\boldsymbol{A}\right)\right] \Delta(\boldsymbol{R}) \\ \times \left(\left|\boldsymbol{d}(\hat{\boldsymbol{k}}')\right|^2 + \left[\cos(\alpha g_{\mathrm{eff}} \mu_B B \xi) - 1\right] \left|d_z(\hat{\boldsymbol{k}}')\right|^2\right),\end{aligned} \tag{7.1}$$

where $N(0)$ is the density of states per spin at the Fermi level, V_0 is the pairing amplitude, ω_n are the fermion Matsubara frequencies, $\boldsymbol{v}_F = \boldsymbol{k}_F/m$ is the effective Fermi velocity, $\alpha = (\overline{m}_{ab}\sin^2\theta + \overline{m}_c\cos^2\theta)^{1/2}$ characterizes the geometric anisotropy of the Fermi surface, $g_{\rm eff} = \left[g_c^2\cos^2\theta' + g_{ab}^2\sin^2\theta'\right]^{1/2}$ is the effective g-factor experienced by the spins with $\cos\theta' = \sqrt{\overline{m}_c}\cos\theta/\alpha$, e is the electronic charge and the convention $\hbar = c = k_B = 1$ is adopted. We note that the Klemm-Clem (KC) transformations have been performed so that the $\hat{\boldsymbol{z}}'$ direction in (7.1) is always along $\boldsymbol{B}'$ [44, 33, 45].

All of the helical states in Fig. 7.1 are degenerate in terms of the KC transformed $\left|\boldsymbol{d}(\hat{\boldsymbol{k}}')\right|^2 = (\hat{k}'_x\cos\theta' + \hat{k}'_z\sin\theta')^2 + \hat{k}'^2_y$. However, the z-components $\left|d_z(\hat{\boldsymbol{k}}')\right|^2 = |\hat{\boldsymbol{B}}'\cdot\boldsymbol{d}(\hat{\boldsymbol{k}}')|^2$, which contribute to the Zeeman energy, are distinct for each of the four helical states. For the helical state $\boldsymbol{d} = \hat{k}_x\hat{\boldsymbol{x}} - \hat{k}_y\hat{\boldsymbol{y}}$ in Fig. 7.1(b), the KC transformed

$$\left|d_z(\hat{\boldsymbol{k}}')\right|^2 = \left(g_{ab}/g_{\rm eff}\right)^2\sin^2\theta'\left[(\hat{k}'_x\cos\theta' + \hat{k}'_z\sin\theta')\cos 2\phi - \hat{k}'_y\sin 2\phi\right]^2, \tag{7.2}$$

is anisotropic in the basal plane[44, 33], where $\phi' = \phi$ for $m_a = m_b$, and for consistency we set $\hat{k}'_y \to \hat{k}'_x$ and $\hat{k}'_x \to -\hat{k}'_y$. $\left|d_z(\hat{\boldsymbol{k}}')\right|^2$ in state (c) is obtained from that of helical state (b) in (7.2) by letting $\phi \to \phi - \pi/4$, while $\left|d_z(\hat{\boldsymbol{k}}')\right|^2$ for the helical states (a) and (d) are respectively obtained by setting $\phi = 0$ and $\phi = \pi/4$ in (7.2). These latter two helical states are therefore isotropic in the basal plane. Accordingly, the helical state (b) with $\boldsymbol{d} = \hat{k}_x\hat{\boldsymbol{x}} - \hat{k}_y\hat{\boldsymbol{y}}$ can be used to present the formulation.

We introduce the dimensionless quantities $t = T/T_c(0)$, $b_{c2} = B_{c2}/B_0$ and for the g-tensor (via its elements) $\bar{g} = g/g_0$, where $T_c(0) = (2e^C\omega_{\rm c}/\pi)e^{-1/N(0)V_0}$ is the superconducting transition temperature in zero field, $C = 0.577$ is the Euler constant, $\omega_{\rm c}$ is the energy cutoff from the BCS

theory, $B_0 = [2\pi T_c(0)]^2/2ev_F^2$ and $g_0 = 2\pi T_c(0)/\mu_B B_0$. Equation (7.1) can be expanded as [86]

$$\left[-\ln t + \alpha_n^{(p)} + \alpha_n^{(a)}\right] a_n + \beta_{n-2}^{(+)} a_{n-2} + \beta_n^{(-)} a_{n+2} = 0. \tag{7.3}$$

The upper critical field b_{c2} is embedded in the coefficients

$$\begin{aligned}
\alpha_n^{(p)} &= \int_0^\infty \psi \frac{\sinh^2\psi}{\cosh^3\psi} \int_0^\infty \rho \frac{t\sqrt{2/\alpha b_{c2}}}{\sinh\left(t\sqrt{2/\alpha b_{c2}}\rho\cosh\psi\right)} \\
&\qquad \times \left[e^{-\frac{1}{2}\rho^2} L_n^{(0)}(\rho^2) F^{(p)} - \sin^2\theta'\right], \qquad (7.4) \\
\alpha_n^{(a)} &= \int_0^\infty \psi \frac{1}{2\cosh^3\psi} \int_0^\infty \rho \frac{t\sqrt{2/\alpha b_{c2}}}{\sinh\left(t\sqrt{2/\alpha b_{c2}}\rho\cosh\psi\right)} \\
&\qquad \times \left[e^{-\frac{1}{2}\rho^2} L_n^{(0)}(\rho^2) F^{(a)} - (1+\cos^2\theta')\right], \qquad (7.5) \\
\beta_n^{(\pm)} &= \int_0^\infty \psi \frac{1}{4\cosh^3\psi} \int_0^\infty \rho \frac{t\sqrt{2/\alpha b_{c2}}}{\sinh\left(t\sqrt{2/\alpha b_{c2}}\rho\cosh\psi\right)} \\
&\qquad \times e^{-\frac{1}{2}\rho^2} \frac{-\rho^2}{\sqrt{(n+2)(n+1)}} L_n^{(2)}(\rho^2) \\
&\times \left[-\sin^2\theta' + G(\cos^2\theta'\cos^2 2\phi - \sin^2 2\phi) \pm iG\cos\theta'\sin 4\phi\right], \qquad (7.6)
\end{aligned}$$

where the $L_n^{(m)}$ are the associated Laguerre polynomials, and

$$F^{(p)} = \sin^2\theta' + G\sin^2\theta'\cos^2 2\phi, \tag{7.7}$$

$$F^{(a)} = 1 + \cos^2\theta' + G(\cos^2\theta'\cos^2 2\phi + \sin^2 2\phi) \tag{7.8}$$

with $G = \left[\cos\left(\bar{g}_{\text{eff}}\sqrt{\alpha b_{c2}/2}\right) - 1\right]\left(\bar{g}_{ab}/\bar{g}_{\text{eff}}\right)^2 \sin^2\theta'$. The solution to (7.3) constitutes the determinant of the (infinite order) tridiagonal matrix constructed from the coefficients of a_n ($n = 0, 2, \ldots$), which can be solved numerically for arbitrary t. To calculate $B_{c2} = \mu_0 H_{c2}$ for non-magnetic superconductors, usually the first 3 or 4 orders produce sufficiently accurate results to show all of the essential features.

Results

Figure 7.3 shows our fits to the angular dependent $H_{c2,a}(\theta, T)$ measurements of Kittaka *et al.* on a sample of Sr_2RuO_4 ($T_c(0) = 1.503$ K) [61] using helical state (b) with $\boldsymbol{d} = \hat{k}_x\hat{\boldsymbol{x}} - \hat{k}_y\hat{\boldsymbol{y}}$. The appropriateness of an elongated uniaxial ellipsoidal Fermi surface for the γ band is verified by the huge effective mass anisotropy $m_c/m_{ab} = 1067$ estimated from the slopes of $H_{c2,a}(T)$ at $T_c(0)$ in the $[100]$ and $[001]$ crystal directions where Pauli limiting effects are negligible. Down to low t, a suitable choice of the effective g-factor will further suppress the H_{c2} curves, especially for those with $\theta < 5^\circ$ (c.f. figure 7.2). Although the $H_{c2,a}(T, \theta > 5^\circ)$ data appear to follow the anisotropic effective mass model [61, 72, 45], one should nevertheless take into consideration the intrinsic anisotropy of $H_{c2}(\theta)$ raising from the point nodal structures of the helical states ($[H_{c2,ab}/H_{c2,c}]_{T\to T_c(0)} = \sqrt{2}$ for an isotropic Fermi surface) [72]. For an overall best fit, the effective g-tensor was evaluated to have the diagonal elements $\bar{g}_c = 0.2$ and $\bar{g}_{ab} = 1.9$. Obviously, the small-valued $\bar{g}_c$ doesn't contribute to $H_{c2,c}$ since $\boldsymbol{d} \perp \hat{\boldsymbol{c}}$ for the helical states, but it plays a role in determining $H_{c2}(\theta)$ for $(0^\circ < \theta < 90^\circ)$.

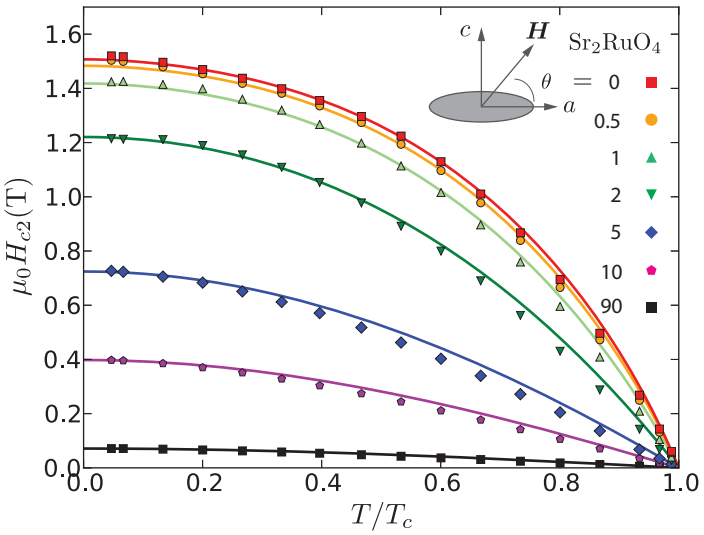

Figure 7.3: Fits to the angular dependant $H_{c2,a}(\theta, T)$ measurements of $SrRuO_4$ using helical state (b) with $\boldsymbol{d} = \hat{k_x}\hat{\boldsymbol{x}} - \hat{k_y}\hat{\boldsymbol{y}}$ with $\overline{g}_{ab} = 1.9$, $\overline{g}_c = 0.2$.

We remark that all the helical states listed in Fig. 7.1 could equally well fit the data shown in Fig 7.3, as the differences in their H_{c2} values only appear in their in-plane (ϕ) anisotropies. As seen from (7.1), in the absence of Pauli limiting, $H_{c2,ab}(\phi)$ for the helical states are isotropic in the basal plane. However, with the fitting parameter $\bar{g}_{ab} = 1.9$, the $H_{c2,ab}(\phi)$ at 0.13 K for the helical states (b) and (c) in Fig. 7.1 exhibit four-fold in-plane azimuthal anisotropies with a relative amplitude as large as 30% (Fig. 7.4(a)) and a phase shift of $\pi/4$ between them, while those for states (a) and (d) remain isotropic in the ab plane. The observed in-plane anisotropy of $H_{c2,ab}(\phi)$ is at most 3% and disappears either above 0.8 K or with a field misalignment of less than 1° [61, 67]. The calculated anisotropy for helical state (b) with $\boldsymbol{d} = \hat{k}_x\hat{\boldsymbol{x}} - \hat{k}_y\hat{\boldsymbol{y}}$ state persists for $T > T_c/2$ and for field misalignments greater than 2° (Fig. 7.4(b)). Thus, this parallel-spin p-wave state can explain the strong Pauli limiting for $\boldsymbol{B} \perp \hat{\boldsymbol{c}}$, but the details are not in precise agreement with the experimental observations [61, 67].

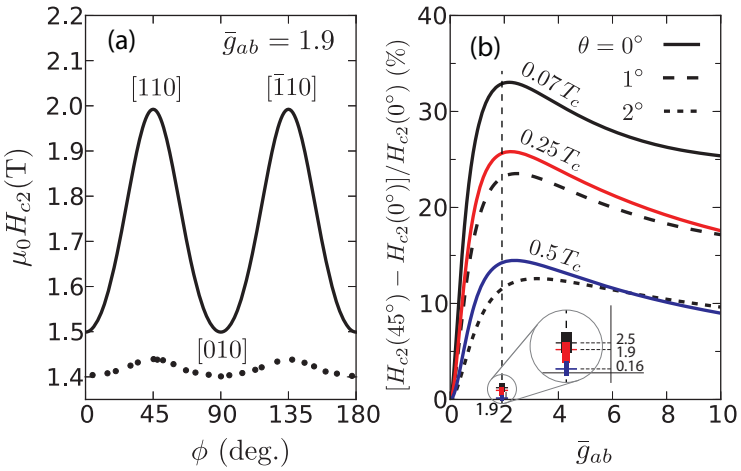

Figure 7.4: In-plane $H_{c2,ab}(\phi)$ anisotropy of helical state (b) with $\boldsymbol{d} = \hat{k}_x\hat{\boldsymbol{x}} - \hat{k}_y\hat{\boldsymbol{y}}$. (a) $H_{c2,ab}(\phi)$ with an effective g-factor $\bar{g}_{ab} = 1.9$ at 0.13 K . The amplitude of the predicted anisotropy (solid) is an order of magnitude larger than that (dotted curve) observed in Sr_2RuO_4 by Mao *et al.*[67]. (b) Effects of $g_{\rm eff}$ to the relative magnitudes of the in-plane anisotropy at various temperatures and field misalignments. Anisotropies comparable to the experiments only occur with small $\overline{g}_{ab}$ values. The symbols at the bottom represent the data of Kittaka *et al.*[61].

Discussion

A multi-component order parameter proposed to interpret the in-plane $H_{c2,ab}(\phi)$ anisotropy in reference [67] turns out to have a similar problem of a large magnitude of the in-plane anisotropy [69]. There could also be two slightly misaligned crystals in the same sample [61], and the smaller region of the hysteretic magnetization data below 0.8 K in the more recent data of Yonezawa *et al.* than in the older Mao *et al.* and Deguchi *et al.* data are consistent with this scenario [60, 61, 62, 67]. Others think that this first-order transition below 0.8 K is more intrinsically due to a Fulde-Farrell-Larkin-Ovchinnikov state, entered below $0.55T_c$ (close to 0.8 K in Sr_2RuO_4) [90]. Based on the

present calculations, if the Pauli pair-breaking effect is demanded as the source for the suppression on $H_{c2,ab}$, helical state (b) with $\boldsymbol{d} = \hat{k}_x\hat{\boldsymbol{x}} - \hat{k}_y\hat{\boldsymbol{y}}$ has the same four-fold anisotropy with the same phase as in the experiments. Helical state (c) with $\boldsymbol{d} = \hat{k}_y\hat{\boldsymbol{x}} + \hat{k}_x\hat{\boldsymbol{y}}$ has the four-fold anisotropy differing in phase by $\pi/4$. However, both of these azimuthal anisotropies are much stronger than that observed in experiment. However, the other helical (a) and (d) p-wave states with $\boldsymbol{d} = \hat{k}_x\hat{\boldsymbol{x}} + \hat{k}_y\hat{\boldsymbol{y}}$ and $\hat{k}_y\hat{\boldsymbol{x}} - \hat{k}_x\hat{\boldsymbol{y}}$ are predicted to have no azimuthal anisotropies at all. Including ab-planar anisotropy on the γ Fermi surface could lead to a small azimuthal anisotropy of $H_{c2}(90^\circ, \phi, T)$, but normally Fermi surface anisotropy is largest near to T_c. Thus, a single purported triplet-spin order parameter for Sr_2RuO_4 is still elusive. We note, however, that there are many examples in which the Knight shift observations have been misleading and/or are also in apparent conflict with the upper critical field results [76, 91], strongly suggesting that a new theory of the Knight shift might lead to a possible resolution of the symmetry of the order parameter in Sr_2RuO_4 [75, 76].

In summary, we studied the four helical p-wave states potentially realized in Sr_2RuO_4 at H_{c2} by fitting the angular dependent $H_{c2,a}(\theta, \phi, T)$ measurements, taking the Pauli paramagnetic effects into account by imposing strong spin-orbit coupling effects as the origin of the $H_{c2,ab}$ suppression. In the ranges of the fitting parameters, one of the four helical states was predicted to have in-plane $H_{c2}(90^\circ, \phi, T)$ four-fold azimuthal anisotropy with the same phase as observed, but both that azimuthal anisotropy and that from the (c) helical state with the anisotropy shifted by $\pi/4$ in phase, had amplitudes that were predicted to be much stronger than that observed in Sr_2RuO_4. The $H_{c2}(90^\circ, \phi, T)$ behaviors of the two other helical p-wave states were predicted to be completely independent of ϕ, as long as in-plane Fermi surface anisotropy could be safely ignored. Other attempts to fit an order parameter such as $\Delta_0[\sin(k_x a) + i\sin(k_y a)]$ with the low-T specific heat $C_V \sim T^2$ dependence failed to confront the very strong Pauli limiting of $H_{c2}(90^\circ, \phi, T)$ [74]. Thus, the thermodynamic zero-field specific heat measurements appear to be in direct conflict with the field-dependent thermodynamic specific heat and magnetization measurements of the upper critical

field [60, 61, 67, 62]. Further calculations to try to fit the excellent scanning tunneling microscopy results of Suderow *et al.* with a p-wave order parameter are also needed [73]. A point node in a helical p-wave order parameter might smear the sharp density of states walls they observed, but an accurate calculation is needed to quantify this possible disagreement.

CHAPTER 8: CONCLUSION

This thesis presented the many aspects of the candidate ferromagnetic p-wave superconductors URhGe and UCoGe. These heavy fermion materials have long been purported to be quintessential parallel spin superconductors, because of their anomalous H_{c2} curves. However, more detailed experimental studies are necessary to establish the order parameter symmetry in these materials. To this end, this thesis presented quantum field theoretical calculations of the full angular and temperature dependencies of the upper critical induction $B_{c2}(\theta, \phi, T)$ for the polar/CBS state in the case of URhGe, and the chiral ABM and SK states in the case of UCoGe and possible Sr_2RuO_4. These theoretical studies predicts anomalous $B_{c2}(\theta)$ anisotropy for fixed effective mass anisotropy ($\gamma^2(\phi)$) for both the polar/CBS state and the chiral ABM and SK states. This thesis also presented a double ellipsoidal Fermi surface model for ferromagnetic superconductors such as URhGe, which was used to understand this material's anomalous specific heat measurements. This model proposed a field dependent effective mass, which could help understand the reentrant superconducting phase in URhGe and possibly UCoGe. This thesis also discussed the helical p-wave states and presented fits to the upper critical field data of Sr_2RuO_4 with an anisotropic g-tensor.

Distinguishing effective mass anisotropy from order parameter anisotropy from H_{c2} curves has been the greatest challenge in identifying the symmetry of the order parameter in UCoGe and URhGe. The help the experimentalists in pinpointing the symmetry of the order parameter (i.e. polar/CBS, chiral SK, etc.), and to help discover new materials with these p-wave symmetries, we have made predictions about the anisotropy of $H_{c2}(\theta)$ at various temperatures and effective masses present in $\gamma^2(\phi)$. For the polar/CBS p-wave state, we predicted an anomalous peak at $\theta^* < 90^\circ$ and $180^\circ - \theta^*$ in $B_{c2}(\theta)$, which occurs for $\gamma^2(\phi) > 3$. This anomalous peak was attributed to a competition between order parameter anisotropy and effective mass anisotropy. The anisotropy of B_{c2} for the chiral ABM state exhibited a similar anomalous peak, however it is

observed only for $\gamma^2(\phi) < 2$. The anisotropy of B_{c2} for the chiral SK state was found to be much more interesting. We observed a kink in $B_{c2}(\theta)$ at $\theta = \theta^*$, which signaled the onset of a first order phase transition from a chiral SK state ($\theta < \theta^*$) to a non-chiral polar state $\theta > \theta^*$. These anomalous signatures found in the anisotropy of B_{c2} may help experimentalists in identifying the order parameter symmetry in UCoGe and URhGe, and possibly discover new materials with these p-wave symmetries.

Understanding the mechanism that drives the reentrant superconducting phase in URhGe and the anomalous S-shaped $H_{c2}(T)$ curve for $\boldsymbol{H} \parallel \hat{\boldsymbol{b}}$ in UCoGe has been a driving force in the active research of these exotic materials. To this end, we have developed a double ellipsoidal Fermi surface model for ferromagnetic superconductors in the normal state, and subsequently used the model to understand the anomalous specific heat measurements of on URhGe conducted by Aoki $et\ al.$ We assumed that the effective mass along one of the crystallographic directions on one of the Fermi surfaces is field dependent, whose form was fit to a Lorentzian function from the $\frac{\partial M}{\partial H}$ data of Aoki $et\ al.$ Using this field Lorentzian field dependent mass and our expression for the field dependent linear T coefficient of the specific heat γ, we fit the $\gamma(\boldsymbol{B})$ for all three crystallographic directions. This model of a field dependent mass could help to understand the reentrant phase and upward curvature in $H_{c2}(T)$ for URhGe and UCoGe respectively in future upper critical field calculations.

Although Sr_2RuO_4 has long been purported to have a chiral ABM p-wave order parameter of the form $\Delta(\boldsymbol{k}) = \Delta_{0,\pm}(k_x \pm ik_y)$, or the more general chiral SK state order parameter which is a linear combination of the $\pm$ chiralities of the ABM state $\Delta(\boldsymbol{k}) = \sum_\sigma \Delta_{0,\sigma}(k_x + i\sigma k_y)$, we have shown that the upper critical fields of these states do not fit the H_{c2} data of Kittika $et\ al.$ We have also shown that the H_{c2} data of Kittika can not be explained by a conventional s-wave order parameter without Pauli limiting. To complicate things, the upper critical field is strongly Pauli limited parallel to the layers, which is inconsistent with the Knight shift measurements. We

have proposed helical p-wave order parameters, which have a chance of explaining the strongly Pauli limited upper critical fields, to fit the data of Kittika. We have included the effect of highly anisotropic Zeeman interactions, which is expected for a layered superconductor such as Sr_2RuO_4, by incorporating a g-tensor. We have used this model to fit the data of Kittika $et\ al.$, which might help to settle the controversy revolving around Sr_2RuO_4.

In conclusion, we propose more experiments on UCoGe, URhGe, and especially on Sr_2RuO_4, including angular dependent measurements of the upper critical field, in order to concretely establish the symmetry of the order parameter in these magnificent materials. We also encourage experimentalists working with potential p-wave superconductors to check for anomalous double peaks in the anisotropy of B_{c2}, as well as kinks which could be a signal of a first order phase transition from a chiral SK state to a non-chiral polar/CBS state. These novel features may prove to be very useful in identifying these exotic states of matter. We also encourage theorists working to understand the reentrant field in URhGe and the anomalous S-shaped $H_{c2,\|\hat{b}}$ to include the effects of a field dependent mass as presented in chapter 6. This might help to explain the upward curvature in $H_{c2}(T)$ for UCoGe along all three crystallographic direction, including the S-shaped curve, as well as the reentrant superconducting phase of URhGe.

APPENDIX A: DERIVATION OF GREEN FUNCTIONS FOR ANGULAR DEPENDENT CALCULATIONS OF H_{c2} WITH A GENERAL ELLIPSOIDAL FERMI SURFACE

Here we present the details of the KC transformations on the Green functions and the resulting derivation of the microscopic gap equation [44], and correct some typos in the literature [13]. Here we assume the charge of an electron is $-e$. The combined anisotropic scale transformation, rotation, and isotropic scale transformation may be written as

$$
\begin{aligned}
x_\mu &= \frac{1}{\alpha\sqrt{\overline{m}_\mu}} \sum_\nu \lambda_{\nu\mu} \tilde{x}_\nu, && \text{(A.1)} \\
\frac{\partial}{\partial x_\mu} &= \alpha\sqrt{\overline{m}_\mu} \sum_\nu \lambda_{\nu\mu} \frac{\partial}{\partial \tilde{x}_\nu}, && \text{(A.2)} \\
B_\mu &= \frac{\alpha}{\sqrt{\overline{m}_\mu}} \sum_\nu \lambda_{\nu\mu} \tilde{B}_\nu \\
&= \frac{\alpha}{\sqrt{\overline{m}_\mu}} \lambda_{3\mu} \tilde{B}_3, && \text{(A.3)} \\
A_\mu &= \sqrt{\overline{m}_\mu} \sum_\nu \lambda_{\nu\mu} \tilde{A}_\nu, && \text{(A.4)}
\end{aligned}
$$

where

$$
\lambda = \begin{pmatrix} \sin\phi' & -\cos\phi' & 0 \\ \cos\theta'\cos\phi' & \cos\theta'\sin\phi' & -\sin\theta' \\ \sin\theta'\cos\phi' & \sin\theta'\sin\phi' & \cos\theta' \end{pmatrix} \qquad \text{(A.5)}
$$

and

$$
\sum_\mu \lambda_{\nu\mu}\lambda_{\nu'\mu} = \delta_{\nu\nu'}. \qquad \text{(A.6)}
$$

Note that $\lambda_{13} = 0$, $\overline{m}_\mu = m_\mu/m$, $m = (m_1 m_2 m_3)^{1/3}$, and $\alpha = \alpha(\theta, \phi)$ is given by Eq. (4.5) of the text [33, 44]. The transformed angles obtained after the anisotropic scale transformation are given

by

$$\cos\theta' = \frac{\sqrt{\overline{m}_3}}{\alpha}\cos\theta, \tag{A.7}$$

$$\sin\theta' = \frac{\overline{\alpha}(\phi)}{\alpha}\sin\theta, \tag{A.8}$$

$$\cos\phi' = \frac{\sqrt{\overline{m}_1}\cos\phi}{\overline{\alpha}(\phi)}, \tag{A.9}$$

$$\sin\phi' = \frac{\sqrt{\overline{m}_2}\sin\phi}{\overline{\alpha}(\phi)}, \tag{A.10}$$

$$\overline{\alpha}(\phi) = \alpha(\pi/2,\phi) = [\overline{m}_1\cos^2\phi + \overline{m}_2\sin^2\phi]^{1/2}$$

$$= \frac{\overline{m}_3}{\gamma^2(\phi)} \tag{A.11}$$

We begin with Eqs. (4.6)-(4.7) of the text. To transform the quadratic operators on the left-hand sides, we expand the gradient and vector potential components with Eqs. (A.2) and (A.4), and make use of the rotation identity, Eq. (A.6). With regard to the delta function in Eq. (4.6), it is easily seen that

$$\delta^3(\boldsymbol{r}) = \int \frac{d^3\boldsymbol{k}}{(2\pi)^3} e^{i\boldsymbol{k}\cdot\boldsymbol{r}} \tag{A.12}$$

$$\rightarrow \alpha^3 \int \frac{d^3\tilde{\boldsymbol{k}}}{(2\pi)^3} e^{i\tilde{\boldsymbol{k}}\cdot\tilde{\boldsymbol{r}}} \tag{A.13}$$

$$= \alpha^3\delta^3(\tilde{\boldsymbol{r}}). \tag{A.14}$$

We note that $d^3\boldsymbol{k} \rightarrow \alpha^3(\overline{m}_1\overline{m}_2\overline{m}_3)^{1/2}d^3\tilde{\boldsymbol{k}} = \alpha^3 d^3\tilde{\boldsymbol{k}}$, as the transformed volume element is invariant under all rotations. Note that to transform $\boldsymbol{k}\cdot\boldsymbol{r}$ in the exponent, expand the components of $\boldsymbol{r}$ and $\boldsymbol{k}$ according to Eqs. (A.1) and (A.2), and again make use of the rotation identity, Eq. (A.6). Note that the scalar product of two vectors is invariant under all rotations.

We then may write the transformed Eqs. (4.6) and (4.7) of the text as

$$\Big[i\omega_n - \frac{1}{2\tilde{m}}\Big(\tilde{\boldsymbol{\nabla}}/i - \tilde{e}\tilde{\boldsymbol{A}}(\tilde{\boldsymbol{r}})\Big)^2 + \mu_\sigma(\tilde{B}_3)\Big]\tilde{G}_{\sigma\sigma'}(\tilde{\boldsymbol{r}},\tilde{\boldsymbol{r}}',\omega_n) + \sum_\rho \int d^3\tilde{\boldsymbol{\xi}}\tilde{\Delta}_{\sigma\rho}(\tilde{\boldsymbol{r}},\tilde{\boldsymbol{\xi}})\tilde{F}^\dagger_{\rho\sigma'}(\tilde{\boldsymbol{\xi}},\tilde{\boldsymbol{r}}',\omega_n) = \alpha^3\delta_{\sigma\sigma'}\delta^3(\tilde{\boldsymbol{r}}-\tilde{\boldsymbol{r}}'), \quad \text{(A.15)}$$

$$\Big[-i\omega_n - \frac{1}{2\tilde{m}}\Big(i\tilde{\boldsymbol{\nabla}} - \tilde{e}\tilde{\boldsymbol{A}}(\tilde{\boldsymbol{r}})\Big)^2 + \mu_\sigma(\tilde{B}_3)\Big]\tilde{F}^\dagger_{\sigma\sigma'}(\tilde{\boldsymbol{r}},\tilde{\boldsymbol{r}}',\omega_n) - \sum_\rho \int d^3\tilde{\boldsymbol{\xi}}\tilde{\Delta}^*_{\sigma\rho}(\tilde{\boldsymbol{r}},\tilde{\boldsymbol{\xi}})\tilde{G}_{\rho\sigma'}(\tilde{\boldsymbol{\xi}},\tilde{\boldsymbol{r}}',\omega_n) = 0, \quad \text{(A.16)}$$

where

$$\tilde{e} = e/\alpha, \quad \text{(A.17)}$$

and

$$\tilde{m} = m/\alpha^2 \quad \text{(A.18)}$$

are the renormalized electronic charge magnitude and mass due to the transformations, and $\tilde{G}$, $\tilde{F}^\dagger$ and $\tilde{\Delta}$ are complicated functions of the transformed variables, since the interaction is best determined in momentum space, as in Eq. (4.3).

Now in order to make the transformed functions gauge invariant, we require the equations of motion in the variables $\tilde{\boldsymbol{r}}$ and $\tilde{\boldsymbol{r}}'$ to be respectively invariant under

$$\tilde{\boldsymbol{A}}(\tilde{\boldsymbol{r}}) = \tilde{\boldsymbol{A}}_0(\tilde{\boldsymbol{r}}) + \tilde{\boldsymbol{\nabla}}\Phi(\tilde{\boldsymbol{r}}), \quad \text{(A.19)}$$

$$\tilde{\boldsymbol{A}}(\tilde{\boldsymbol{r}}') = \tilde{\boldsymbol{A}}_0(\tilde{\boldsymbol{r}}') + \tilde{\boldsymbol{\nabla}}'\Phi(\tilde{\boldsymbol{r}}'), \quad \text{(A.20)}$$

where $\tilde{A}_0$ can be taken to vanish. We then may write

$$\tilde{G}_{\sigma\sigma'}(\tilde{\boldsymbol{r}},\tilde{\boldsymbol{r}}',\omega_n) = \overline{\tilde{G}}_{\sigma\sigma'}(\tilde{\boldsymbol{r}},\tilde{\boldsymbol{r}}',\omega_n)e^{i\tilde{e}[\Phi(\tilde{\boldsymbol{r}})-\Phi(\tilde{\boldsymbol{r}}')]}, \tag{A.21}$$

$$\tilde{F}^{\dagger}_{\sigma\sigma'}(\tilde{\boldsymbol{r}},\tilde{\boldsymbol{r}}',\omega_n) = \overline{\tilde{F}}^{\dagger}_{\sigma\sigma'}(\tilde{\boldsymbol{r}},\tilde{\boldsymbol{r}}',\omega_n)e^{-i\tilde{e}[\Phi(\tilde{\boldsymbol{r}})+\Phi(\tilde{\boldsymbol{r}}')]}, \tag{A.22}$$

$$\tilde{G}_{\sigma\sigma'}(\tilde{\boldsymbol{r}},\tilde{\boldsymbol{r}}',-\omega_n) = \overline{\tilde{G}}_{\sigma\sigma'}(\tilde{\boldsymbol{r}},\tilde{\boldsymbol{r}}',-\omega_n)e^{i\tilde{e}[\Phi(\tilde{\boldsymbol{r}}')-\Phi(\tilde{\boldsymbol{r}})]}, \tag{A.23}$$

$$\tilde{F}_{\sigma\sigma'}(\tilde{\boldsymbol{r}},\tilde{\boldsymbol{r}}',\omega_n) = \overline{\tilde{F}}_{\sigma\sigma'}(\tilde{\boldsymbol{r}},\tilde{\boldsymbol{r}}',\omega_n)e^{i\tilde{e}[\Phi(\tilde{\boldsymbol{r}})+\Phi(\tilde{\boldsymbol{r}}')]}, \tag{A.24}$$

as was done long ago for isotropic superconductors [37].

We then examine the bare Green functions in the absence of any pairing. We have

$$\Big[\pm i\omega_n - \frac{1}{2\tilde{m}}\Big(\tilde{\boldsymbol{\nabla}}/i \mp \tilde{e}\tilde{\boldsymbol{A}}(\tilde{\boldsymbol{r}})\Big)^2 + \mu_\sigma(\tilde{B}_3)\Big]\tilde{G}^0_{\sigma\sigma'}(\tilde{\boldsymbol{r}},\tilde{\boldsymbol{r}}',\pm\omega_n) = \delta_{\sigma\sigma'}\alpha^3\delta(\tilde{\boldsymbol{r}}-\tilde{\boldsymbol{r}}'). \tag{A.25}$$

These forms are easily shown to satisfy

$$\tilde{G}^0_{\sigma\sigma'}(\tilde{\boldsymbol{r}},\tilde{\boldsymbol{r}}',\pm\omega_n) = \overline{\tilde{G}}^0_{\sigma\sigma'}(\tilde{\boldsymbol{r}},\tilde{\boldsymbol{r}}',\pm\omega_n)e^{\mp i\tilde{e}\phi(\tilde{\boldsymbol{r}},\tilde{\boldsymbol{r}}')}, \tag{A.26}$$

where

$$\phi(\tilde{\boldsymbol{r}},\tilde{\boldsymbol{r}}') = \int_{\tilde{\boldsymbol{r}}}^{\tilde{\boldsymbol{r}}'} \tilde{A}(\tilde{\boldsymbol{s}})\cdot d\tilde{\boldsymbol{s}} = \Phi(\tilde{\boldsymbol{r}}')-\Phi(\tilde{\boldsymbol{r}}), \tag{A.27}$$

precisely as for a spherical Fermi surface, except that $e \to \tilde{e}$ and $m \to \tilde{m}$. We note that $\overline{\tilde{G}}^0_{\sigma\sigma'}(\tilde{\boldsymbol{r}},\tilde{\boldsymbol{r}}',\pm\omega_n)$ satisfies

$$\Big[\pm i\omega_n + \frac{\tilde{\boldsymbol{\nabla}}^2}{2\tilde{m}} + \mu_\sigma(\tilde{B}_3)\Big]\overline{\tilde{G}}^0_{\sigma\sigma'}(\tilde{\boldsymbol{r}},\tilde{\boldsymbol{r}}',\pm\omega_n) = \delta_{\sigma\sigma'}\alpha^3\delta^3(\tilde{\boldsymbol{r}}-\tilde{\boldsymbol{r}}'), \tag{A.28}$$

which can be taken to be a function of $\tilde{\boldsymbol{r}} - \tilde{\boldsymbol{r}}'$, and can therefore be Fourier transformed. Writing

$$\delta^3(\tilde{\boldsymbol{r}} - \tilde{\boldsymbol{r}}') = \int \frac{d^3\tilde{\boldsymbol{k}}}{(2\pi)^3} e^{i\tilde{\boldsymbol{k}}\cdot(\tilde{\boldsymbol{r}}-\tilde{\boldsymbol{r}}')}, \tag{A.29}$$

$$\overline{\tilde{G}}^0_{\sigma\sigma'}(\tilde{\boldsymbol{r}} - \tilde{\boldsymbol{r}}', \pm\omega_n) = \alpha^3 \int \frac{d^3\tilde{\boldsymbol{k}}}{(2\pi)^3} \overline{\tilde{G}}^0_{\sigma\sigma'}(\tilde{\boldsymbol{k}}, \pm\omega_n) e^{i\tilde{\boldsymbol{k}}\cdot(\tilde{\boldsymbol{r}}-\tilde{\boldsymbol{r}}')}, \tag{A.30}$$

and using Eq. (A.28), we easily obtain

$$\overline{\tilde{G}}^0_{\sigma\sigma'}(\tilde{\boldsymbol{k}}, \pm\omega_n) = \frac{\delta_{\sigma\sigma'}}{\pm i\omega_n - \tilde{\boldsymbol{k}}^2/(2\tilde{m}) + \mu_\sigma(\tilde{B}_3)}. \tag{A.31}$$

To obtain $\overline{\tilde{G}}^0_{\sigma\sigma'}(\tilde{\boldsymbol{r}}, \tilde{\boldsymbol{r}}', \pm\omega_n)$ in real space, one can easily perform the same contour integral as was done long ago for isotropic superconductors on a spherical FS [37], obtaining

$$\overline{\tilde{G}}^0_{\sigma\sigma'}(\tilde{\boldsymbol{r}} - \tilde{\boldsymbol{r}}', \pm\omega_n) = \alpha^3 \int \frac{d^3\tilde{\boldsymbol{k}}}{(2\pi)^3} e^{i\tilde{\boldsymbol{k}}\cdot(\tilde{\boldsymbol{r}}-\tilde{\boldsymbol{r}}')} \frac{\delta_{\sigma\sigma'}}{\pm i\omega_n - \frac{\tilde{\boldsymbol{k}}^2}{2\tilde{m}} + \mu_\sigma(\tilde{B}_3)} \tag{A.32}$$

$$= -\frac{\delta_{\sigma\sigma'}\tilde{m}\alpha^3}{2\pi|\tilde{\boldsymbol{r}} - \tilde{\boldsymbol{r}}'|} e^{\pm i\tilde{k}_F|\tilde{\boldsymbol{r}}-\tilde{\boldsymbol{r}}'|\mathrm{sgn}(\omega_n) - |\omega_n||\tilde{\boldsymbol{r}}-\tilde{\boldsymbol{r}}'|/\tilde{v}_F}, \tag{A.33}$$

where $\tilde{k}_F = k_F/\alpha$, $\tilde{v}_F = \alpha v_F$, and $\tilde{m}$ is given by Eq. (A.18). In deriving Eq. (A.33), it is easiest to first perform the angular integrals, and then to note that

$$\int_0^\infty \tilde{k}d\tilde{k}(e^{i\tilde{k}|\tilde{\boldsymbol{r}}-\tilde{\boldsymbol{r}}'|} - e^{-i\tilde{k}|\tilde{\boldsymbol{r}}-\tilde{\boldsymbol{r}}'|})\overline{\tilde{G}}^0_{\sigma\sigma'}(\tilde{\boldsymbol{k}}, \pm\omega_m) = \int_{-\infty}^\infty \tilde{k}d\tilde{k} e^{i\tilde{k}|\tilde{\boldsymbol{r}}-\tilde{\boldsymbol{r}}'|}\overline{\tilde{G}}^0_{\sigma\sigma'}(\tilde{\boldsymbol{k}}, \pm\omega_m) \tag{A.34}$$

$$= -\int_{-\infty}^\infty \tilde{k}d\tilde{k} e^{-i\tilde{k}|\tilde{\boldsymbol{r}}-\tilde{\boldsymbol{r}}'|}\overline{\tilde{G}}^0_{\sigma\sigma'}(\tilde{\boldsymbol{k}}, \pm\omega_m) \tag{A.35}$$

Then set $\tilde{k} = \tilde{k}_F + \tilde{k} - \tilde{k}_F$, let $\mu_\sigma(\tilde{B}_3) = \tilde{k}_F^2/(2\tilde{m})$, set $\xi_{\tilde{k}} = (\tilde{k} - \tilde{k}_F)\tilde{v}_F$, and neglect the term proportional to $\xi_{\tilde{k}}^2$. Then, if $\pm\omega_n > 0$, use Eq. (A.34), and close the contour in the upper half plane. If $\pm\omega_n < 0$, use Eq. (A.35), and close the contour in the lower half plane. Note that the sum over the ω_n is performed after the final gap equation is evaluated, so there is a single pole at $\xi_k = \pm i\omega_n$

in Eq. (A.32).

Equations (4.6) and (4.7) may be rewritten as

$$\begin{aligned}
\tilde{G}_{\sigma\sigma'}(\tilde{\boldsymbol{r}},\tilde{\boldsymbol{r}}',\omega_n) &= \tilde{G}^0_{\sigma\sigma}(\tilde{\boldsymbol{r}},\tilde{\boldsymbol{r}}',\omega_n)\delta_{\sigma\sigma'} - \alpha^{-6}\int d^3\tilde{\boldsymbol{\xi}}d^3\tilde{\boldsymbol{\xi}}'\sum_\rho \tilde{G}^0_{\sigma\sigma}(\tilde{\boldsymbol{r}},\tilde{\boldsymbol{\xi}}',\omega_n)\tilde{\Delta}_{\sigma\rho}(\tilde{\boldsymbol{\xi}}',\tilde{\boldsymbol{\xi}})\tilde{F}^\dagger_{\rho\sigma'}(\tilde{\boldsymbol{\xi}},\tilde{\boldsymbol{r}}',\omega_n), \\
\tilde{F}_{\sigma\sigma'}(\tilde{\boldsymbol{r}},\tilde{\boldsymbol{r}}',\omega_n) &= \alpha^{-6}\int d^3\tilde{\boldsymbol{\xi}}d^3\tilde{\boldsymbol{\xi}}'\sum_\rho \tilde{G}^0_{\sigma\sigma}(\tilde{\boldsymbol{r}},\tilde{\boldsymbol{\xi}},\omega_n)\tilde{\Delta}_{\sigma\rho}(\tilde{\boldsymbol{\xi}},\tilde{\boldsymbol{\xi}}')\tilde{G}_{\rho\sigma'}(\tilde{\boldsymbol{r}}',\tilde{\boldsymbol{\xi}}',-\omega_n),
\end{aligned} \tag{A.36}$$

where the two factors of α^{-3} arise from the KC transformations, since the volume element is rotationally invariant, and hence $d^3\boldsymbol{\xi} \to \alpha^{-3}(\overline{m}_1\overline{m}_2\overline{m}_3)^{-1/2}d^3\tilde{\boldsymbol{\xi}} = \alpha^{-3}d^3\tilde{\boldsymbol{\xi}}$.

In real space and imaginary time, the superconducting order parameter is defined by

$$\tilde{\Delta}_{\sigma\sigma'}(\tilde{\boldsymbol{r}},\tilde{\boldsymbol{r}}') = \tilde{V}(\tilde{\boldsymbol{r}}-\tilde{\boldsymbol{r}}')\tilde{F}_{\sigma\sigma'}(\tilde{\boldsymbol{r}},\tilde{\boldsymbol{r}}',0^+), \tag{A.37}$$

resulting in the gap equation in the transformed variables,

$$\begin{aligned}
\tilde{\Delta}_{\sigma\sigma'}(\tilde{\boldsymbol{r}},\tilde{\boldsymbol{r}}') &= \tilde{V}(\tilde{\boldsymbol{r}}-\tilde{\boldsymbol{r}}')\alpha^{-6}T\sum_{\omega_n}\sum_\rho\int d^3\tilde{\boldsymbol{\xi}}d^3\tilde{\boldsymbol{\xi}}'\tilde{G}^0_{\sigma\sigma}(\tilde{\boldsymbol{r}},\tilde{\boldsymbol{\xi}},\omega_n)\tilde{\Delta}_{\sigma\rho}(\tilde{\boldsymbol{\xi}},\tilde{\boldsymbol{\xi}}') \\
&\quad\times\tilde{G}_{\rho\sigma'}(\tilde{\boldsymbol{r}}',\tilde{\boldsymbol{\xi}}',-\omega_n).
\end{aligned} \tag{A.38}$$

Since the order parameter is obtained from the $\tilde{F}$ function, we have to include it to insure gauge invariance. Thus, we write

$$\tilde{\Delta}_{\sigma\sigma'}(\tilde{\boldsymbol{r}},\tilde{\boldsymbol{r}}') = \overline{\tilde{\Delta}}_{\sigma\sigma'}(\tilde{\boldsymbol{r}},\tilde{\boldsymbol{r}}')e^{i\tilde{e}[\Phi(\tilde{\mathrm{r}})+\Phi(\tilde{\mathrm{r}}')]}. \tag{A.39}$$

Using Eqs. (A.21), (A.23), and (A.39), and after dividing by the exponents in Eq. (A.39), we

obtain

$$\begin{aligned}\overline{\tilde{\Delta}}_{\sigma\sigma'}(\tilde{\boldsymbol{r}},\tilde{\boldsymbol{r}}') &= \tilde{V}(\tilde{\boldsymbol{r}}-\tilde{\boldsymbol{r}}')\alpha^{-6}T\sum_{\omega_n}\sum_{\rho}\int d^3\tilde{\boldsymbol{\xi}}d^3\tilde{\boldsymbol{\xi}}'\overline{\tilde{G}}^0_{\sigma\sigma}(\tilde{\boldsymbol{r}}-\tilde{\boldsymbol{\xi}},\omega_n)\\ &\quad\times e^{2i\tilde{e}\phi(\tilde{\boldsymbol{r}}',\tilde{\boldsymbol{\xi}}')}\overline{\tilde{\Delta}}_{\sigma\rho}(\tilde{\boldsymbol{\xi}},\tilde{\boldsymbol{\xi}}')\overline{\tilde{G}}_{\rho\sigma'}(\tilde{\boldsymbol{\xi}}',\tilde{\boldsymbol{r}}',-\omega_n).\end{aligned} \tag{A.40}$$

We then rewrite the order parameter and the full Green function in terms of their centers of mass and relative positions, obtaining

$$\begin{aligned}\overline{\tilde{\Delta}}_{\sigma\sigma'}\big[(\tilde{\boldsymbol{r}}+\tilde{\boldsymbol{r}}')/2,\tilde{\boldsymbol{r}}-\tilde{\boldsymbol{r}}'\big] &= \tilde{V}(\tilde{\boldsymbol{r}}-\tilde{\boldsymbol{r}}')\alpha^{-6}T\sum_{\omega_n}\sum_{\rho}\int d^3\tilde{\boldsymbol{\xi}}d^3\tilde{\boldsymbol{\xi}}'\overline{\tilde{G}}^0_{\sigma\sigma}(\tilde{\boldsymbol{r}}-\tilde{\boldsymbol{\xi}},\omega_n)\\ &\quad\times\exp\Big[2i\tilde{e}\int_{\tilde{\boldsymbol{r}}'}^{\tilde{\boldsymbol{\xi}}'}\tilde{\boldsymbol{A}}(\tilde{\boldsymbol{s}})\cdot d\tilde{\boldsymbol{s}}\Big]\overline{\tilde{\Delta}}_{\sigma\rho}\big[(\tilde{\boldsymbol{\xi}}+\tilde{\boldsymbol{\xi}}')/2,\tilde{\boldsymbol{\xi}}-\tilde{\boldsymbol{\xi}}'\big]\\ &\quad\times\overline{\tilde{G}}_{\rho\sigma'}\big[(\tilde{\boldsymbol{r}}'+\tilde{\boldsymbol{\xi}}')/2,\tilde{\boldsymbol{r}}'-\tilde{\boldsymbol{\xi}}',-\omega_n\big].\end{aligned} \tag{A.41}$$

Now, we let

$$\tilde{\boldsymbol{R}} = (\tilde{\boldsymbol{r}}+\tilde{\boldsymbol{r}}')/2 \tag{A.42}$$

be the center of mass of the unperturbed order parameter. Thus, we may rewrite

$$\begin{aligned}\overline{\tilde{\Delta}}_{\sigma\rho}\big[(\tilde{\boldsymbol{\xi}}+\tilde{\boldsymbol{\xi}}')/2,\tilde{\boldsymbol{\xi}}-\tilde{\boldsymbol{\xi}}'\big] &= \exp\Big(\big[(\tilde{\boldsymbol{\xi}}+\tilde{\boldsymbol{\xi}}')/2-\tilde{\boldsymbol{r}}''\big]\cdot\tilde{\boldsymbol{\nabla}}_{\tilde{\boldsymbol{R}}}\Big)\\ &\quad\times\overline{\tilde{\Delta}}_{\sigma\rho}(\tilde{\boldsymbol{R}},\tilde{\boldsymbol{\xi}}-\tilde{\boldsymbol{\xi}}')\Big|_{\tilde{\boldsymbol{r}}''=\tilde{\boldsymbol{R}}},\end{aligned} \tag{A.43}$$

$$\begin{aligned}\overline{\tilde{G}}_{\rho\sigma'}\big[(\tilde{\boldsymbol{r}}'+\tilde{\boldsymbol{\xi}}')/2,\tilde{\boldsymbol{r}}'-\tilde{\boldsymbol{\xi}}',-\omega_n\big] &= \exp\Big(\big[(\tilde{\boldsymbol{r}}'+\tilde{\boldsymbol{\xi}}')/2-\tilde{\boldsymbol{r}}'''\big]\cdot\tilde{\boldsymbol{\nabla}}_{\tilde{\boldsymbol{R}}}\Big)\\ &\quad\times\overline{\tilde{G}}_{\rho\sigma'}(\tilde{\boldsymbol{R}},\tilde{\boldsymbol{r}}'-\tilde{\boldsymbol{\xi}}',-\omega_n)\Big|_{\tilde{\boldsymbol{r}}'''=\tilde{\boldsymbol{R}}}.\end{aligned} \tag{A.44}$$

Note that these operations are just reformulations of the Taylor series expansions.

We then make the approximations that $\tilde{\boldsymbol{R}} = (\tilde{\boldsymbol{r}} + \tilde{\boldsymbol{r}}')/2 \approx \tilde{\boldsymbol{r}}'$ and $(\tilde{\boldsymbol{\xi}} + \tilde{\boldsymbol{\xi}}')/2 \approx \tilde{\boldsymbol{\xi}}'$, as the center of mass of the order parameter is close to the positions of either paired electron. Then

$$\begin{aligned} e^{2i\tilde{e}\phi(\tilde{\boldsymbol{r}}',\tilde{\boldsymbol{\xi}}')}\overline{\tilde{\Delta}}\big[(\tilde{\boldsymbol{\xi}}+\tilde{\boldsymbol{\xi}}')/2, \tilde{\boldsymbol{\xi}}-\tilde{\boldsymbol{\xi}}'\big] \quad &\approx \quad e^{2i\tilde{e}\phi(\tilde{\boldsymbol{r}}',\tilde{\boldsymbol{\xi}}')}e^{(\tilde{\boldsymbol{\xi}}'-\tilde{\boldsymbol{r}}')\cdot\tilde{\boldsymbol{\nabla}}_{\tilde{\boldsymbol{R}}}}\overline{\tilde{\Delta}}_{\sigma\rho}(\tilde{\boldsymbol{R}}, \tilde{\boldsymbol{\xi}}-\tilde{\boldsymbol{\xi}}') \\ \times\overline{\tilde{G}}_{\rho\sigma'}\big[(\tilde{\boldsymbol{r}}'+\tilde{\boldsymbol{\xi}}')/2, \tilde{\boldsymbol{r}}'-\tilde{\boldsymbol{\xi}}', -\omega_n\big] \quad &\quad \times e^{\frac{1}{2}(\tilde{\boldsymbol{\xi}}'-\tilde{\boldsymbol{r}}')\cdot\tilde{\boldsymbol{\nabla}}_{\tilde{\boldsymbol{R}}}}\overline{\tilde{G}}_{\rho\sigma'}(\tilde{\boldsymbol{R}}, \tilde{\boldsymbol{r}}'-\tilde{\boldsymbol{\xi}}', -\omega_n) \\ &= \quad e^{(\tilde{\boldsymbol{\xi}}'-\tilde{\boldsymbol{r}}')\cdot[\tilde{\boldsymbol{\nabla}}_{\tilde{\boldsymbol{R}}}-2i\tilde{e}\tilde{\boldsymbol{A}}(\tilde{\boldsymbol{R}})]}\overline{\tilde{\Delta}}_{\sigma\rho}(\tilde{\boldsymbol{R}}, \tilde{\boldsymbol{\xi}}-\tilde{\boldsymbol{\xi}}') \\ &\quad \times e^{\frac{1}{2}(\tilde{\boldsymbol{\xi}}'-\tilde{\boldsymbol{r}}')\cdot\tilde{\boldsymbol{\nabla}}_{\tilde{\boldsymbol{R}}}}\overline{\tilde{G}}_{\rho\sigma'}(\tilde{\boldsymbol{R}}, \tilde{\boldsymbol{r}}'-\tilde{\boldsymbol{\xi}}', -\omega_n), \quad \text{(A.45)} \end{aligned}$$

where we set $\tilde{\boldsymbol{r}}' \approx \tilde{\boldsymbol{R}}$ and $(\tilde{\boldsymbol{\xi}} + \tilde{\boldsymbol{\xi}}')/2 \approx \tilde{\boldsymbol{\xi}}'$, and made use of the Helfand-Werthamer procedure based upon a Feynman theorem [85]. Thus, the gap equation may be written as

$$\begin{aligned} \overline{\tilde{\Delta}}_{\sigma\sigma'}(\tilde{\boldsymbol{R}}, \tilde{\boldsymbol{r}}-\tilde{\boldsymbol{r}}') \;&=\; \tilde{V}(\tilde{\boldsymbol{r}}-\tilde{\boldsymbol{r}}')\alpha^{-6}T\sum_{\omega_n}\sum_{\rho}\int d^3\tilde{\boldsymbol{\xi}}d^3\tilde{\boldsymbol{\xi}}'\overline{\tilde{G}}^0_{\sigma\sigma}(\tilde{\boldsymbol{r}}-\tilde{\boldsymbol{\xi}}, \omega_n) \\ &\quad \times e^{i(\tilde{\boldsymbol{\xi}}'-\tilde{\boldsymbol{r}}')\cdot\tilde{\boldsymbol{\Pi}}(\tilde{\boldsymbol{R}})/\alpha}\overline{\tilde{\Delta}}_{\sigma\rho}(\tilde{\boldsymbol{R}}, \tilde{\boldsymbol{\xi}}-\tilde{\boldsymbol{\xi}}')e^{\frac{1}{2}(\tilde{\boldsymbol{\xi}}'-\tilde{\boldsymbol{r}}')\cdot\tilde{\boldsymbol{\nabla}}_{\tilde{\boldsymbol{R}}}} \\ &\quad \times\overline{\tilde{G}}_{\rho\sigma'}(\tilde{\boldsymbol{R}}, \tilde{\boldsymbol{r}}'-\tilde{\boldsymbol{\xi}}', -\omega_n), \qquad \text{(A.46)} \end{aligned}$$

where $\tilde{\boldsymbol{\Pi}}(\tilde{\boldsymbol{R}})$ is given by Eq. (4.10) of the text. We note that this expression differs slightly from that obtained previously, due to an unfortunate typo that interchanged G with G^0 [13]. To clarify that this result is correct, we put in the spin indices to preserve the matrix multiplications correctly. This change does not affect the behavior at H_{c2}, however.

We note that at (or just barely below) H_{c2} (or B_{c2}), the order parameter is vanishingly small, so it suffices to set

$$\overline{\tilde{G}}_{\rho\sigma'}(\tilde{\boldsymbol{R}}, \tilde{\boldsymbol{r}}'-\tilde{\boldsymbol{\xi}}', -\omega_n) \;\approx\; \overline{\tilde{G}}^0_{\rho\sigma'}(\tilde{\boldsymbol{r}}'-\tilde{\boldsymbol{\xi}}', -\omega_n), \qquad \text{(A.47)}$$

which is independent of $\tilde{\boldsymbol{R}}$, and hence the factor $e^{\frac{1}{2}(\tilde{\boldsymbol{\xi}}'-\tilde{\boldsymbol{r}}')\cdot\tilde{\boldsymbol{\nabla}}_{\tilde{\boldsymbol{R}}}}$ can be set equal to unity. We thus

have the equation in real space for the calculation of B_{c2},

$$\begin{aligned}\overline{\tilde{\Delta}}_{\sigma\sigma'}(\tilde{\boldsymbol{R}},\tilde{\boldsymbol{r}}-\tilde{\boldsymbol{r}}') &= \tilde{V}(\tilde{\boldsymbol{r}}-\tilde{\boldsymbol{r}}')\alpha^{-6}T\sum_{\omega_n}\int d^3\tilde{\boldsymbol{\xi}}d^3\tilde{\boldsymbol{\xi}}'\overline{\tilde{G}}^0_{\sigma\sigma}(\tilde{\boldsymbol{r}}-\tilde{\boldsymbol{\xi}},\omega_n)\\ &\quad\times e^{i(\tilde{\boldsymbol{\xi}}'-\tilde{\boldsymbol{r}}')\cdot\tilde{\boldsymbol{\Pi}}(\tilde{\boldsymbol{R}})/\alpha}\overline{\tilde{\Delta}}_{\sigma\sigma'}(\tilde{\boldsymbol{R}},\tilde{\boldsymbol{\xi}}-\tilde{\boldsymbol{\xi}}')\overline{\tilde{G}}^0_{\sigma'\sigma'}(\tilde{\boldsymbol{r}}'-\tilde{\boldsymbol{\xi}}',-\omega_n). \qquad \text{(A.48)}\end{aligned}$$

We remark that the pairing interaction is best defined in momentum space, so we have to transform this equation to the KC-transformed momentum space, which will allow us to properly transform the pairing interaction. Hence, we shall include enough intermediate steps to demonstrate the correct α dependence of the KC-transformed gap equation.

In order to Fourier transform the right-hand side of Eq. (A.48), we first let $\tilde{\boldsymbol{\xi}} \to \tilde{\boldsymbol{\xi}}+\tilde{\boldsymbol{r}}$ and $\tilde{\boldsymbol{\xi}}' \to \tilde{\boldsymbol{\xi}}'+\tilde{\boldsymbol{r}}'$. This means we only need to Fourier transform $\overline{\tilde{\Delta}}_{\sigma\rho}(\tilde{\boldsymbol{R}},\tilde{\boldsymbol{\xi}}+\tilde{\boldsymbol{r}}-\tilde{\boldsymbol{\xi}}'-\tilde{\boldsymbol{r}}')$ to obtain all of the $\tilde{\boldsymbol{r}}-\tilde{\boldsymbol{r}}'$ terms in the exponent for comparison with that in Eq. (A.49). In writing the Fourier transform, we use the same transformation $d^3\boldsymbol{k} \to \alpha^3 d^3\tilde{\boldsymbol{k}}$ as in Eq. (A.14). We then obtain

$$\begin{aligned}\overline{\tilde{\Delta}}_{\sigma\sigma'}(\tilde{\boldsymbol{R}},\tilde{\boldsymbol{k}}) &= \alpha^{-3}\int\frac{d^3\tilde{\boldsymbol{k}}'}{(2\pi)^3}e^{i\tilde{\boldsymbol{k}}'\cdot(\tilde{\boldsymbol{\xi}}-\tilde{\boldsymbol{\xi}}')}T\sum_{\omega_n}\tilde{V}(\tilde{\boldsymbol{k}}-\tilde{\boldsymbol{k}}')\\ &\quad\times\int d^3\tilde{\boldsymbol{\xi}}d^3\tilde{\boldsymbol{\xi}}'\overline{\tilde{G}}^0_{\sigma\sigma}(\tilde{\boldsymbol{\xi}}',\omega_n)e^{i\tilde{\boldsymbol{\xi}}\cdot\tilde{\boldsymbol{\Pi}}(\tilde{\boldsymbol{R}})/\alpha}\overline{\tilde{\Delta}}_{\sigma\sigma'}(\tilde{\boldsymbol{R}},\tilde{\boldsymbol{k}}')\overline{\tilde{G}}^0_{\sigma'\sigma'}(\tilde{\boldsymbol{\xi}},-\omega_n), \qquad \text{(A.49)}\end{aligned}$$

where we interchanged $\tilde{\boldsymbol{\xi}}$ and $\tilde{\boldsymbol{\xi}}'$ for convenience, and we assumed the sample to exhibit inversion symmetry in the absence of a magnetic field.

We now need to write the transformed interaction $\tilde{V}(\tilde{\boldsymbol{k}}-\tilde{\boldsymbol{k}}')$ explicitly. We first note that the relevant part of an untransformed interaction of the form $V_0[(\hat{\boldsymbol{k}}-\hat{\boldsymbol{k}}')^2-2] = -2V_0\hat{\boldsymbol{k}}\cdot\hat{\boldsymbol{k}}'$, is rotationally invariant, as studied previously [13]. However, if we break this symmetry, and only allow the pairing to be in one or two dimensions, we could have the relevant bare interaction be as described in the text, $V(\hat{\boldsymbol{k}},\hat{\boldsymbol{k}}') = V_0\hat{k}_3\hat{k}'_3$, where $\hat{k}_3$ is given by Eq. (4.4) with $i=3$. Then, making

the KC transformations, we obtain

$$\tilde{V}(\hat{\tilde{\boldsymbol{k}}},\hat{\tilde{\boldsymbol{k}}}') \;=\; 3V_0(\hat{\tilde{k}}_3\cos\theta' - \hat{\tilde{k}}_2\sin\theta')(\hat{\tilde{k}}'_3\cos\theta' - \hat{\tilde{k}}'_2\sin\theta'), \tag{A.50}$$

This leads to

$$\begin{aligned}\overline{\tilde{\Delta}}_{\sigma\sigma'}(\tilde{\boldsymbol{R}},\tilde{\boldsymbol{k}}) \;&=\; \alpha^{-3}\int\frac{d^3\tilde{\boldsymbol{k}}'}{(2\pi)^3}e^{i\tilde{\boldsymbol{k}}'\cdot(\tilde{\boldsymbol{\xi}}-\tilde{\boldsymbol{\xi}}')}\\ &\quad\times T\sum_{\omega_n}3V_0(\hat{\tilde{k}}_3\cos\theta' - \hat{\tilde{k}}_2\sin\theta')(\hat{\tilde{k}}'_3\cos\theta' - \hat{\tilde{k}}'_2\sin\theta')\\ &\quad\times\int d^3\tilde{\boldsymbol{\xi}}d^3\tilde{\boldsymbol{\xi}}'\overline{\tilde{G}}^0_{\sigma\sigma}(\tilde{\boldsymbol{\xi}}',\omega_n)e^{i\tilde{\boldsymbol{\xi}}\cdot\tilde{\boldsymbol{\Pi}}(\tilde{\boldsymbol{R}})/\alpha}\overline{\tilde{\Delta}}_{\sigma\sigma'}(\tilde{\boldsymbol{R}},\tilde{\boldsymbol{k}}')\overline{\tilde{G}}^0_{\sigma'\sigma'}(\tilde{\boldsymbol{\xi}},-\omega_n),\end{aligned} \tag{A.51}$$

We then may write

$$\overline{\tilde{\Delta}}_{\sigma\sigma'}(\tilde{\boldsymbol{R}},\tilde{\boldsymbol{k}}) \;=\; \overline{\tilde{\Delta}}_{\sigma\sigma'}(\tilde{\boldsymbol{R}})(\hat{\tilde{k}}_3\cos\theta' - \hat{\tilde{k}}_2\sin\theta'), \tag{A.52}$$

leading to

$$\begin{aligned}\overline{\tilde{\Delta}}_{\sigma\sigma'}(\tilde{\boldsymbol{R}}) \;&=\; \alpha^{-3}3V_0\int\frac{d^3\tilde{\boldsymbol{k}}'}{(2\pi)^3}e^{i\tilde{\boldsymbol{k}}'\cdot(\tilde{\boldsymbol{\xi}}-\tilde{\boldsymbol{\xi}}')}(\hat{\tilde{k}}'_3\cos\theta' - \hat{\tilde{k}}'_2\sin\theta')^2\\ &\quad\times T\sum_{\omega_n}\int d^3\tilde{\boldsymbol{\xi}}d^3\tilde{\boldsymbol{\xi}}'\overline{\tilde{G}}^0_{\sigma\sigma}(\tilde{\boldsymbol{\xi}}',\omega_n)e^{i\tilde{\boldsymbol{\xi}}\cdot\tilde{\boldsymbol{\Pi}}(\tilde{\boldsymbol{R}})/\alpha}\overline{\tilde{\Delta}}_{\sigma\sigma'}(\tilde{\boldsymbol{R}})\overline{\tilde{G}}^0_{\sigma'\sigma'}(\tilde{\boldsymbol{\xi}},-\omega_n).\end{aligned} \tag{A.53}$$

Then, we invoke the mild approximation used previously [13],

$$\int d^3\tilde{\boldsymbol{k}}'e^{i\tilde{\boldsymbol{k}}'\cdot(\tilde{\boldsymbol{\xi}}-\tilde{\boldsymbol{\xi}}')}\hat{\tilde{k}}'_\mu\hat{\tilde{k}}'_\nu \;=\; (2\pi)^3\hat{\tilde{\xi}}_\mu\hat{\tilde{\xi}}_\nu\delta^3(\tilde{\boldsymbol{\xi}}-\tilde{\boldsymbol{\xi}}'), \tag{A.54}$$

which also works with the transformed variables. This leads to

$$\begin{aligned}\overline{\tilde{\Delta}}_{\sigma\sigma'}(\tilde{\boldsymbol{R}}) &= \alpha^{-3}3V_0\int d^3\tilde{\boldsymbol{\xi}}'(\hat{\tilde{\xi}}'_3\cos\theta' - \hat{\tilde{\xi}}'_2\sin\theta')^2 \\ &\quad\times T\sum_{\omega_n}\overline{\tilde{G}}^0_{\sigma\sigma}(\tilde{\boldsymbol{\xi}}',\omega_n)e^{i\tilde{\boldsymbol{\xi}}'\cdot\tilde{\boldsymbol{\Pi}}(\tilde{\boldsymbol{R}})/\alpha}\overline{\tilde{\Delta}}_{\sigma\sigma'}(\tilde{\boldsymbol{R}})\overline{\tilde{G}}^0_{\sigma'\sigma'}(\tilde{\boldsymbol{\xi}}',-\omega_n). \qquad \text{(A.55)}\end{aligned}$$

We then let $\tilde{\boldsymbol{\xi}}' = \alpha\tilde{\boldsymbol{\xi}}$, and obtain

$$\begin{aligned}\overline{\tilde{\Delta}}_{\sigma\sigma'}(\tilde{\boldsymbol{R}}) &= \frac{m^2 3V_0}{(2\pi)^2}\int\frac{d^3\tilde{\boldsymbol{\xi}}}{\tilde{\xi}^2}(\hat{\tilde{\xi}}_3\cos\theta' - \hat{\tilde{\xi}}_2\sin\theta')^2 \\ &\quad\times T\sum_{\omega_n}e^{-2|\omega_n|\tilde{\xi}/v_F}e^{i\tilde{\boldsymbol{\xi}}\cdot\tilde{\boldsymbol{\Pi}}(\tilde{\boldsymbol{R}})}\overline{\tilde{\Delta}}_{\sigma\sigma'}(\tilde{\boldsymbol{R}}), \qquad \text{(A.56)}\end{aligned}$$

which is exactly as for an isotropic Fermi surface, except for the transformed p-wave polar/CBS state interaction and the modification of $\tilde{\boldsymbol{\Pi}}(\tilde{\boldsymbol{R}})$ due to α in Eq. (4.10). Note that in deriving Eq. (A.56), we used Eq. (A.33) with $\tilde{\boldsymbol{r}} - \tilde{\boldsymbol{r}}' \to \alpha\tilde{\boldsymbol{\xi}}$. Since this form appears to describe the interaction in real space rather than in the correct momentum space, we rewrite this equation including the $\hat{\tilde{\boldsymbol{k}}}$ or $\hat{\tilde{\boldsymbol{k}}}'$ dependence of the order parameter, and also include the pairing interaction. $N(0)$, the single-spin density of states, can also be included in the expression by letting $\tilde{\boldsymbol{\xi}} \to \tilde{\boldsymbol{k}}' v_F$. We then obtain the expression in terms of the general transformed interaction $\tilde{V}(\hat{\tilde{\boldsymbol{k}}},\hat{\tilde{\boldsymbol{k}}}')$,

$$\begin{aligned}\overline{\tilde{\Delta}}(\tilde{\boldsymbol{R}},\hat{\tilde{\boldsymbol{k}}}) &= T\frac{N(0)}{2}\sum_{\omega_n}\int d\Omega_{\tilde{\boldsymbol{k}}'}\tilde{V}(\hat{\tilde{\boldsymbol{k}}},\hat{\tilde{\boldsymbol{k}}}')\int_0^\infty d\xi_{\tilde{\boldsymbol{k}}'}e^{-2\xi_{\tilde{\boldsymbol{k}}'}|\omega_n|}e^{-i\xi_{\tilde{\boldsymbol{k}}'}v_F\hat{\tilde{\boldsymbol{k}}}'\cdot\tilde{\boldsymbol{\Pi}}(\tilde{\boldsymbol{R}})} \\ &\quad\times\overline{\tilde{\Delta}}(\tilde{\boldsymbol{R}},\hat{\tilde{\boldsymbol{k}}}'), \qquad \text{(A.57)}\end{aligned}$$

where $\tilde{V}(\hat{\tilde{\boldsymbol{k}}},\hat{\tilde{\boldsymbol{k}}})$ for the polar state with completely broken symmetry is given by Eq. (A.50), but can be generalized to any anisotropic form. Of course, for non-parallel spin states, the Zeeman energies leading to Pauli pair breaking and $\boldsymbol{B}$ at an arbitrary direction must also be included and properly transformed for an ellipsoidal FS.

We note that $\tilde{\boldsymbol{B}} = \hat{\boldsymbol{z}}\tilde{B}_3$. Neglecting defects and surface pinning effects, it is valid just below B_{c2} to assume straight vortices along $\hat{\tilde{\boldsymbol{z}}}$. For a spatially constant (single-ferromagnetic domain) $\tilde{B}_3$, the $\tilde{\boldsymbol{A}}(\tilde{\boldsymbol{R}})$ can then be chosen to be either $-\tilde{B}_3\hat{\tilde{\boldsymbol{X}}}\tilde{Y}$ or $\tilde{B}_3\hat{\tilde{\boldsymbol{Y}}}\tilde{X}$, mapping the eigenvalue problem onto that of a one-dimensional (1D) harmonic oscillator.

In order to calculate B_{c2}, we expand $\overline{\tilde{\Delta}}(\tilde{\boldsymbol{R}}, \hat{\tilde{\boldsymbol{k}}})$ in terms of the $\hat{\tilde{\boldsymbol{k}}}$ factor in $\tilde{V}(\hat{\tilde{\boldsymbol{k}}}, \hat{\tilde{\boldsymbol{k}}}')$ and the $\tilde{\boldsymbol{R}}$ part in terms of the 1D harmonic oscillator eigenfunctions [13, 85],

$$\overline{\tilde{\Delta}}(\tilde{\boldsymbol{R}}, \hat{\tilde{\boldsymbol{k}}}) \;=\; (\hat{\tilde{\boldsymbol{k}}}\cos\theta' - \hat{\tilde{\boldsymbol{k}}}\sin\theta')\sum_{n=0}^{\infty} a_n |n(\tilde{\boldsymbol{R}})\rangle. \tag{A.58}$$

The procedure is precisely the same as for the polar, SK and polar/CBS states [13, 14], with the only differences being the θ' of the transformed interaction and the modification of the the operator from $\boldsymbol{\Pi}(\boldsymbol{R}) \rightarrow \tilde{\boldsymbol{\Pi}}(\tilde{\boldsymbol{R}})$, where $\tilde{\boldsymbol{\Pi}}(\tilde{\boldsymbol{R}})$ is given by Eq. (4.10) of the text. As in those previous calculations [85, 13, 14], one requires the matrix elements

$$M_{n',n} \;=\; \langle a_{n'}(\tilde{\boldsymbol{R}})| e^{i\xi_{\tilde{\boldsymbol{k}}'} v_F \hat{\tilde{\boldsymbol{k}}}'\cdot\tilde{\boldsymbol{\Pi}}(\tilde{\boldsymbol{R}})} |a_n(\tilde{\boldsymbol{R}})\rangle, \tag{A.59}$$

which must then be integrated over the angles arising from $\hat{\tilde{\boldsymbol{k}}}' \cdot \tilde{\boldsymbol{R}}$. We write

$$\tilde{\Pi}_{\pm}(\tilde{\boldsymbol{R}}) \;=\; \frac{1}{\sqrt{2}}[\tilde{\Pi}_x(\tilde{\boldsymbol{R}}) \pm i\tilde{\Pi}_y(\tilde{\boldsymbol{R}})], \tag{A.60}$$

and since $\tilde{\boldsymbol{B}} = \hat{\tilde{\boldsymbol{z}}}\tilde{B}_3$ is along the transformed $\tilde{z}$ axis, we may write

$$\begin{aligned} e^{i\xi_{\tilde{\boldsymbol{k}}'} v_F \hat{\tilde{\boldsymbol{k}}}'\cdot\tilde{\boldsymbol{\Pi}}(\tilde{\boldsymbol{R}})} \;=\; & e^{-\frac{1}{2}eB\alpha v_F^2 \xi_{\tilde{\boldsymbol{k}}'}^2} e^{\frac{i}{\sqrt{2}} v_F \xi_{\tilde{\boldsymbol{k}}'} \sin\theta_{\tilde{\boldsymbol{k}}'} e^{-i\phi_{\tilde{\boldsymbol{k}}'}} \tilde{\Pi}_+(\tilde{\boldsymbol{R}})} e^{\frac{i}{\sqrt{2}} v_F \xi_{\tilde{\boldsymbol{k}}'} \sin\theta_{\tilde{\boldsymbol{k}}'} e^{+i\phi_{\tilde{\boldsymbol{k}}'}} \tilde{\Pi}_-(\tilde{\boldsymbol{R}})} \\ & \times e^{i v_F \xi_{\tilde{\boldsymbol{k}}'} \cos\theta_{\tilde{\boldsymbol{k}}'} \tilde{\Pi}_z(\tilde{\boldsymbol{R}})}. \end{aligned} \tag{A.61}$$

For straight vortices, $\tilde{\Pi}_z(\tilde{\boldsymbol{R}})|n(\tilde{\boldsymbol{R}})\rangle = 0$. Hence, we may drop the right factor containing $\tilde{\Pi}_z(\tilde{\boldsymbol{R}})$. Note that for this operator ordering, $\tilde{\Pi}_-^n(\tilde{\boldsymbol{R}})|n(\tilde{\boldsymbol{R}})\rangle = 0$, etc. It is then easiest to expand the exponentials of the operators in the usual power series, and obtain the matrix elements

$$M_{n',n}^{p',p} = \langle n'(\tilde{\boldsymbol{R}})|\tilde{\Pi}_+^{p'}(\tilde{\boldsymbol{R}})\tilde{\Pi}_-^{p}(\tilde{\boldsymbol{R}})|n(\tilde{\boldsymbol{R}})\rangle. \tag{A.62}$$

Then, one evaluates the integrals over $\theta_{\tilde{\boldsymbol{k}}'}$, $\phi_{\tilde{\boldsymbol{k}}'}$, and $\xi_{\tilde{\boldsymbol{k}}'}$ to obtain the relevant recursion relation for the a_n coefficients.

APPENDIX B: DERIVATION OF DOUBLE ELLIPSOIDAL FERMI SURFACE MODEL AND SPECIFIC HEAT IN A FIELD

We first calculate an expression for the field dependent chemical potential, $\mu_\sigma(\boldsymbol{B})$, on the σ Fermi surface, by calculating the particle density in the absence of a field, $n_\sigma(0)$, and in a field, $n_\sigma(\boldsymbol{B})$. As in the Born-Sommerfeld approximation, we expect $\sum_\sigma n_\sigma(0) = \sum_\sigma n_\sigma(\boldsymbol{B})$, or the total particle density for both spin-split Fermi surfaces to be independent of the external magnetic induction. In our formulation, we set $T \to 0$.

We begin with the Hamiltonian, $\mathcal{H}$, of our system

$$\mathcal{H} = \sum_{j\sigma} \left[\frac{1}{2m_{j\sigma}(\boldsymbol{B})} \left(k_j - eA_j\right)^2 - \mu_\sigma(0) + g\mu_B \boldsymbol{\sigma} \cdot \boldsymbol{B}/2 \right], \tag{B.1}$$

where $\mu_\sigma(0) = \mu(0) - \sigma I/2$. We apply the combined anisotropic scale, rotation, and isotropic scale KC transformations

$$x_\mu = \frac{1}{\alpha_\sigma \sqrt{\overline{m}_{\sigma,\mu}}} \sum_{\nu=1}^{3} \lambda_{\sigma,\nu\mu} \tilde{x}_{\sigma,\nu}, \tag{B.2}$$

$$\frac{\partial}{\partial x_\mu} = \alpha_\sigma \sqrt{\overline{m}_{\sigma,\mu}} \sum_{\nu=1}^{3} \lambda_{\sigma,\nu\mu} \frac{\partial}{\partial \tilde{x}_{\sigma,\nu}}, \tag{B.3}$$

$$B_\mu = \frac{1}{\alpha_\sigma \sqrt{\overline{m}_{\sigma,\mu}}} \sum_{\nu=1}^{3} \lambda_{\sigma,\nu\mu} \tilde{B}_{\sigma,\nu}, \tag{B.4}$$

$$H_\mu = \frac{1}{\alpha_\sigma \sqrt{\overline{m}_{\sigma,\mu}}} \sum_{\nu=1}^{3} \lambda_{\sigma,\nu\mu} \tilde{H}_{\sigma,\nu}, \tag{B.5}$$

$$A_\mu = \sqrt{\overline{m}_{\sigma,\mu}} \sum_{\nu=1}^{3} \lambda_{\sigma,\nu\mu} \tilde{A}_{\sigma,\nu}, \tag{B.6}$$

where

$$\lambda_\sigma = \begin{pmatrix} -\sin\phi'_\sigma & -\cos\phi'_\sigma & 0 \\ \cos\theta'_\sigma\cos\phi'_\sigma & \cos\theta'_\sigma\sin\phi'_\sigma & -\sin\theta'_\sigma \\ \sin\theta'_\sigma\cos\phi'_\sigma & \sin\theta'_\sigma\sin\phi'_\sigma & \cos\theta'_\sigma \end{pmatrix}, \tag{B.7}$$

and the transformed angles are given by

$$\cos\theta'_\sigma = \frac{\sqrt{\overline{m}_{3\sigma}}\cos\theta}{\alpha_\sigma(\theta,\phi)}, \tag{B.8}$$

$$\sin\theta'_\sigma = \frac{\overline{\alpha}_\sigma(\phi)\sin\theta}{\alpha_\sigma(\theta,\phi)}, \tag{B.9}$$

$$\cos\phi'_\sigma = \frac{\sqrt{\overline{m}_{1\sigma}}\cos\phi}{\overline{\alpha}_\sigma(\phi)}, \tag{B.10}$$

$$\sin\phi'_\sigma = \frac{\sqrt{\overline{m}_{2\sigma}}\sin\phi}{\overline{\alpha}_\sigma(\phi)}, \tag{B.11}$$

where $\overline{\alpha}_\sigma(\phi) = \alpha_\sigma(\pi/2,\phi)$. We also obtain

$$\epsilon_\sigma(k_{\sigma,\parallel}, n+1/2) = \frac{k^2_{\sigma,\parallel}}{2m_{\sigma,\parallel}} + \omega_{\sigma,\perp}(n+1/2), \tag{B.12}$$

where $\omega_{\sigma,\perp} = \frac{eB}{m_{\sigma,\perp}(\boldsymbol{B})}$, $m_{\sigma,\perp}(\boldsymbol{B}) = \frac{m_\sigma(\boldsymbol{B})}{\alpha_\sigma(\theta,\phi)}$, and $m_{\sigma,\parallel} = m_\sigma\alpha^2_\sigma(\theta,\phi)$ Although obtaining the effective mass parallel to the field with the KC-transformations is non-trivial, we have shown that our results are consistent for any choice of $\boldsymbol{A}$ in all three planes, and they provide the correct $\boldsymbol{B} \to 0$ limit.

For the particle density in zero magnetic induction, we have

$$n_\sigma(0) = \int \frac{d^3k'_\sigma}{(2\pi)^3}\Theta[\mu_\sigma(0) - \varepsilon_\sigma\left(k'_\sigma\right)], \tag{B.13}$$

where we have used the first KC scale transformation $k_i \rightarrow \sqrt{\overline{m}_{i\sigma}(0)}k'_{i\sigma}$, which is different for each FS, so we get

$$n_\sigma(0) = c_\sigma \int_0^{\mu_\sigma(0)} E_\sigma^{1/2} dE_\sigma = \frac{2m_\sigma^{3/2}(0)\mu_\sigma^{3/2}(0)}{3\pi^2\sqrt{2}}, \tag{B.14}$$

where $c_\sigma = \frac{m_\sigma^{3/2}(0)}{\pi^2\sqrt{2}}$,

$$\varepsilon_\sigma\left(k\right) = \sum_{j=1}^{3} \frac{k_{j\sigma}^2}{2m_{j\sigma}(0)}, \tag{B.15}$$

$$\varepsilon_\sigma\left(k'_\sigma\right) = E_\sigma = \sum_{j=1}^{3} \frac{k_{j\sigma}'^2}{2m_\sigma(0)}, \tag{B.16}$$

and $m_\sigma(0) = [m_{1\sigma}(0)m_{2\sigma}(0)m_{3\sigma}(0)]^{1/3}$, and $m_{j\sigma}(0)$ are the single particle effective masses on each FS in zero induction. We sum over spin to obtain the total particle density for $\boldsymbol{B} = 0$,

$$\sum_\sigma n_\sigma(0) = \frac{2}{3\pi^2\sqrt{2}} \sum_\sigma \Pi_\sigma^{3/2}\left(0\right). \tag{B.17}$$

Now, in the presence of an induction,

$$n_\sigma(\boldsymbol{B}) = \frac{eB}{2\pi}\int \frac{dk_{\sigma,\|}}{2\pi} \times \sum_{n=0}^{\infty} \frac{1}{e^{\beta\left[k^2_{\sigma,\|}/2m_{\sigma,\|}(\boldsymbol{B})+\omega_{\sigma,\perp}(n+1/2)-\mu_\sigma(\boldsymbol{B})\right]}+1}, \tag{B.18}$$

where we have applied the KC-transformations [44, 33] on each ferromagnetically split Fermi surface to obtain $\omega_{\sigma,\perp} = \frac{eB}{m_{\sigma,\perp}(\boldsymbol{B})}$, $m_{\sigma,\|}(\boldsymbol{B}) = m_\sigma(\boldsymbol{B})\alpha^2_\sigma(\theta,\phi)$, which has been checked for consistency by diagonalizing the Hamiltonian with $\boldsymbol{B}$ chosen to lie in the xy, yz, and xz planes. To obtain $m_{\sigma,\perp}(\boldsymbol{B}) = \frac{m_\sigma(\boldsymbol{B})}{\alpha_\sigma(\theta,\phi)}$ from the KC transformations is not trivial, but we will deduce this result from the $B \to 0$ limit of $n_\sigma(\boldsymbol{B})$. For the time being, we will consider it to be an undetermined expression for each FS. We now obtain the expression for the particle density in a magnetic induction

$$\begin{aligned} n_\sigma(\boldsymbol{B}) &= \frac{eB}{2\pi}\frac{\sqrt{m_{\sigma,\|}(\boldsymbol{B})}}{\pi\sqrt{2}} \\ &\times \int E_\sigma^{-1/2} dE_\sigma \int_0^\infty dx \frac{1}{e^{\beta\left[E+\omega_{\sigma,\perp}x-\mu_\sigma(\boldsymbol{B})\right]}+1} \\ &\times \left(1+2\sum_{s=0}^{\infty}\cos(2\pi s x)\right), \end{aligned} \tag{B.19}$$

where we have used the Poisson summation formula

$$\sum_{n=0}^{\infty} f(n+1/2) = \int_0^\infty dx f(x)\left(1+2\sum_{s=0}^{\infty}(-1)^s\cos\left(2\pi s x\right)\right), \tag{B.20}$$

and have made the change of variables $E_\sigma = \frac{k^2_{\sigma,\|}}{2m_{\sigma,\|}(\boldsymbol{B})}$.

We calculate the non-oscillatory, $n_\sigma^{(1)}(\boldsymbol{B})$, and oscillatory, $n_\sigma^{(2)}(\boldsymbol{B})$, terms separately.

We have

$$\begin{aligned} n_\sigma^{(1)}(\boldsymbol{B}) &= \frac{eB}{2\pi}\frac{\sqrt{m_{\sigma,\|}(\boldsymbol{B})}}{\pi\sqrt{2}}\frac{1}{\omega_{\sigma,\perp}}\int E_\sigma^{-1/2}dE_\sigma \\ &\quad\times\int_0^\infty dy_\sigma \frac{1}{e^{\beta[E_\sigma+y_\sigma-\mu_\sigma(\boldsymbol{B})]}+1}, \end{aligned} \tag{B.21}$$

which upon taking the zero temperature limit, $T\to 0^+$, becomes

$$\begin{aligned} n_\sigma^{(1)}(\boldsymbol{B}) &= \frac{eB}{2\pi\omega_{\sigma,\perp}}\frac{\sqrt{m_{\sigma,\|}(\boldsymbol{B})}}{\pi\sqrt{2}} \\ &\quad\times\int_0^{\mu_\sigma(\boldsymbol{B})} E_\sigma^{-1/2}dE_\sigma\int_0^{\mu_\sigma(\boldsymbol{B})-E_\sigma} dy \\ &= \frac{2\sqrt{m_{\sigma,\|}(\boldsymbol{B})}m_{\sigma,\perp}(\boldsymbol{B})\mu_\sigma^{3/2}(\boldsymbol{B})}{3\pi^2\sqrt{2}}, \end{aligned} \tag{B.22}$$

where we have used the change of variables $y_\sigma=\omega_{\sigma,\perp}x$. It is important to note that the exponential term in Eq.(B.21) becomes a theta-function when taking the zero temperature limit.

Now we evaluate the oscillatory term, $n_\sigma^{(2)}(B)$, for which we have

$$\begin{aligned} n_\sigma^{(2)}(\boldsymbol{B}) &= \frac{eB}{2\pi\omega_{\sigma,\perp}}\frac{\sqrt{m_{\sigma,\|}(\boldsymbol{B})}}{\pi\sqrt{2}}\int_0^\infty dy_\sigma \\ &\quad\left(\int_0^\infty E_\sigma^{-1/2}dE_\sigma\frac{1}{e^{\beta[E_\sigma+y_\sigma-\mu_\sigma(\boldsymbol{B})]}+1}\right) \\ &\quad\times 2\sum_{s=1}^\infty(-1)^s\cos(2\pi s y_\sigma/\omega_{\sigma,\perp}). \end{aligned} \tag{B.23}$$

We define

$$f(y_\sigma) = \int_0^\infty E_\sigma^{-1/2} dE_\sigma \frac{1}{e^{\beta[E_\sigma + y_\sigma - \mu_\sigma(\boldsymbol{B})]} + 1}, \tag{B.24}$$

which then leads to

$$\begin{aligned} n_\sigma^{(2)}(\boldsymbol{B}) &= \frac{eB}{\pi\omega_{\sigma,\perp}} \frac{\sqrt{m_{\sigma,\parallel}(\boldsymbol{B})}}{\pi\sqrt{2}} \sum_{s=1}^{\infty} (-1)^s \\ &\quad \times \int_0^\infty dy_\sigma f(y_\sigma) \cos(2\pi s y_\sigma)/\omega_{\sigma,\perp}). \end{aligned} \tag{B.25}$$

We now evaluate the remaining integral by parts to arbitrary order and obtain

$$\begin{aligned} &\int_0^\infty dy_\sigma f(y_\sigma) \cos(2\pi s y_\sigma/\omega_{\sigma,\perp}) = \\ &\sum_{n=0}^{\infty} (-1)^{n+1} \left(\frac{\omega_{\sigma,\perp}}{2\pi s}\right)^{2n+2} f^{(2n+1)}(0), \end{aligned} \tag{B.26}$$

where $f^{(2n+1)}(0) = \frac{-(4n-1)!!}{2^{(2n)}\mu_\sigma^{(2n+1/2)}(\boldsymbol{B})}$, which is obtained from Eq.(B.24) by letting $T \to 0^+$, or $\beta \to +\infty$, so that the integration becomes

$$f(y_\sigma) = \int_0^{\mu_\sigma(\boldsymbol{B}) - y_\sigma} E_\sigma^{-1/2} dE_\sigma = 2\sqrt{\mu_\sigma(\boldsymbol{B}) - y_\sigma}, \tag{B.27}$$

and subsequently taking the $(2n+1)$th derivative and evaluating the expression at $y_\sigma = 0$. Substituting Eq.(B.26) into Eq.(B.25), we obtain

$$n_\sigma^{(2)}(\boldsymbol{B}) = \frac{2\sqrt{m_{\sigma,\parallel}(\boldsymbol{B})}m_{\sigma,\perp}(\boldsymbol{B})\mu_\sigma^{3/2}(\boldsymbol{B})}{\pi^2\sqrt{2}} \times \sum_{n=0}^{\infty}\frac{1}{3}a_n\left(\frac{eB\alpha_\sigma(\theta,\phi)}{m_\sigma(\boldsymbol{B})\mu_\sigma(\boldsymbol{B})}\right)^{2n+2}. \quad \text{(B.28)}$$

where $a_n = 3(-1)^{n+1}(2-2^{-2n})\zeta(2n+2)\frac{(4n-1)!!}{(4\pi)^{2n+2}}$, we have used $\sum_{s=1}^{\infty}(-1)^{s-1}\frac{1}{s^{2n+2}} = (1-2^{1-(2n+2)})\zeta(2n+2)$. We now take the limit as the magnetic induction tends to zero in the expression for the field-dependent particle density, $\sum_\sigma(n_\sigma^{(1)}(0)+n_\sigma^{(2)}(0))$ and equate this limit to the zero field particle density, $\sum_\sigma n_\sigma(0)$, from which we obtain the self consistent expression for the effective mass parallel to the magnetic induction, $\sqrt{m_{\sigma,\parallel}(\boldsymbol{B})}m_{\sigma,\perp}(\boldsymbol{B}) = m_\sigma^{3/2}(\boldsymbol{B})$. We have also diagonalized our Hamiltonian to order B^2 in all three crystallographic planes (i.e. ab, ac, and bc) confirming this result, and have obtained $m_{\parallel\sigma}(\boldsymbol{B}) = \alpha_\sigma^2(\theta,\phi)\, m_\sigma(\boldsymbol{B})$. We may now write

$$n_\sigma^{(1)}(\boldsymbol{B}) = \frac{2m_\sigma^{3/2}(\boldsymbol{B})\mu_\sigma^{3/2}(\boldsymbol{B})}{3\pi^2\sqrt{2}}, \quad \text{(B.29)}$$

and

$$n_\sigma^{(2)}(\boldsymbol{B}) = \frac{2m_\sigma^{3/2}(\boldsymbol{B})\mu_\sigma^{3/2}(\boldsymbol{B})}{\pi^2\sqrt{2}} \times \sum_{n=0}^{\infty}\frac{1}{3}a_n\left(\frac{eB\alpha_\sigma(\theta,\phi)}{m_\sigma(\boldsymbol{B})\mu_\sigma(\boldsymbol{B})}\right)^{2n+2}. \quad \text{(B.30)}$$

As in the Born-Sommerfeld approximation, we now equate the particle density in the absence of a field, $\sum_\sigma n_\sigma(0)$, and the particle density in the presence of a field, $\sum_\sigma[n_{1\sigma}(\boldsymbol{B})+n_{2\sigma}(\boldsymbol{B})]$, from which we obtain the equation

$$\sum_{\sigma} \Pi_{\sigma}^{3/2}(0) =$$
$$\sum_{\sigma} \Pi_{\sigma}^{3/2}(\boldsymbol{B}) \left(1 + \sum_{n=0}^{\infty} a_n \left(\frac{eB\alpha_{\sigma}(\theta,\phi)}{\Pi_{\sigma}(\boldsymbol{B})}\right)^{2n+2}\right). \tag{B.31}$$

We now present the details of the calculation of the linear T-coefficient of specific heat, $\gamma(\boldsymbol{B})$, for an electron gas with a strong spin-split ellipsoidal Fermi surfaces, one for each spin projection $\sigma = \{\uparrow, \downarrow\}$. Each ferromagnetically split Fermi surface has three distinct single particle effective masses, $\{m_{i\sigma}(\boldsymbol{B})\}$.

Writing the entropy, S, of the system as in Eq.(6.7) and taking the thermodynamic limit, $\sum_{\mathbf{k}\sigma} \rightarrow \sum_{\sigma} \frac{V}{(2\pi)^3} \int d^3\mathbf{k}$, and by applying the first KC transformation $k_{i\sigma} \rightarrow \sqrt{m_{i\sigma}/m_{\sigma}} k'_{i\sigma}$, we obtain

$$\begin{aligned} S/V &= k_B \sum_{\sigma} \int \frac{d^3\mathbf{k}'_{\sigma}}{(2\pi)^3} \\ &\quad \times \left[\frac{\beta\xi_{\sigma}(\mathbf{k}'_{\sigma})}{e^{\beta\xi_{\sigma}(\mathbf{k}'_{\sigma})}+1} + \ln\left(1 + e^{-\beta\xi_{\sigma}(\mathbf{k}'_{\sigma})}\right)\right], \end{aligned} \tag{B.32}$$

where $\xi_{\sigma} = \varepsilon(\mathbf{k}'_{\sigma}) - \mu_{\sigma}$.

We make use of the thermodynamic relationship for the specific heat $C_V = -\beta \frac{\partial(S/V)}{\partial\beta}$, and obtain for $B = 0$

$$C_V(0) = \frac{\beta^2 k_B}{2} c \sum_{\sigma} m_{\sigma}^{3/2}(0) \int_{-\mu_{\sigma}(0)}^{\infty} \frac{\xi_{\sigma}^2 d\xi_{\sigma} \sqrt{\xi_{\sigma} + \mu_{\sigma}(0)}}{1 + \cosh(\beta\xi_{\sigma})}, \tag{B.33}$$

where $c = \frac{1}{\pi^2\sqrt{2}}$.

Upon introducing the change of variables $x_\sigma = \beta\xi_\sigma$, allowing $T \to 0^+$, and making use of the common integral $\int_{-\infty}^{\infty} \frac{x^2 dx_\sigma}{1+\cosh x_\sigma} = \frac{2\pi^2}{3}$, we find the $B = 0$ T-coefficient to be $\gamma(0) = \sum_\sigma \frac{m_\sigma^{3/2}(0)\mu_\sigma^{1/2}(0)}{3\sqrt{2}}$.

Now we generalize to include a finite magnetic induction, $\boldsymbol{B}$, using

$$\begin{aligned} C_V(B) &= \frac{\beta^2 k_B}{2}\frac{eB}{2\pi}\sum_\sigma \int \frac{dk_{\sigma,\|}}{(2\pi)} \\ &\quad \times \sum_{n=0}^{\infty} \frac{\xi_\sigma^2\left(k_{\sigma,\|}, n+1/2\right)}{1+\cosh\left(\beta\xi_\sigma\left(k_{\sigma,\|}, n+1/2\right)\right)}, \end{aligned} \tag{B.34}$$

where

$$\xi_\sigma\left(k_{\sigma,\|}, n+1/2\right) = \frac{k_{\sigma,\|}^2}{2m_{\sigma,\|}(\boldsymbol{B})} + \omega_{\sigma,\perp}(n+1/2) - \mu_\sigma(\boldsymbol{B}), \tag{B.35}$$

We make use of the Poisson summation formula, and obtain a non-oscillatory and oscillatory term, $C_V^{(1)}(\boldsymbol{B})$ and $C_V^{(2)}(\boldsymbol{B})$ respectively, which we then evaluate separately.

We have

$$\begin{aligned} C_V^{(1)}(\boldsymbol{B}) &= \frac{\beta^2 k_B}{2}\frac{eB}{2\pi}\sum_\sigma \frac{1}{\omega_{\sigma,\perp}} \int_0^\infty c_{1\sigma} E_\sigma^{-1/2} dE_\sigma \\ &\quad \times \int_0^\infty dy_\sigma \left[\frac{\left(E_\sigma - \mu_\sigma(\boldsymbol{B}) + y_\sigma\right)^2}{1+\cosh\beta\left(E_\sigma - \mu_\sigma(\boldsymbol{B}) + y_\sigma\right)}\right], \end{aligned} \tag{B.36}$$

where we have used the change of variables $y_\sigma = \omega_{\sigma,\perp}x$, and $c_{1\sigma} = \frac{m_{\sigma,\|}^{1/2}(\boldsymbol{B})}{\pi\sqrt{2}}$.

We now let $\xi_\sigma = E_\sigma - \mu_\sigma + y_\sigma$, and $\beta\xi_\sigma = x_\sigma$, and obtain

$$\begin{aligned} C_V^{(1)}(\boldsymbol{B}) &= \frac{k_B^2 T}{2}\frac{eB}{2\pi}\sum_\sigma \frac{1}{\omega_{\sigma,\perp}}\int_0^\infty c_{1\sigma}E_\sigma^{-1/2}dE_\sigma \\ &\quad \times \int_{\beta[-\mu_\sigma(\boldsymbol{B})+E_\sigma]}^\infty dx_\sigma \left[\frac{x_\sigma^2}{1+\cosh x_\sigma}\right]. \end{aligned} \tag{B.37}$$

We then take the zero temperature limit, $T \rightarrow 0^+$, for which $\beta[-\mu_\sigma(\boldsymbol{B}) + E_\sigma] \rightarrow -\infty$, and evaluating the energy integral up to the chemical potential in a field, $\int_0^{\mu_\sigma(\boldsymbol{B})} E_\sigma^{-1/2}dE_\sigma$, we obtain

$$C_V^{(1)}(\boldsymbol{B}) = \frac{k_B^2}{3\sqrt{2}}\sum_\sigma m_\sigma^{3/2}(\boldsymbol{B})\mu_\sigma^{1/2}(\boldsymbol{B})T. \tag{B.38}$$

Now we evaluate the second term, which is oscillatory; we have

$$\begin{aligned} C_V^{(2)}(\boldsymbol{B}) &= \frac{\beta^2 k_B eB}{2\pi}\sum_\sigma \frac{c_{1\sigma}}{\omega_{\sigma,\perp}}\sum_{s=1}^\infty (-1)^s \\ &\quad \times \int_0^\infty dy_\sigma f(y_\sigma)\cos\left(2\pi s\frac{y_\sigma}{\omega_{\sigma,\perp}}\right)dy_\sigma, \end{aligned} \tag{B.39}$$

where

$$f(y_\sigma) \equiv \int_0^\infty E_\sigma^{-1/2}dE_\sigma \frac{[E_\sigma - \mu_\sigma(\boldsymbol{B}) + y_\sigma]^2}{1+\cosh\beta\left(E_\sigma - \mu_\sigma(\boldsymbol{B}) + y_\sigma\right)}, \tag{B.40}$$

for which we define $I(y_\sigma) = \int_0^\infty dy f(y_\sigma)\cos\left(2\pi s\frac{y_\sigma}{\omega_{\sigma,\perp}}\right)dy_\sigma$. By successively integrating by parts to infinite order , we obtain an infinite series expression for $I(y_\sigma)$,

$$\int_0^\infty f(y_\sigma)\cos\left(2\pi s y_\sigma/\omega_{\sigma,\perp}\right)dy_\sigma = \sum_{n=0}^{\infty}(-1)^{n+1}\frac{\omega_{\sigma,\perp}^{2n+2}}{(2\pi s)^{2n+2}}f^{(2n+1)}(0), \tag{B.41}$$

where $f^{(2n+1)}(0) = \frac{2\pi^2}{3\beta^3}\frac{1}{2^{2n+1}}\,(4n+1)!!\frac{1}{[\mu_\sigma(\boldsymbol{B})]^{2n+3/2}}$, which we obtain from Eq.(B.40) by integrating with respect to $x_\sigma = \beta[E_\sigma - \mu_\sigma(B) - y_\sigma]$, allowing $T \to 0^+$, or equivalently $\beta \to +\infty$, which then results in

$$f(y_\sigma) = \frac{2\pi^2}{3\beta^3}[\mu_\sigma(\boldsymbol{B}) - y_\sigma]^{-1/2}, \tag{B.42}$$

which can then be differentiated $(2n+1)$-times to obtain the desired result. Substituting Eq.(B.41) into Eq.(B.39), we obtain

$$\begin{aligned} C_V^{(2)}(B) &= \frac{k_B eB}{\pi}\left(\frac{\pi^2}{3\beta}\right)\sum_\sigma \frac{c_{1\sigma}}{\omega_{\sigma,\perp}}\sum_{n=0}^{\infty}(-1)^n \\ &\quad\times\sum_{s=1}^{\infty}\frac{(-1)^{s-1}}{s^{2n+2}}\frac{\omega_{\sigma,\perp}^{2n+2}}{(2\pi)^{2n+2}}\frac{(4n+1)!!}{2^{2n+1}} \\ &\quad\times\frac{1}{(\mu_\sigma(\boldsymbol{B}))^{2n+3/2}}, \end{aligned} \tag{B.43}$$

so that we have

$$C_V^{(2)}(B) = \sum_\sigma \frac{k_B^2 m_\sigma^{3/2}(\boldsymbol{B})\mu_\sigma^{1/2}(\boldsymbol{B})}{3\sqrt{2}} \times \sum_{n=0}^{\infty} \lambda_n \left(\frac{eB\alpha_\sigma(\theta,\phi)}{m_\sigma(\boldsymbol{B})\mu_\sigma(\boldsymbol{B})} \right)^{2n+2} T, \tag{B.44}$$

where

$$\lambda_n = \frac{1}{3}(4n+1)\, a_n. \tag{B.45}$$

Now $C_V(\boldsymbol{B}) = C_V^{(1)}(\boldsymbol{B}) + C_V^{(2)}(\boldsymbol{B})$, from which we get

$$\gamma(\boldsymbol{B}) = \frac{k_B^2}{3\sqrt{2}} \sum_\sigma m_\sigma(\boldsymbol{B})\, \Pi_\sigma^{1/2}(\boldsymbol{B}) \times \left(1 + \sum_{n=0}^{\infty} \lambda_n \left(\frac{eB\alpha_\sigma(\theta,\phi)}{\Pi_\sigma(\boldsymbol{B})} \right)^{2n+2} \right). \tag{B.46}$$

Here we present the derivation for the conversion factor λ from m^3 to moles, the effective mass in zero field $m_\downarrow(0)$, and the chemical potential in zero field $\mu_\downarrow(0)$.

We have the number of Uranium atoms per unit cell $N_{\mathrm{U}} = 4$U atoms/unit cell [12] the volume of a unit cell $V_{\mathrm{c}} = 4.35 \times 10^{-10} \times 6.90 \times 10^{-10} \times 7.52 \times 10^{-10}\mathrm{m}^3 = 225 \times 10^{-30}\mathrm{m}^3/$unit cell [46], the number of atoms in one mole of atoms is $N_{\mathrm{A}} = 6.022 \times 10^{23}$U atoms/mol of URhGe, from which we may obtain the conversion factor

$$\lambda = (V_c/N_U) \times N_A = 3.4 \times 10^{-5}\mathrm{m}^3/\mathrm{mol}. \tag{B.47}$$

We also have from Yelland $et\ al.$ [8] that the number of carriers per Uranium is

$$N_{\mathrm{c}}/\mathrm{U} = 2.1 \times 10^{-3}\text{carriers/U}, \tag{B.48}$$

from which we calculate k_{F},

$$N_{\mathrm{c}}/\mathrm{U} = 2.1 \times 10^{-3} = \frac{V_c \times k_F^3}{6\pi^2}, \tag{B.49}$$

and obtain

$$k_F = 0.82 \times 10^{10}/\mathrm{m}. \tag{B.50}$$

Now, we substitute our values into the expression for the zero field linear-T coefficient of the specific heat

$$\gamma(0) = \frac{2(\alpha m_e)k_F k_B^2 \times \lambda}{\hbar^2}, \tag{B.51}$$

where α is the integer multiple of electron masses, and obtain $m_{\downarrow}(0) = 180m_e$, where we have used $\gamma(0) = 160 \times 10^{-3}$J/mol K^2, and we have used the conversion factor λ to convert from moles to m^3, and the factor of 2 comes from taking both spin contributions equally.

Now we calculate the effective mass on the $\downarrow$ FS in zero field

$$\gamma(0) = \frac{k_B^2}{3\hbar^3\sqrt{2}} \times 10^3 \times \lambda \times m_{\downarrow}^{3/2}(0)\mu_{\downarrow}^{1/2}(0) \tag{B.52}$$

and obtain

$$\mu_{\downarrow}(0) = 20 \text{ meV} \tag{B.53}$$

We have also obtained good least-squares fits to the data for $\boldsymbol{H} \parallel \hat{\boldsymbol{a}}$ and $\boldsymbol{H} \parallel \hat{\boldsymbol{c}}$ shown in Figure (3), for which we have obtained $\gamma_{\boldsymbol{H}\|a} = 155.64$ mJ/(mol K^2) $- 7.0175$ mJ/(mol K^2 T)$(\mu_0 H) +$ 0.26588 mJ/(mol K^{2}T^2)$(\mu_0 H)^2$, and $\gamma_{\boldsymbol{H}\|c} = 158.05$ mJ/(mol K^2)-0.84964 mJ/(mol K^2 T)$(\mu_0 H)+$ 0.37012 mJ/(mol K^2 T^2)$(\mu_0 H)^2$.

LIST OF REFERENCES

[1] N. T. Huy, A. Gasparini, D. E. de Nijs, Y. Huang, J. C. P. Klaasse, T. Gortenmulder, A. de Visser, A. Hamann, T. Görlach, and H. v. Löhneysen, Phys. Rev. Lett. **99**, 067006 (2007).

[2] N. T. Huy, D. E. de Nijs, Y. K. Huang, A. de Visser, Phys. Rev. Lett. **100** 077002

[3] S. S. Saxena, P. Agarwal, K. Ahilan, F.M. Grosche, R. K. W. Haselwimmer, M. J. Steiner, E. Pugh, I. R. Walker, S. R. Julian, P. Monthoux, G. G. Lonzarich, A. Huxley, I. Sheikin, D. Braithwaite and J. Flouquet 2000 Nature 406 587

[4] A. de Visser, N. T. Huy, A. Gasparini, D. E. de Nijs, D. Andreica, C. Baines, and A. Amato, Phys. Rev. Lett. **102**, 167003 (2009).

[5] D. Aoki, A. Huxley, E. Ressouche, D. Braithwaite, J. Flouquet, J.-P. Brison, E. Lhotel, and C. Paulsen, Nature **413**, 613 (2001).

[6] F. Hardy and A. D. Huxley, Phys. Rev. Lett.**94**, 247006 (2005).

[7] F. Lévy, I. Sheikin, and A. Huxley, Nature Phys. **3**, 460 (2007).

[8] E. A. Yelland, J. M. Barraclough, W. Wang, K. V. Kamenev, and A. D. Huxley, Nature Phys. **7**, 890 (2011).

[9] F. Lévy, I. Sheikin, B. Grenier, C. Marcenat, and A. Huxley, J. Phys.: Condens. Matter **21**, 164211 (2009).

[10] D. Aoki, T. D. Matsuda, V. Taufour, E. Hassinger, G. Knebel, and J. Flouquet, J. Phys. Soc. Jpn. **78**, 113709 (2009).

[11] D. Aoki, T. D. Matsuda, V. Taufour, E. Hassinger, G. Knebel, and J. Flouquet, J. Phys. Soc. Jpn. **80**, 013705 (2011).

[12] D. Aoki and J. Flouquet, J. Phys. Soc. Jpn. **81**, 011003 (2012).

[13] K. Scharnberg and R. A. Klemm, Phys. Rev. B **22**, 5233 (1980).

[14] K. Scharnberg and R. A. Klemm, Phys. Rev. Lett. **54**, 2445 (1985).

[15] R. A. Klemm and K. Scharnberg, Phys. Rev. B **24**, 6361 (1981).

[16] V. P. Mineev, C. R. Physique **7**, 35 (2006).

[17] M. Diviš, L. M. Sandratskii, M. Richter, P. Mohn, and P. Novák, J. Alloys Comp. **337**, 48 (2002).

[18] A. B. Shick, Phys. Rev. B. **65**, 180509(R) (2002).

[19] W. Müller, V. H. Tran, and M. Richter, Phys. Rev. B **80**, 195108 (2009).

[20] G. E. Volovik and L. P. Gor'kov, Zh. Eksp. Teor. Fiz. **88**, 1412 (1985) [Sov. Phys. JETP **61**, 843 (1985).]

[21] E. I. Blount, Phys. Rev. B **32**, 2935 (1985).

[22] J. Sauls, Adv. Phys. **43**, 113 (1994).

[23] B. S. Shivaram, Y. H. Jeong, T. F. Rosenbaum, and D. G. Hinks, Phys. Rev. Lett. **56**, 1078 (1986).

[24] C. H. Choi and J. Sauls, Phys. Rev. Lett. **66**, 484 (1991).

[25] Y. Machida, A. Itoh, K. Izawa, Y. Haga, E. Yamamoto, N. Kimura, Y. Onuki, Y. Tsutsumi, and K. Machida, Phys. Rev. Lett. **108**, 157002 (2012).

[26] V. P. Mineev and K. V. Samokhin, *Introduction to Unconventional Superconductivity* (New York: Gordon and Breach 1999).

[27] S. Yonezawa, T. Kajikawa, and Y. Maeno, Phys. Rev. Lett. **110**, 077003 (2013).

[28] M. Kriener, K. Segawa, Z. Ren, S. Sasaki, and Y. Ando, *Phys. Rev. Lett.* **106**, 127004 (2011).

[29] T. V. Bay, T. Naka, Y. K. Huang, H. Luigjes, M. S. Golden, and A. de Visser, Phys. Rev. Lett. **108**, 057001 (2012).

[30] R. Balian and N. R. Werthamer, Phys. Rev. **131**, 1553 (1963).

[31] I. A. Luk'yanchuk and V. P. Mineev, Sov. Phys. JETP **66**, 1168 (1987).

[32] C. Lörscher, J. Zhang, Q. Gu, and R. A. Klemm, to be published.

[33] R. A. Klemm, *Layered Superconductors Volume 1* (Oxford University Press, Oxford, UK and New York, NY 2012).

[34] M. Prohammer and J. P. Carbotte, Phys. Rev. B **42**, 2032 (1990).

[35] C. T. Rieck and K. Scharnberg, Physica B **163**, 670 (1990).

[36] H. A. Vieyra, N. Oeschler, S. Seiro, H. S. Jeevan, C. Geibel, D. Parker, and F. Steglich, Phys. Rev. Lett. **106**, 207001 (2011).

[37] A. A. Abrikosov, L. N. Gor'kov, and I. E. Dzaloshinskii, *Methods of Quantum Field Theory in Statistical Physics* (Dover Books on Physics, 1975).

[38] F. Hardy and A. D. Huxley, Phys. Rev. Lett. **94**, 247006 (2005).

[39] D. Aoki, I. Sheikin, T. D. Matsuda, V. Taufour, G. Knebel, and J. Flouquet, J. Phys. Soc. Jpn. **80**, 013705 (2011).

[40] L. Malone, L. Howald, A. Pourret, D. Aoki, V. Taufour, G. Knebel, and J. Flouquet, Phys. Rev. B **85**, 024526 (2012).

[41] L. Malone *et al.* (unpublished).

[42] D. Aoki, W. Knafo, and I. Sheikin, C. R. Phys. **14**, 53 (2013)

[43] K. Kadowaki and S. B. Woods, Solid State Commun. **58**, 507 (1986)

[44] R. A. Klemm and J. R. Clem, Phys. Rev. B **21**, 1868 (1980).

[45] C. Lörscher, J. Zhang, Q. Gu, and R. A. Klemm, Phys. Rev. B **88**, 024504 (2013).

[46] V. H. Tran, R. Troć, and G. André, J. Magn. Mater. **186**, 81-86 (1998).

[47] R. A. Klemm, A. Luther, M. R. Beasley, Phys. Rev. B **12** 877

[48] T. Hattori, K. Karuba, Y. Ihara, K. Ishida, K. Deguchi, N. K. Sato, and T. Yamamura, Phys. Rev. B **88**, 085127(2013).

[49] A. P. Mackenzie 2003 *Rev. Mod. Phys.* **75** 657–712

[50] M. Sigrist 2005 *Prog. Theor. Phys. Supplement* **160** 1–14

[51] Y. Maeno , S. Kittaka, T. Nomura, S. Yonezawa and K. Ishida 2012 *J. Phys. Soc.Jpn.* **81** 011009

[52] K. Ishida, H. Mukuda, Y. Kitaoka, K. Asayama, Z. Q. Mao, Y. Mori and Y. Maeno 1998 *Nature* **396** 658–660

[53] H. Mukuda, K. Ishida, Y. Kitaoka, Z. Mao, Y. Mori and Y. Maeno 1999 *J Low Temp. Phys.* **117** 1587–1591

[54] K. Ishida, H. Mukuda, Y. Kitaoka, Z. Mao, H. Fukazawa and Y. Maeno 2001 *Phys. Rev.* B **63** 060507

[55] H. Murakawa, K. Ishida, K. Kitagawa, Z. Mao and Y. Maeno 2004 *Phys. Rev. Lett.* **93** 167004

[56] H. Murakawa, K. Ishida, K. Kitagawa, H. Ikeda, Z. Q. Mao and Y. Maeno 2007 *J. Phys. Soc. Jpn.* **76** 024716

[57] T. M. Riseman, P. G. Kealey, E. M. Forgan, A. P. Mackenzie, L. M. Galvin, A. W. Tyler, S. L. Lee, C. Ager, D. M. Paul, C. M. Aegerter, R. Cubitt, Z. Q. Mao, T. Akima and Y. Maeno 1998 *Nature* **396** 242–245

[58] J. Duffy, S. Hayden, Y. Maeno, Z. Mao, J. Kulda and G. McIntyre 2000 *Phys. Rev. Lett.* **85** 5412–5415

[59] G. M. Luke, Y. Fudamoto, K. M. Kojima, M. I. Larkin, J. Merrin, B. Nachumi, Y. J. Uemura, Y. Maeno, Z. Q. Mao, Y. Mori, H. Nakamura and M. Sigrist 1998 *Nature* **394** 558–561

[60] K. Deguchi, M. A Tanatar, Z. Mao, T. Ishiguro and Y. Maeno 2002 *J. Phys. Soc. Jpn.* **71** 2839–2842

[61] S. Kittaka, T. Nakamura, Y. Aono, S. Yonezawa, K. Ishida and Y. Maeno 2009 *Phys. Rev.* B **80** 174514

[62] S. Yonezawa, T. Kajikawa and Y. Maeno 2013 *Phys. Rev. Lett.* **110** 077003

[63] A. M. Clogston 1962 *Phys. Rev. Lett.* **9** 266–267

[64] A. J. Leggett 1975 *Rev. Mod. Phys.* **47** 331–414

[65] K. Machida and M. Ichioka 2008 *Phys. Rev.* B **77** 184515

[66] C. H. Choi 2010 *J. Korean Phys. Soc.* **56** 933

[67] Z. Q. Mao, Y. Maeno, S. NishiZaki, T. Akima and T. Ishiguro 2000 *Phys. Rev. Lett.* **84** 991–994

[68] K. Deguchi, Z. Q. Mao, H. Yaguchi and Y. Maeno 2004 *Phys. Rev. Lett.* **92** 047002

[69] D. Agterberg 2001 *Phys. Rev.* B **64** 052502

[70] V. P. Mineev 2008 *Phys. Rev.* B **77** 064519

[71] M. Ishihara, Y. Amano, M. Ichioka and K. Machida 2013 *Phys. Rev.* B **87** 224509

[72] J. Zhang, C. Lörscher, Q. Gu and R. A. Klemm 2014 *J. Phys.: Condens. Matter* **26** 252202

[73] H. Suderow, V. Crepo, I. Guillamon, S. Viera, F. Servant, P. Lejay, J. P. Brison and J. Flouquet 2009 *New J. Phys.* **11** 093004

[74] I. A. Firmo, S. Lederer, C. Lupien, A. P. Mackenzie, J. C. Davis and S. A. Kivelson 2013 *Phys. Rev.* B **88** 134521

[75] E. Pavarini and I. Mazin 2006 *Phys. Rev.* B **74** 035115; *ibid* (2007) **76** 079901(E)

[76] B. E. Hall and R. A. Klemm 2014 (unpublished)

[77] E. J. Rozbicki, J. F. Annett, J. R. Souquet and A. P. Mackenzie 2011 *J. Phys. Condens. Matter* **23** 094201

[78] M. Sigrist and K. Ueda 1991 *Rev. Mod. Phys.* **63** 239–311

[79] T. M. Rice and M. Sigrist 1999 *J. Phys.: Condens. Matter* **7** L643–L648

[80] C. Bergemann, S. Julian, A. P. Mackenzie, S. NishiZaki and Y. Maeno 2000 *Phys. Rev. Lett.* **84** 2662–2665

[81] S. Raghu, A. Kapitulnik and S. A. Kivelson 2010 *Phys. Rev. Lett.* **105** 136401

[82] J. Annett, G. Litak, B. Györffy and K. Wysokiński 2002 *Phys. Rev.* B **66** 134514

[83] M. Zhitomirsky and T. Rice 2001 *Phys. Rev. Lett.* **87** 057001

[84] J. W. Huo, T. Rice and F. C. Zhang 2013 *Phys. Rev. Lett.* **110** 167003

[85] E. Helfand and N. R. Werthamer 1966 *Phys. Rev.* **147** 288–294

[86] R. A. Klemm and K. Scharnberg 1980 *Phys. Rev.* B **22** 5233–5244

[87] P. W. Anderson and P. Morel 1961 *Phys. Rev.* **123** 1911–1934

[88] P. Anderson and W. Brinkman 1973 *Phys. Rev. Lett.* **30** 1108–1111

[89] C. Choi and J. Sauls 1993 *Phys. Rev.* B **48** 13684–13690

[90] Y. Matsuda and H. Shimahara 2007 *J. Phys. Soc. Jpn.* **76** 051005

[91] R. J. Noer and W. D. Knight 1964 *Rev. Mod. Phys.* **36** 177–184

[92] S. Adenwalla, S. W. Lin, Q. Z. Ran, Z. Zhao, J. B. Ketterson, J. A. Sauls, L. Taillefer, D. G. Hinks, M. Levy, and B. K. Sharma 1990 *Phys. Rev. Lett.* **65**, 2298

[93] H. Tou, Y. Kitaoka, K. Ishida, K. Asayama, N. Kimura, Y. $\overline{\mathrm{O}}$nuki, E. Yamamoto, Y. Haga, and K. Maezawa 1998 *Phys. Rev. Lett.* **80**, 3129

[94] E Hassinger, D. Aoki, G. Knebel, and J. Flouquet 2008 *J. Phys. Soc. Jpn.* **77**, 073703

[95] M. Czekala-Samsel, S. Elgazzar, P. M. Oppeneer, E. Talik, W. Walerczyk, R. Troc 2010 *J. Phys.: Condens. Matter* **22** 015503